El Instituto de Investigaciones en Materiales
de la
Universidad Nacional Autónoma de México
Otorga la presente

CONSTANCIA

A: Cardenas Aguazaco William Antonio

Por haber asistido el Curso-Taller:

CIENCIA Y TECNOLOGÍA DE NANOFIBRAS Y NANOTEXTILES

IMPARTIDO POR EL DR. JUAN PAULO HINESTROZA

Del 10 al 12 de enero de 2017.
"POR MI RAZA HABLARÁ EL ESPÍRITU"
Ciudad Universitaria Cd.Mx, a 12 de enero de 2017.

Dr. José Israel Betancourt Reyes
Director

Dr. Juan Paulo Hinestroza
Universidad de Cornell, NY, USA.

Dr. Ricardo Vera Graziano
Coordinador



UNIVERSIDAD
EL BOSQUE

FACULTAD DE CIENCIAS
Programa de Biología

CENTRO DE MICROSCOPIA Y MICROANÁLISIS
CEMMI

CERTIFICAN QUE

WILLIAN A CARDENAS AGUAZACO

CC. *1054093910*

PARTICIPÓ EN EL

II CURSO DE ANALISIS DE IMAGENES

En calidad de Asistente

CELEBRADO del 6 al 8 de junio del 2018 con una
Duracion de 24 horas acadèmicas
Bogota. Colombia

Clara Santafé
Directora de programa biología
Facultad de ciencias
UNIVERSIDAD EL BOSQUE

Edgar Palacios
Secretario Academico
Facultad de ciencias
UNIVERSIDAD EL BOSQUE

Magnolia Herrera
Directora
CENTRO DE MICROSCOPIA Y
MICROANALISIS

La Secretaría Distrital de Salud y El Instituto Distrital
de Ciencia, Biotecnología e Innovación en Salud - IDCBIS

CERTIFICAN QUE:

William A. Cardenas Aguazaco

Participó en el curso:

Escritura de Artículos Científicos con una intensidad horaria de 30 horas.
Bogotá, Noviembre del 2019

Manuel González Mayorga
Subsecretario de Salud Pública (E)

Nayibe Castro Novoa
Docente del Observatorio Colombiano
de Ciencia y Tecnología - OCyT

IDCBIS
Instituto Distrital de Ciencia,
Biotecnología e Innovación en Salud

Alcaldía de Bogotá

El conocimiento es de todos

Minciencias



El Ministerio de Ciencia, Tecnología e Innovación y la Superintendencia de Industria y Comercio,

certifican que:

William Cárdenas Aguazaco

Participó en la iniciativa **Uso de la Información Tecnológica que contienen los documentos de patentes.** Modalidad Virtual. Duración 60 horas.

Este certificado se expide a los 30 días del mes de julio de 2021.

Julián Humberto Ferro Arellana
Director de la Dirección de Transferencia y Uso de Conocimiento.
Ministerio de Ciencia, Tecnología e innovación

María José Lamus Becerra
Superintendente Delegada para la Propiedad Industrial
Superintendencia de Industria y Comercio

informaciontecnologica.co

Industria y Comercio
SUPERINTENDENCIA

tecnnova
Conectamos Universidad Empresa Estado

Universidad de los Andes | Facultad de Medicina

Universidad Militar Nueva Granada

Línea bioética médica y salud pública

Universidad Militar Nueva Granada
Facultad de Educación y Humanidades - Doctorado en Bioética
La Universidad de los Andes
Facultad de Medicina

Certifica que:

William Cárdenas

C.C.1054093910

Asistió como participante y aprobó el curso de:
Bioética en el contexto colombiano
Intensidad :
4 horas
Febrero 21 de 2022

Natalia Mejía
Decana
Facultad Medicina
Universidad de los Andes

Ruby Stella Romero
Decana
Facultad de Educación y Humanidades
Universidad Militar Nueva Granada

Universidad de los Andes Vigilada Mineducacion, Reconocimiento como Universidad: Decreto 1297 del 30 de mayo de 1964 Reconocimiento personeria jurídica: Resolución 28 del 23 de febrero de 1949 Minjusticia.
Universidad Militar Nueva Granada Institución de educación superior – Vigilada Mineducación – Decreto 1075 del 26 de mayo de 2015 – Código SNIES 1117
Acreditación institucional de alta calidad de la educación superior, por seis años, mediante la Resolución 10683 del 16 de julio de 2015

AVANZAR

Asociación para el Avance de la Investigación Clínica en Colombia

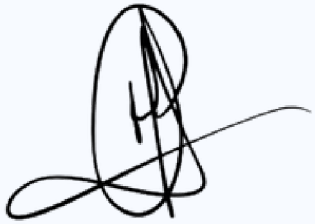
CERTIFICA QUE:

William Antonio Cardenas Aguazaco

Participó como asistente en el:

Curso de Buenas Prácticas Clínicas - E6 (Revisión 2)

El cual se realizó virtualmente el 17 de marzo de 2023.
Con intensidad de 8 horas



Henry García
Presidente
Junta Directiva AVANZAR

Contenido: Introducción a la Buenas Prácticas Clínicas / Desarrollo de un medicamento / Comité de ética / Investigador / Patrocinador / Protocolo / Manual del Investigador /Documentos Esenciales / Consentimiento Informado /Farmacovigilancia / Regulación Local Vigente

Certificado 20230317 - 16

Universidad del Rosario | ADVANCE Educación Continua

AVANZAR

LA UNIVERSIDAD DEL ROSARIO, LA ESCUELA DE MEDICINA Y CIENCIAS DE LA SALUD Y ***EDUCACIÓN CONTINUA***

OTORGAN EL PRESENTE

DIPLOMA A:

WILLIAM ANTONIO CÁRDENAS AGUAZACO

CC 1054093910

Por su asistencia y participación en el **DIPLOMADO EN GESTIÓN DE ENSAYOS CLÍNICOS: ÉNFASIS EN DISPOSITIVOS Y MEDICAMENTOS**, realizado entre el 03 de septiembre y el 03 de diciembre de dos mil veinticinco (2025) con una intensidad de ciento diez (110) horas académicas.

Para constancia se firma en la ciudad de Bogotá D.C., República de Colombia, a los tres (03) días del mes de diciembre de dos mil veinticinco (2025).

JUAN MAURICIO PARDO OVIEDO
Decano
Escuela de Medicina y Ciencias de la Salud

LEONARDO ARANGO MARTÍNEZ
Director
Educación Continua

Real Cédula del 31 de diciembre de 1651 - Resolución 58 del 16 de septiembre de 1895 Vigilada por el Ministerio de Educación Nacional Código: 15955-15

#AVANZACONPROPÓSITO

PAPER • **OPEN ACCESS**

Preparation of potato starch microfibers obtained by electro wet spinning

To cite this article: W Cárdenas *et al* 2016 *IOP Conf. Ser.: Mater. Sci. Eng.* **138** 012001

View the article online for updates and enhancements.

Related content

- Engineering of composite metallic microfibers towards development of plasmonic devices for sensing applications
A Petropoulou, G Antonopoulos, P Bastock et al.
- Mechanical and molecular studies of biocomposites filled with oil palm empty fruit bunches microfibers
S Nikmatin, D R Saepulloh, Irmansyah et al.
- Liquid Concentration Sensing Properties of Microfibers with a Nanoscale-Structured Film
Zhou Guo-Rui, Lv Hai-Bing, Yuan Xiao-Dong et al.

Recent citations

- Comparative Study of Starch Fibers Obtained by Electro-spinning of Indigenous, Commercial and Cationic Potato Starch
Cárdenas William A *et al*
- Electrospinning of native and anionic corn starch fibers with different amylose contents
Laura Martins Fonseca *et al*
- S. L. Rúa Jiménez *et al*



IOP ebooks™

Bringing you innovative digital publishing with leading voices to create your essential collection of books in STEM research.

Start exploring the collection - download the first chapter of every title for free.

This content was downloaded from IP address 189.130.183.53 on 09/05/2019 at 17:31

Preparation of potato starch microfibers obtained by electro wet spinning

W Cárdenas[1,4], E Y Gómez-Pachon[2,4], E Muñoz[1,4], and R Vera-Graziano[3]

[1] Escuela de Ciencias Químicas, Facultad de Ciencias, Universidad Pedagógica y Tecnológica de Colombia-UPTC. Avenida Central del Norte 39-115 Sede Central Tunja–Boyacá–Colombia

[2] Escuela de Diseño Industrial, Facultad sede Duitama, Universidad Pedagógica y Tecnológica de Colombia-UPTC. Carrera18 con Calle 22 Duitama-Boyacá-Colombia

[3] Instituto de investigaciones en materiales-IIM, Universidad Nacional Autónoma de México-UNAM. Ciudad Universitaria, circuito exterior s/n 04510 México D.F-México

[4] Grupo de Investigación en desarrollo y aplicación de nuevos materiales-DANUM, Universidad Pedagógica y Tecnológica de Colombia-UPTC.

Email: edwin.gomez02@uptc.edu.co

Abstract. Starch is one of the most abundant biopolymer in nature. It has been primarily used as a thickener in the food industry. Starch is found in greater amounts in the potato tubers, which is one of the largest food productions in the region of Boyacá-Colombia. Thus, potatoes are a viable source of starch. The main objective of this study is the preparation and characterization of native starch´s microfiber by electro wet-spinning technique. The parameters that were changed for each treatment were as follows: the amount of potential applied to the solution, the distance between the needle and the collector and the rate of injection of the solution in order to determine the physical and chemical properties of the membranes, conformed by potatoes starch microfiber. Diverse instrumental analysis techniques were applied. They were: Scanning Electron Microscopy (SEM) to determine the morphologies and diameters of microfibers, Fourier Transform Infrared Spectroscopy (FTIR) to determine the chemical changes, Thermogravimetric Analysis (TGA) and Differential Calorimetry Scanning (DSC) to obtain the thermal transitions and the temperatures of useful. The microfibers were analysed in order to determine their structural properties and thus define the range of application. In conclusion, potatoes starch microfibers were obtained with average diameters of 15, 17, 23 and 25 micrometres, besides the fibers presented a degradation temperature of 304 °C, indicating that fibers are available with diameters of small scale, with good thermal properties. This study will enable the implementation of the microfibers to obtain bio packaging for food products and other applications.

1. Introduction

Polymeric Nano and microfibers have been studied enough due to their characteristics which present high porosity, mechanical strength, flexibility and adhesion to other materials and high surface energy due to tiny diameters. Some other outstanding microfibers polymers' properties such as the

Content from this work may be used under the terms of the Creative Commons Attribution 3.0 licence. Any further distribution of this work must maintain attribution to the author(s) and the title of the work, journal citation and DOI.
Published under licence by IOP Publishing Ltd

mechanical, physical and chemical have been reported in several papers. These exalted properties are important for the development of new materials for industrial and technological applications. One of the most used techniques for preparation in nano-microfibers is the electrospinning. This is due to the versatility to prepare continuous fibers in diverse sizes: from nano to the micro size [1, 2].

The main parameters of electrospinning are power supply of high voltage, rate of injection of the solution and distance between needle and metallic collector. The power supply of high voltage charges the polymer solution accelerating it from the needle to a collector. A jet of solution is ejected toward the metal plate due to the electric field force which is greater than the surface tension of the polymer solution. The jet of the solution is exposed to the atmosphere over the course of needle to collector, allowing the solvent to evaporate. This is to obtain solid polymer fibers with small diameters in the collector [3-5]. This technique in which fibers with small-scale diameters are formed by use of electrostatic forces, was discovered many years ago[6-8], but in the last decade research in this area has been increasing given that many studies for the production of nonwoven webs from a variety of synthetic polymers to be used in different applications such as filters, textiles, tissue scaffolds, drug delivery, sensors and nanocomposites[9-14].

Also electrospun from natural polymers such as starch and cellulose have been studied, being that these polysaccharides have rapid degradation, high biocompatibility and are not harmful to the environment. These natural polymers have been studied for the manufacture of products that replace fossil fuel-based materials [15, 16]. Starch is a major natural polymer, besides being abundant in nature, is also a great industrial utility either in the food, pharmaceutical, textile, paper, among others [17-20]. One of the main advantages for natural polymers is its easy access because there are various sources that have concentrations of more than 70% of polysaccharide. Among the most food used for the extraction of starch are corn, potatoes, barley and wheat [21-24].

In previous studies Kong, L et al [25] conducted electrospinning of starch from different sources such corn, potatoes, beans, rice and barley. They considered several grades of concentration of amylose and amylopectin, composites in which variation of concentration in the starch, offers different qualities as high heat resistance as described by Barichello et al [25]. Also Kong et al studied parameters of electro wet-spinning for obtaining corn starch fibers with diameters around 1 a 5 micrometers. Besides Kong, L et al [25-27] obtained starch microfibers the electrospinning equipment was configured to electro wet-spinning where the plate collector was immersed in pure ethanol with the final purpose of retirement of dimethyl sulfoxide dissolvent. However, they used industrial starch for electrospun microfibers and they have not been made electro wet-spinning from nature starch from the potatoes.

For this reason, the proposal of this paper is to obtain the starch potatoes microfibers with the technical of electro wet-spinning from the natural potatoes and special from the region of Boyacá like the variety Diacol Capiro (R12) which its high amylose gives the starch high thermal resistance, this being quite important for the preparation of new biodegradable materials[26] with the objective for industrial applications.

2. Experimental

2.1. Materials

The extraction of starch was carried out from to the potato variety Diacol Capiro, also known as R-12, cultivated in Boyacá-Colombia. The solvent for the preparation of starch solution was dimethyl

sulfoxide (DMSO, CAS: 67-68-5), being acquired from the marketing firm Merck at a concentration of 99%. Also ethanol (CAS: 64-17-5) was used. It was purchased from Sigma-Aldrich trading house at a concentration of 99.8%. The extraction of the starch is carried out following the methodology proposed by Vasanthan et al and Aristizabal et al [1, 6]. The solution obtained is allowed to settle for 12 hours and the precipitate was washed with deionized water and subjected to a drying air flow at 40 °C for 8 hours.

2.2. Electro wet-spinning

The equipment used for this work was the electrospinning which was configured to wet. It was constructed at Universidad Pedagógica y Tecnológica de Colombia- hereafter UPTC, (see Figure 1). The power supply used is HV 350R provided by the company Unlimited Company Amherst, the injector was provided by the company Syringe Pump Company Pump Systems Inc model NE model 4000 injector. The collector plate was immersed in a solution of ethanol-water 70:30, because this solution dissolves the DMSO and so the microfibers collected are starch with high purity. The starch solution used in electro wet-spinning process was prepared according to Kong et al [5], with a starch concentration of 10% w/w, due to starches with a percentage higher than 70% amylose are completely dissolved in DMSO in a range of 10-20% w/w of starch.

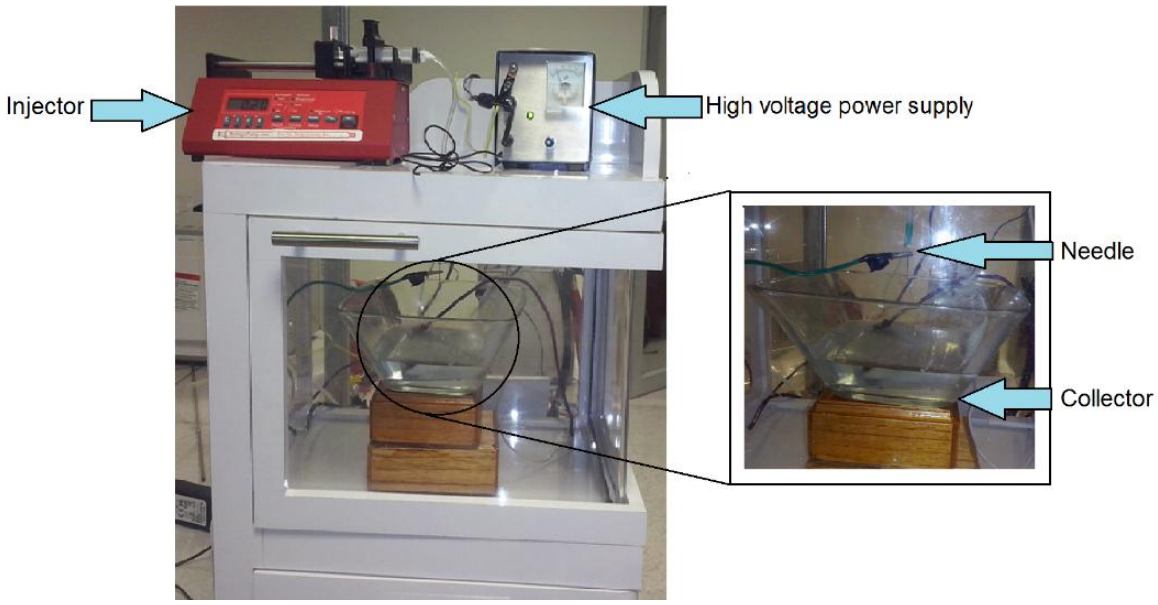


Figure 1. Electro wet-spinning equipment belonging to UPTC.

2.3. Techniques used for the characterization

The fibers were analysed by infrared Fourier transform spectroscopy with attenuated total reflectance (ATR-FTIR). The equipment used for the analysis was the ATR-Thermo Scientific Nicolet iS5, making a total of 32 scans in a range from 4000 to 400 cm-1.For the Thermal Analysis was used the DSC and TGA about the starch potatoes fibers. This technique was performed in a calorimeter SDT Q600 TGA / DSC TA Instruments. The analysis was performed with a heating rate 10 °C/min, 18 to 400 °C. For the morphological determination and for the porosity of the fibers was performed a technique with scanning electron microscopy-SEM. These micrographs were made through JEOL-JSM-7600F (Japan) equipment Tungsten filament with a voltage difference of 20.0 KV. Photographs

taken for analysis of the fibers contained increases from 60x to 650x. To carry out the estimation of fiber´s diameters, the micrographs were analysed using the Image J software.

3. Results

3.1. Infrared Spectroscopy

The fibers were analysed by ATR-FTIR to observe if the electro wet-spinning process causes chemical changes in the fibers. The native starch potatoes of powder were taken as reference to the infrared spectrum and so, used to determine whether there are changes in the spectrum of the fibers. In Figure 2, the spectra obtained fibers starch and native starch powder are presented. The IR spectrum for fibers of native starch presented one band at 3289 cm−1 related to the OH group bending [27] and at 1148,60; 1076,68 and 1000 cm−1 corresponding to –C–O–C– stretching vibration of glucose [28]. The bands found between 940 and 575 cm−1 were attributed to the whole glucose ring stretching vibrations. The band at 1635,26 cm−1 is due to tightly bound water present in the starch [29].The signal at 2926,59 cm−1 was the characteristic vibration of C–H stretches [30].

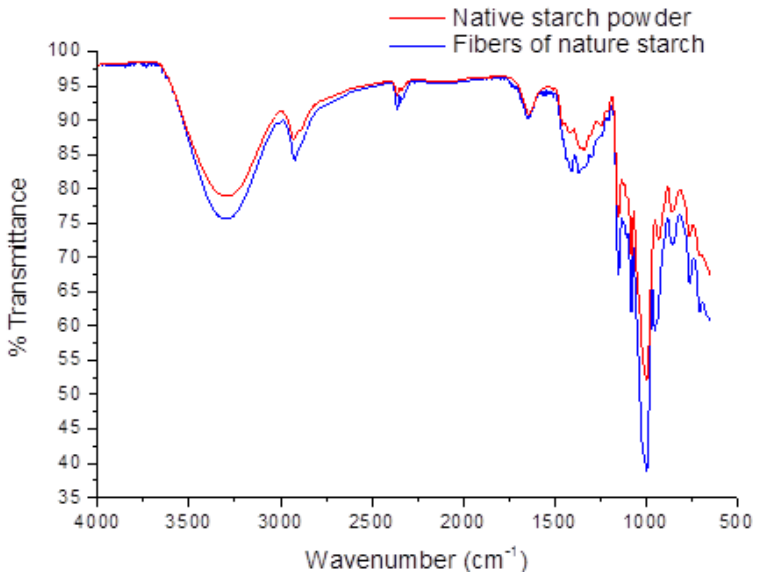


Figure 2. Infrared spectrum of the fibers potato starch and potato starch powder

For the of native starch, the IR spectrum presents the band of the OH group bending at 3296,59 cm-1. The C-O-C stretching vibration of glucose presents signals at 1148,15; 1077,83 and 1000 cm-1 and the bands attributes to the glucose ring stretching vibrations are between 937-580 cm-1. At 1652,15 cm-1 is the bound water present in the starch and the band characteristic vibration of C-H stretches is found at 2921,93 cm-1. As shown in Figure 2, the electrospun fibers of native starch do not present chemical changes to the native starch powder. The bands found in both spectra are described in Table 1. Given the similarity of the signals obtained, we can confirm that the starch does not undergo chemical changes as a result of electro wet-spinning.

Table 1. Signals encountered in the infrared spectrum of the fibers of native starch and starch.

Starch Fibers (cm^{-1})	Native Starch (cm^{-1})	Type of vibration
3289,08	3296,59	Stretch wáter
2926,59	2921,93	C-H stretching
1635,26	1652,15	O-H bending
1148,60; 1076,68 y 1000	1148,15; 1077,83 y 1000	Stretch C-O-C

3.2. Thermal Analysis- TGA

To observe the thermal properties belonging to the starch potatoes fibers an analysis of TGA was conducted and the results are shown in Figure 3.

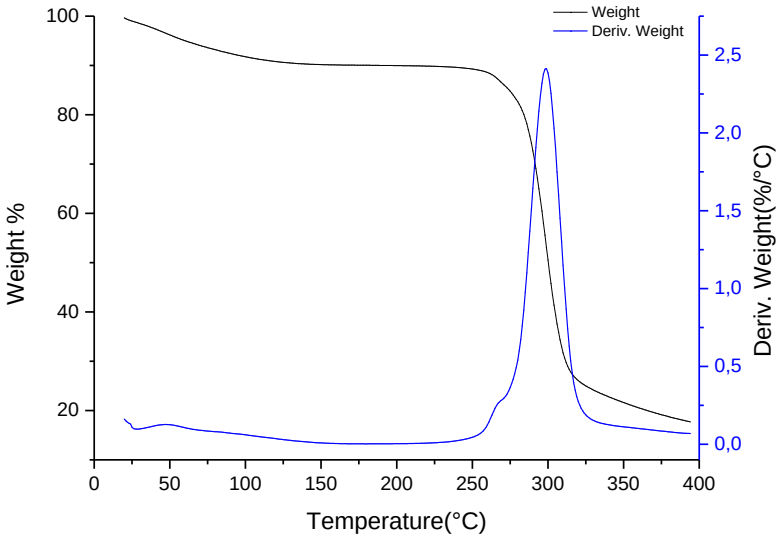


Figure 3. TGA diagram of starch potatoes fibers

In thermogravimetric analysis, the loss in mass due to volatilization of the degradation products is monitored as a function of temperature. It is possible to observe the loss of humidity of starch potatoes microfibers at 100°C corresponding to 11% of loss of total weight. After evaporation, the weight of the fibers stay constant until 250°C, where it is observed the beginning of loss of the weight of the fibers that correspond to the beginning of decomposition temperature of the starch fibers. The blue line observed in the figure, correspond to the derivative of weight in function of temperature. Here the temperature of fast degradation of fibers at 304°C can be seen. The fast loss of weight occurred at 315°C, in this transition point the fibers have lost near of 60% as compared with the initial weight. This analysis indicates the maxim temperature for usefulness (250°C) that must be considered for the design of elements with this material.

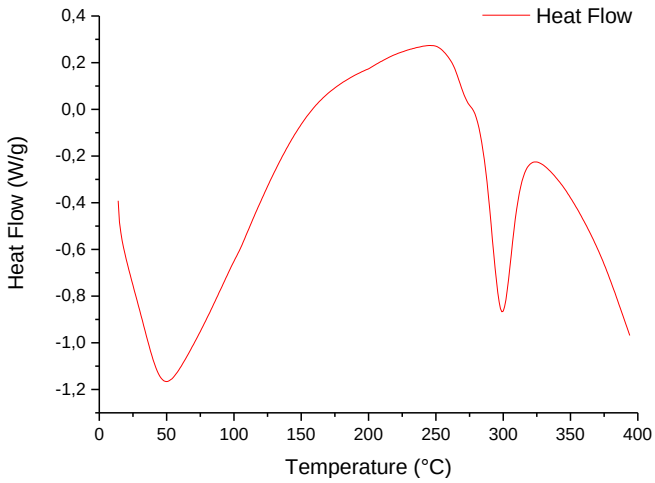


Figure 4. DSC of starch potatoes fibers.

In figure 4 it is possible to observe the energy absorptions that presents the native starch potatoes fibers with the increase of the temperature. Here the gelatinization temperatures of starch potatoes microfibers can be seen which are endothermic signals. The first signal appeared at 50°C, where the first stage of absorption of enthalpy energy of 81.16J/g is presented. This energy is absorbed by the fibers of starch for the dissociation of amylose (amorphous part) present in the starch. The second endothermic peak appeared at 303°C with enthalpy energy of 120 J/g. It occurs when this energy break the amylopectin bound. When the process increases the temperature, the fibers absorb the heat and generate the dissociation of amorphous phase (amylase). When the temperature is increasing, this generates the melting of a second component of starch potatoes, known, in this case, as amylopectin. The easy dissolution of amylase starch potatoes fibers at a low temperature happen because the hydrogen bonds are not that strong, while the bond of amylopectin is most stable, therefore it required higher temperature. Figure 4 confirms what is reported in several papers. It is to say that starch potatoes Diacol capiro (R-12) presents a high temperature resistance [26], so it is a good candidate for the fabrication of biodegradable material and industrial applications that require temperature above 100 C°.

3.3. Morphological analysis

The Morphological analysis of the fibers was carried out to four treatments of fibers. The Electro wet-spinning parameters used are shown in Table 2. In Figure 5 it is showed the micrograph taken to 4 treatments mentioned.

Table 2.Parameters used in the 4 treatments.

Parameters	Treatment 1	Treatment 2	Treatment 3	Treatment 4
Voltage (Kv)	10	10	8	8
Rate injection (ml/h)	2	2	2	4
Distance needle-collector (cm)	8	6	6	6

In figure 5 it can be observed that all fibers obtained present roughness, cross-linking and agglomerations in some areas. This can indicate the effects of electro wet-spinning process because despite the variety of possible conditions, the contact of the jet of solution of starch with the ethanol, in the moment of deposition in the collector, does not generate completely the solidification and then the fibers were still wet and it creates the cross-link between the fibers. On the other hand, the agglomerations are evidence of the no continuity in the process. Therefore some polymers leave the needles with major o less volume.

In the first treatment, it is possible to denote that the fibers are fused. This could be due to the presence of solvent in the time of deposition that was not evaporated completely in the process of spinning, as consequence of high voltage. In the fibers of second treatment, it can be observed roughness, inhomogeneous in the size of the diameter and defined fibers. In contrast with the first treatment, here the process had less time and therefore, the fibers are thicker (25 micrometers) than the first treatment (17 micrometers).

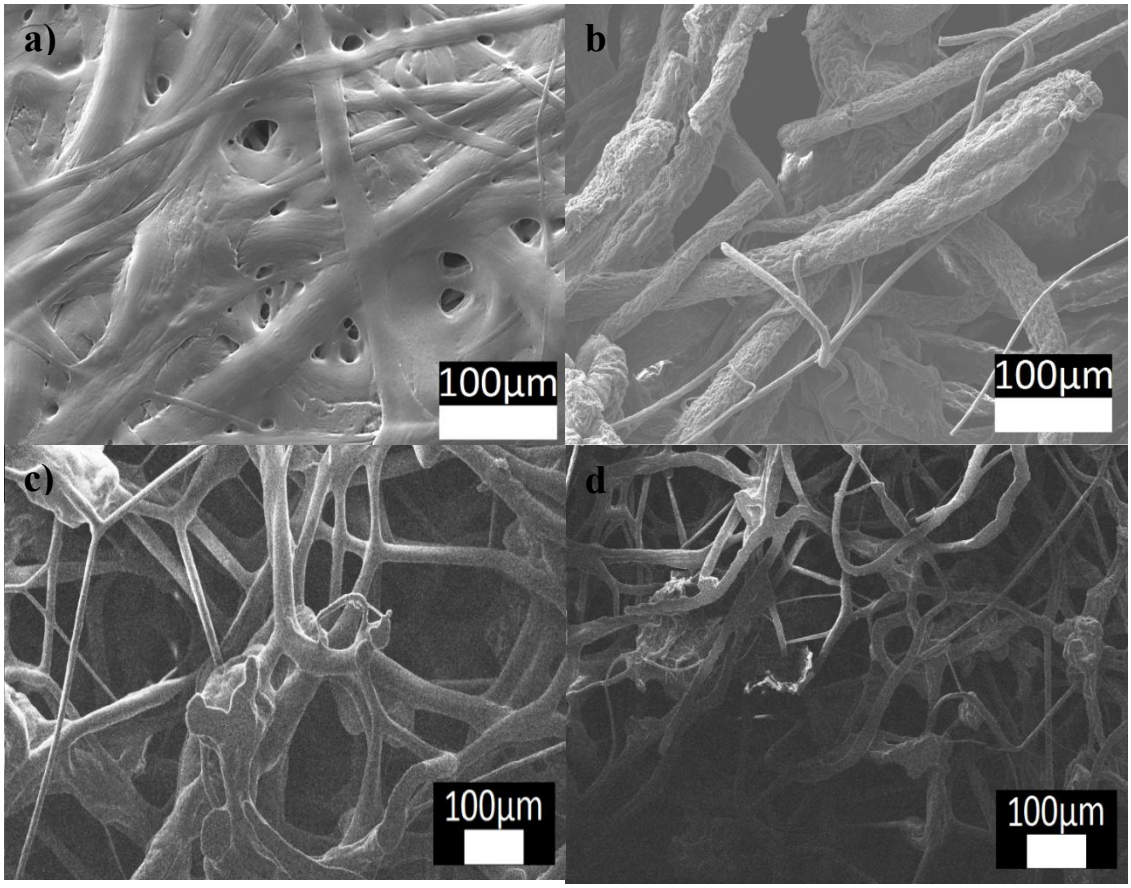


Figure 5. Micrograph of SEM starch potatoes fibers taken at the Instituto de Investigaciones en Materiales IIM of UNAM, a) treatment 1 (250X), b) treatment 2 (250X), c) treatment 3 (200X), d) treatment 4 (100X).

The fibers of the third treatment presented similar characteristic to second treatment such as continuous and defined fibers. Also it is possible to observe that the diameters of fibers in this treatment are more homogeneous, interlinking and smaller (15 micrometers) in comparison with the second treatment. This is explained because of the decrease of the voltage that allowed the jet of the solution to leave the capillary with less force and more time in the spinning. The fibers of the fourth treatment are similar to the third in the homogeneity in the diameters, the interlinking and they presented an increase in the diameters (25 micrometers). This is possible due to the increase in the rate of injection.

In studies carried out by Kong et al [31] with industrial corn starch, they obtained fibers with diameters between 1 and 5 micrometers, with a smooth morphology and homogeneous diameters. The difference with our results in the inhomogeneous morphology is due to the starch potatoes variety, Diacol Capiro (R12), presents different concentrations of amylose and amylopectin in comparison with starch corn. In consequence, it is generated a change in the viscosity of polymeric solution. In addition, these two components (amylose and amylopectin) influence in the starch thermal properties which was showed in the TGA. Another reason for this difference in diameter is due to the fact that our ethanol had a percentage of water that caused a time of solidification of fibers different.

The treatment with more homogeneity was treatment 3 and although the studies of Milasius et al [32] obtained fibers (125 nanometers) thinner in the order of nanometers, the fibers in our work were obtained from natural starch potatoes with voltage in the order of 6-8 Kv, while Milasius et al used voltage in the order of 75 Kv. They also used polyvinyl alcohol such dissolvent with addition with ethanol and collected the fibers with drum.

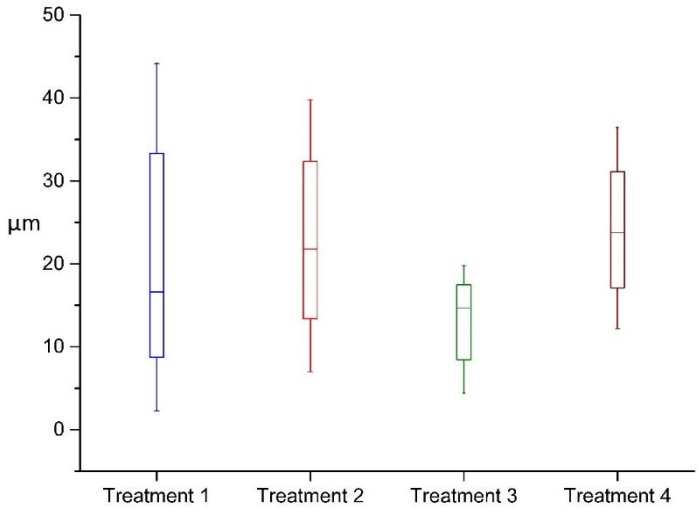


Figure 6. Boxplot about 4 treatments.

The analyses of diameter of starch potatoes fibers was measure by software ImageJ and the results are shown in figure 6 with the boxplot, where the upper diameters, the average and the lower diameter of the fibers in each treatment are represented. In figure 6 it can be observed that the third treatment with a voltage of 8 Kv, distance between needle and collector of 6 cm and rate of injection of 2 ml/h, presented the lowest diameter average (15 micrometer) and lowest variation (among 5 y 20 micrometers) in comparison with other treatments.

The treatment 1showed a mean diameter of 17 micrometer, similar to the treatment 3, but showed a more variation (3 - 44 micrometers). This difference in the variation may be due to the fact that the first treatment used higher voltage (10 Kv) with distance 8 cm generate more mobility of the fibers in the path between needle and collector and as a consequence the fibers are deposited in several places of the collector and it generates the variation of diameters of fibers.

The treatment 4 (8 Kv, 6 cm and 4 ml/h) generates an average diameter of 25 micrometers that exceeds the others treatments. Here the only difference in the treatment is in the increase of rate of injection of 2 ml/h, which demonstrates the influence of the rate injection about the diameter of starch potatoes fibers. Such influence may explain that higher rate injection causes major volume of the solution in the needle, therefore the force generated by the field electric does not decrease diameter of jet generating an increase in the diameter of the fibers deposited in the collector. However, in this case the variation of diameters is lower in comparison with the treatment 2, this is due to more voltage that makes the polymer accelerates toward to collector. Then, the fibers are deposited faster and dispersed without enough time for stretching.

4. Conclusions

This study proves that native potato's fibers from the Region of Boyacá Colombia, with diameters in the size of micrometers can be obtained. It also shows the effect of the three parameters used in the

electro wet spinning, being the parameters of the third treatment the one that showed homogeneous continuous fibers, and high interlinking. It also notes that the deposition and washing with ethanol for the separation of solvent of the fibers, in the electrospinning process, was fundamental to obtain fibers. It was also noted that after the electrospinning, the fibers do not showed a change in the chemical structure as evidenced with the FTIR, Besides that, the test of DSC and TGA evidence that the fibers show a high resistance to heat (304°C is the maxim temperature of degradation), which is of quite important for the use of this material in the industry. Because the maxim temperature for useful found for the starch potatoes microfibers was 250°C that must be considered for design of elements with this material

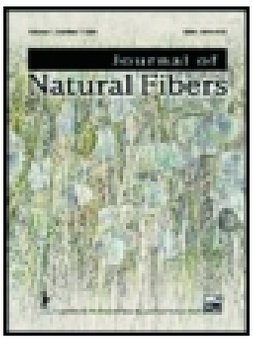
5. Acknowledgments

The present study was carried out under the cooperation agreement between UPTC - IIM-UNAM and it was supported by the projects PAPIIT-UNAM/IN108930, CONACYT/ CNPq174247 in México and the projects at UPTC with SGI codes: 1573 y 1769 in the UPTC-Colombia.

References

[1] Huang Z-M et al 2003 A review on polymer nanofibers by electrospinning and their applications in nanocomposites *Composites Science and Technology*. **63** 2223-2253
[2] Chronakis IS 2015 Micro- and Nano-fibers by Electrospinning Technology: Processing, Properties, and Applications, in Micromanufacturing Engineering and Technology (Second Edition), Y Qin, Editor., William Andrew Publishing: Boston **22** 513-548
[3] Kim IG et al 2015 A comprehensive electric field analysis of cylinder-type multi-nozzle electrospinning system for mass production of nanofibers *Journal of Industrial and Engineering Chemistry*. **31** 251-256
[4] Deitzel JM et al 2001Controlled deposition of electrospun poly(ethylene oxide) fibers *Polymer*. **42** 8163-8170
[5] Fong H, I Chun and DH Reneker 1999 Beaded nanofibers formed during electrospinning. *Polymer.***40** 4585-4592
[6] Morton WJ 1902 Method of dispersing fluids, *Google Patents*
[7] Cooley J 2006 *Improved methods of and apparatus for electrically separating the relatively volatile liquid component from the component of relatively fixed substances of composite fluids*. United Kingdom Patent, 1900. **6385** 19
[8] Cooley JF, *Apparatus for electrically dispersing fluids*. 1902, Google Patents.
[9] Pant, HR et al 2011 Photocatalytic and antibacterial properties of a TiO2/nylon-6 electrospun nanocomposite mat containing silver nanoparticles *Journal of Hazardous Materials* **189** 465-471
[10] Pant HR et al 2013 Synthesis, characterization, and mineralization of polyamide-6/calcium lactate composite nanofibers for bone tissue engineering. *Colloids and Surfaces B: Biointerfaces*. **102** 152-157
[11] Burger, C, BS Hsiao, and B Chu 2006 nanofibrous materials and their applications. *Annual Review of Materials Research*. **36** 333-368
[12] Neppalli R et al 2013 The effect of clay and of electrospinning on the polymorphism, structure and morphology of poly(vinylidene fluoride) *European Polymer Journal* **49** 90-99
[13] Neppalli R et al 2010 Poly(ε-caprolactone) filled with electrospun nylon fibres: A model for a facile composite fabrication *European Polymer Journal* **46** 968-976

[14] Unnithan AR et al 2012 Wound-dressing materials with antibacterial activity from electrospun polyurethane-dextran nanofiber mats containing ciprofloxacin HCl *Carbohydrate Polymers* **90** 1786-1793
[15] Silva RM et al 2016 Dental glass ionomer cement reinforced by cellulose microfibers and cellulose nanocrystals *Materials Science and Engineering: C* **58** 389-395
[16] Sonia A and K Priya Dasan 2013 Celluloses microfibers (CMF)/poly (ethylene-co-vinyl acetate) (EVA) composites for food packaging applications: A study based on barrier and biodegradation behavior *Journal of Food Engineering* **118** 78-89
[17] Rodrigues, A and M Emeje 2012 Recent applications of starch derivatives in nanodrug delivery *Carbohydrate Polymers* **87** 987-994
[18] Torres FG et al 2011 Biocompatibilty of starch-based films from starch of Andean crops for biomedical applications *Materials Science and Engineering: C* **31** 1737-1740
[19] Hung PV, NL Vien and NT Lan Phi 2016 Resistant starch improvement of rice starches under a combination of acid and heat-moisture treatments *Food Chemistry* **191** 67-73
[20] Buddrick O et al 2015 The effect of fermentation and addition of vegetable oil on resistant starch formation in wholegrain breads *Food Chemistry* **180** 181-185
[21] Moreno O L Atarés and A Chiralt 2015 Effect of the incorporation of antimicrobial/antioxidant proteins on the properties of potato starch films *Carbohydrate Polymer*s **133** 353-364
[22] Villamonte G, V Jury, and M de Lamballerie 2016 Stabilizing emulsions using high-pressure-treated corn starch *Food Hydrocolloids* **52** 581-589
[23] Yangcheng H et al 2015 Pysicochemical properties of tibetan hull-less barley starch *Carbohydrate Polymers* **137** 10
[24] Rosicka - Kaczmarek J et al 2016 Composition and thermodynamic properties of starches from facultative wheat varieties *Food Hydrocolloids* **54 Part A** 66-76
[25] Barichello V et al 1990 Low Temperature Sweetening in Susceptible and Resistant Potatoes: Starch Structure and Composition *Journal of Food Science* **55** 1054-1059
[26] Pardo Cuervo, OH, JC Castañeda Mancipe and CA Ortiz 2014 Caracterización estructural y térmica de almidones provenientes de diferentes variedades de papa. **62** 7
[27] Fang JM et al 2002 The preparation and characterisation of a series of chemically modified potato starches *Carbohydrate Polymers* **47** 245-252
[28] Fang JM et al 2004 The chemical modification of a range of starches under aqueous reaction conditions *Carbohydrate Polymers* **55** 283-289
[29] Kačuráková M and RH Wilson 2001 Developments in mid-infrared FT-IR spectroscopy of selected carbohydrates *Carbohydrate Polymers* **44** 291-303
[30] Chi H et al 2007 Synthesis of dodecenyl succinic anhydride (DDSA) corn starch Food *Research International* **40** 232-238
[31] Kong L and GR Ziegler 2014 Fabrication of pure starch fibers by electrospinning *Food Hydrocolloids* **36** 20-25
[32] Milašius R 2010 Investigation of the Possibility of Forming Nanofibres with Potato Starch *Fibres & Textiles in Eastern Europe* **18** 82



Journal of Natural Fibers

ISSN: 1544-0478 (Print) 1544-046X (Online) Journal homepage: http://www.tandfonline.com/loi/wjnf20

Comparative Study of Starch Fibers Obtained by Electro-spinning of Indigenous, Commercial and Cationic Potato Starch

Cárdenas William A, Muñoz Prieto Efrén, Gómez-Pachón Edwin Yesid & Vera-Graziano Ricardo

To cite this article: Cárdenas William A, Muñoz Prieto Efrén, Gómez-Pachón Edwin Yesid & Vera-Graziano Ricardo (2018): Comparative Study of Starch Fibers Obtained by Electro-spinning of Indigenous, Commercial and Cationic Potato Starch, Journal of Natural Fibers, DOI: 10.1080/15440478.2018.1534189

To link to this article: https://doi.org/10.1080/15440478.2018.1534189

Published online: 30 Oct 2018.

Submit your article to this journal

Article views: 1

View Crossmark data

Full Terms & Conditions of access and use can be found at
http://www.tandfonline.com/action/journalInformation?journalCode=wjnf20

JOURNAL OF NATURAL FIBERS
https://doi.org/10.1080/15440478.2018.1534189

Taylor & Francis
Taylor & Francis Group

Check for updates

Comparative Study of Starch Fibers Obtained by Electro-spinning of Indigenous, Commercial and Cationic Potato Starch

Cárdenas William A[a], Muñoz Prieto Efrén[a], Gómez-Pachón Edwin Yesid[a,b], and Vera-Graziano Ricardo[c]

[a]Escuela de Ciencias Químicas, Facultad de Ciencias, Grupo de investigación en desarrollo y aplicación de nuevos materiales, Universidad Pedagógica y Tecnológica de Colombia, Tunja, Colombia; [b]Escuela de Diseño Industrial, Universidad Pedagógica y Tecnológica de Colombia, Duitama, Colombia; [c]Instituto de Investigaciones en Materiales, Universidad Nacional Autónoma de México, Ciudad de México, México

ABSTRACT

By using the electro-spinning process on natural polymers, it is possible to obtain biodegradable membranes with potential applications in filters and scaffolds for tissue engineering. In this study, a comparison was made between the respective chemical, physical and thermal properties of the fibers from two sources of starch: One derived from a local, indigenous variety of potato (Diacol Capiro), native to the Boyacá region of Colombia (from here on referred to as "local starch"); the other, commercially available starch. A cationization of fibers was also carried out on the two starches. Chemical, physical and thermal properties were analyzed by Fourier transform infrared (FTIR), scanning electron microscopy (SEM), X-ray diffraction (DRX), thermogravimetric analysis (TGA) and differential scanning calorimetry (DSC). The results showed the fibers were cationized with a highly amorphous state, with a heat resistance of 300°C from physicochemical changes generated in the fibers.

摘要

利用电纺丝技术在天然高分子材料上制备生物可降解膜，在组织工程用过滤器和支架中具有潜在的应用前景。在本研究中，对两种来源的淀粉纤维各自的化学、物理和热性能进行了比较：一种来源于当地土豆品种（DiacolCapiro），原产于哥伦比亚Boyac地区（在此称为"当地淀粉"），另一种是商业上可获得的淀粉。在两种淀粉上也进行了纤维的阳离子化。采用傅里叶变换红外光谱（FTIR）、扫描电镜（SEM）、X射线衍射（DRX）、热重分析（TGA）和差示扫描量热法（DSC）对材料的化学、物理和热性能进行了分析。结果表明，纤维经阳离子化后呈高度非晶态，其耐热性为300℃。

KEYWORDS

Starch; fibers; natural polymers; electro-spinning; biodegradable; cationization

关□词

淀粉; 纤维; 天然聚合物; 静电纺丝; 能进行生物降解的; 阳离子化

Introduction

The use of starch has become more common thanks to the development of micro and nanomaterials, which are fabricated by techniques such as electro-spinning. This technique represents a versatile route for manufacturing materials at the micro- and nanoscale (Ramakrishna 2005; Reneker and Chun 1996; Wendorff, Agarwal, and Greiner 2012). The recent interest in such materials is due to the new properties that are found in materials at this scale, which are not present in the same composition and structures of macroscopic size. Nano- and microfibers are primarily polymeric and have enormous potential to significantly improve current technologies, as well as to develop new

CONTACT Cárdenas William A. wcaguazaco@gmail.com Escuela de Ciencias Químicas, Facultad de Ciencias, Grupo de investigación en desarrollo y aplicación de nuevos materiales, Universidad Pedagógica y Tecnológica de Colombia, Tunja, Colombia

Color versions of one or more of the figures in the article can be found online at www.tandfonline.com/wjnf.

© 2018 Taylor & Francis

applications. These in turn have high surface reactivity, thermal and electrical conductivity, and superior mechanical properties as a result of their size (Brown and Stevens 2007; Gogotsi 2006).

Some studies have been carried out pertaining to the electro-spinning of starch combined with other polymers, as reported by Milašius et al. (Milašius 2010), making use of starch, polyvinyl alcohol (PVA) and ethanol with electro-spinning equipment with voltages between 35 and 75 Kv and a rotatory collector. The concentration of starch in the solution generated and the increase of viscosity in said solution, produced nanofibers with diameters between 250 to 320 nanometers. In another study, Wang H. et al. (Wang et al. 2011) prepare fibers of oxidized starch with poly(vinyl alcohol) of 380 nm by means of electro-spinning, demonstrating that a high concentration of starch in the solution notably affects the homogeneity of the fibers. Studies where the electro-spun nanofiber is produced using polycaprolactone and starch have also been carried out, such as Jukola et al. (Jukola et al. 2008), using a high concentration of starch and resulting in highly porous scaffolds. Electro-spinning with starch in multicomponent solutions was realized by Sunthornvarabhas et al. (Sunthornvarabhas et al. 2011), using solutions of polylactic acid (PLA) with dichloromethane (DCM) and solutions with cassava starch dissolved in dimethylsulfoxide (DMSO). They found defined fibers with homogeneous diameters.

Another way to obtain starch microfibers is through electro wet spinning, in which the collector is immersed in a liquid. This modification is performed in order to remove the solvent from the fibers and to obtain homogeneous microscale diameters. The first studies of wet electro-spinning with starch were carried out by Kong et al. (Kong and Ziegler 2012, 2013, 2014). The first study (Kong and Ziegler 2012) observed the relation between the concentration of solvent and concentration of starch. Another study of Kong et al. (Kong and Ziegler 2013) proved that the diameter of the fibers did not depend on the rate of injection. It also showed that the diameter increased when the starch concentration in the solution was increased. A further study by Kong et al. (Kong and Ziegler 2014) involved the preparation of corn starch fibers with diameters between 1 and 5 microns. Using a solution of ethanol and water with heat, they improved the thermal transitions of the fibers at temperatures of 65°C and 114°C and also improved the crystallinity to 43%, a higher percentage when compared to untreated fibers.

The study realized by Cardenas et al. (Cárdenas et al. 2016) demonstrated how fibers of locally extracted starch (from a variety of potatoes endemic to the Boyacá region of Colombia) were obtained using wet electro-spinning. The starch did not present chemical changes after electro-spinning, and resulted in fiber diameters below 50 micrometers, with a high degree of crosslinking and high heat resistance. Besides the previous study of Cardenas et al. (Cárdenas et al. 2016), there have been no studies carried out to obtain fibers with diameters on the micrometer scale using starch obtained from potatoes native to the Boyacá region of Colombia; nor have there been studies characterizing cationized starch fibers in order to improve the thermal properties of the polysaccharide (Siau et al. 2004).

This study was carried out to define both the electro-spinning parameters necessary to obtain starch fibers from a particular endemic variety of potatoes, as well as the physicochemical and structural properties generated by the process of potato starch fiber cationization.

Experiment

Materials

This study was conducted on both starch made from the Diacol Capiro variety of potatoes (21–23% amylose) and commercial potato starch purchased from Sigma-Aldrich (18–20% amylose). The dimethylsulfoxide (99%), used to prepare the starch solutions, was purchased commercially from Merck. The ethanol (99.8%) and the cationizing agent chloride 3-chloro-2-hydroxypropyl trimethyl ammonium (37%) were purchased from Sigma-Aldrich.

Preparation of spinning solution

The local and commercial starches were prepared by dissolving starch (10% w/w) in a 95% aqueous DMSO solution. This concentration references the research by Kong et al. (Kong and Ziegler 2013). The solutions were subjected to a water bath with a temperature of 90°C, being stirred constantly for 1 h (Kong and Ziegler 2014). Absence of bubbles in the syringe was checked, continuing then with the wet electro-spinning process, parameters for which were defined for each treatment.

Electro-spinning conditions

The fibers were obtained using different treatments in which the electrical potential was varied, as was the distance between needle and collector and the injection speed, as shown in Table 1. The treatments 1 to 6 show the parameters used in the fibers subjected to heat drying after electro-spinning; treatments 5 to 8 refer to the fibers which underwent ethanol washing after wet electro-spinning; treatments 9 and 10 are fibers cationized by microwaves.

Post electro-spinning

The post wet electro-spinning process tends to be crucial to obtain fibers with a uniform diameter at the micro and/or nanoscale. One process involved immediately drying the fibers obtained at a temperature of 40°C for 3 h (heat drying); the other process was to leave the fibers in ethanol for 15 min and wash them three times with ethanol (ethanol washing). The fibers obtained were then deposited in a desiccator with Drierite for the respective characterizations.

Fiber cationization process

The fiber cationization of the starch was carried out by preparing a sodium hydroxide ethanol solution at a concentration of 10% w/w. Subsequently, 3-chloro-2-hydroxypropyl trimethylammonium chloride (CHPTAC) was added with a molar ratio of 1 chloride hydroxide (Contreras Lozano, Salcedo Mendoza, and Estrada Garrido 2013). Starch fiber was immersed in this solution and placed in the microwave with control of temperature, time and power (MLW WSO 100 S1086) for 10 min at a temperature of 60°C and 600 watts (Munoz, Palacios, and Rius 2012). Finally, the fibers were stored in a desiccator with Drierite to remove moisture.

Table 1. Electro-wet spinning parameters of starch.

Treatment	Voltage (Kv)	Distance (cm)	Rate of Injection (ml/h)
1[a,c]	9	6	4
2[a,c]	10	7,5	1
3[b,c]	12	7	1
4[b,c]	12	12	4
5[a,d]	7,5	8	4
6[a,d]	10	8	4
7[a,d]	9	6	4
8[a,d]	12	12	2
Cationized			
9[a,d]	9	6	4
10[a,d]	7,5	6	4

a: "homegrown" starch
b: commercial starch
c: heat dried
d: washed with ethanol

Morphological analysis

The morphology and porosity analysis, as well as the images for determining the diameters of the fibers, were obtained using scanning electron microscopy (SEM). The micrographs were obtained at the Institute for Research and Innovation in Science and Technology of Materials (INCITEMA, JEOL-JSM-7600F), located at the Pedagogical and Technological University of Colombia (UPTC) and the Institute of Materials Research (IIM, ZESS-MEB-EVO10) of the National Autonomous University of Mexico (UNAM). The measurement of fiber diameters was determined solely by means of ImageJ software.

Infrared analysis

The chemical changes of the pure starch present after electro-spinning and the changes to the starch fibers after the cationization process were determined by FTIR, through the use of the ATR-Thermo Scientific Nicolet IS50 unit. For this analysis, the fibers were directly analyzed without further treatment.

Crystallographic analysis

The starch fiber X-ray diffraction study was carried out through a diffractometer (Siemens D-500) using a Cu tube. Data were collected in a 2θ range of 1 to 60° and at room temperature.

Thermogravimetric and differential scanning calorimetry (DSC) analysis

Thermogravimetric analysis (TGA) was carried out with the TGA Q5000 V3.15 Build 263 TGA Module machine and the DSC was carried out with the DSC Q2000 V24.10 Build 122 DSC Module machine.

Results

Morphological analysis

Morphological analysis of fibers with heat drying

In the micrographs numbered 1 to 4 Figure 1, a complete or partial fusion of the fibers can be observed due to the presence of residual solvent in the fibers (DMSO). Treatment 1 shows the presence of some fibers; however, these have melted and have a large diameter (>120 μm). Treatment 2, 3 and 4 shows a solid material with a fracture, indicating complete fusion of the starch on the collector.

Morphological analysis of fibers washed with ethanol

Given the images obtained in the Figure 2, washing with ethanol after electro-spinning is important for obtaining fibers with micrometric diameters. Overall, the fibers obtained have a diameter of less than 100 microns, and only in some treatments (such as Treatment 6) are some agglomerations of starch observed, which are due to traces of solvent in the fibers.

The fibers of treatment 5–7 presented roughness, similar to that presented in the study reported by Cardenas et al. (Cárdenas et al. 2016). The difference between the diameter of the fibers from local starch and commercial starch may be the result of how the starch type is combined with the wet electro-spinning parameters. In Treatment 8, short fibers with less than one micron of diameter were obtained by being deposited in the bulk polymer; however, these fibers exhibit high rigidity and low crosslinking, which is indispensable to manufacture materials such as scaffolds, filters and sensors.

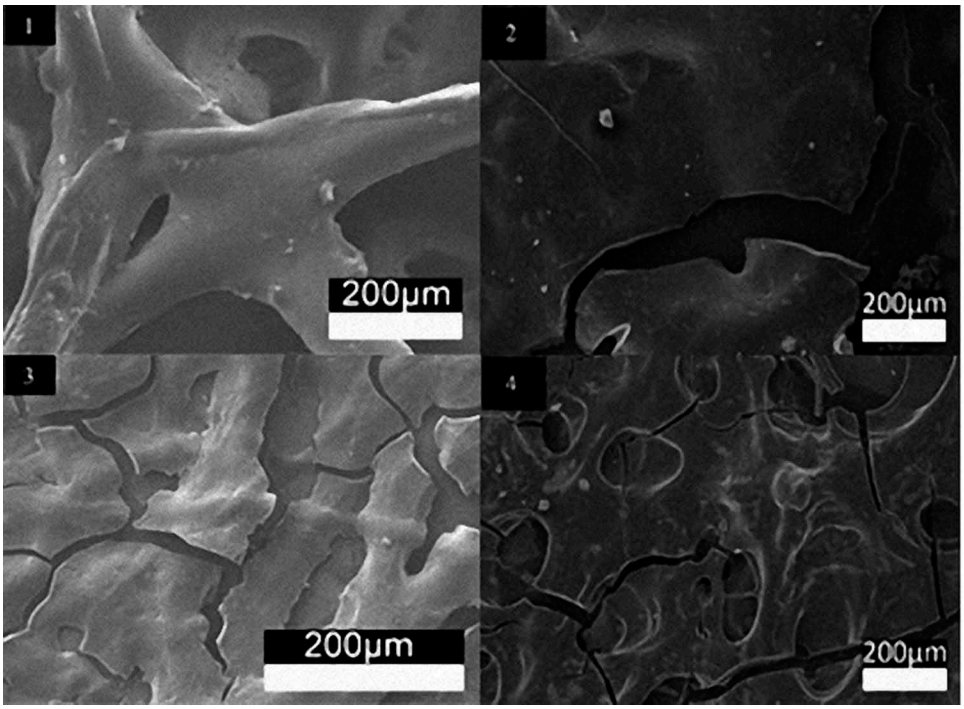


Figure 1. Scanning electron micrographs of fibers obtained with treatments 1 to 4 with heat drying.

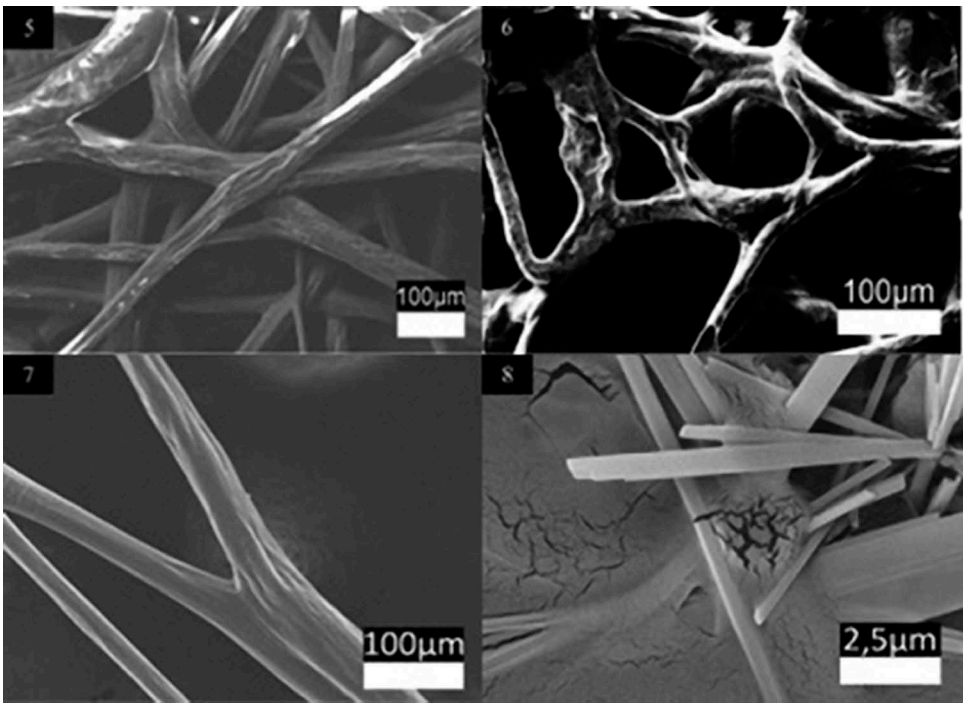


Figure 2. Scanning electron micrographs of the fibers of the treatments 5 to 8.

Table 2. Diameter of fiber washed with ethanol.

Treatment	Average Diameter (μm)	Standard Deviation	Type of Starch
5	24,16	± 11 μm	Native
6	26,66	± 20 μm	Native
7	34,34	± 12 μm	Commercial
8	0,46	± 0,2 μm	Commercial

Table 3. Average diameters of the cationized starch fibers.

Cationized	Average Diameter (μm)	Standard Deviation	Type of Starch
9	42,73	± 22 μm	Native
10	41,55	± 21 μm	Commercial

According to fiber diameters, as reported in Table 2 and Table 3, the local starch fibers have a smaller diameter (24.16–26.66 micrometers) compared to commercial starch fibers (34.34 micrometers), at 24.4% lower.

Kong et al. (Kong and Ziegler 2014) reported obtaining smooth and continuous fibers using mostly corn starch. They also found some fractures in the fibers which they attributed to their fragility. In the results shown by Cardenas et al. (Cárdenas et al. 2016), smooth and rough fibers are shown, the latter property being the result of the type of starch used in the wet electro-spinning process.

In accordance the fibers obtained in heat drying and washing ethanol, this latter is the essential process due to the ethanol eliminate the residual solvent into the fibers and so, is possible observed defined fibers with micrometric diameters.

Morphological analysis of cationized starch fibers

Regarding the micrograph of the two cationized starch fibers (Figure 3), when compared to the fibers that did not undergo cationization, it is possible to see that the external morphology is not altered. In terms of diameters, there is a big difference compared with fibers that were not cationized, so this process generates an increment of about 40%. This may also be possible because this process, by incorporating structure groups within the starch, may generate a slight increase in the final diameter of the fibers. The lowest diameter was obtained with the commercial starch, which may indicate that this kind of starch is less sensitive to the cationization process in comparison to the local type.

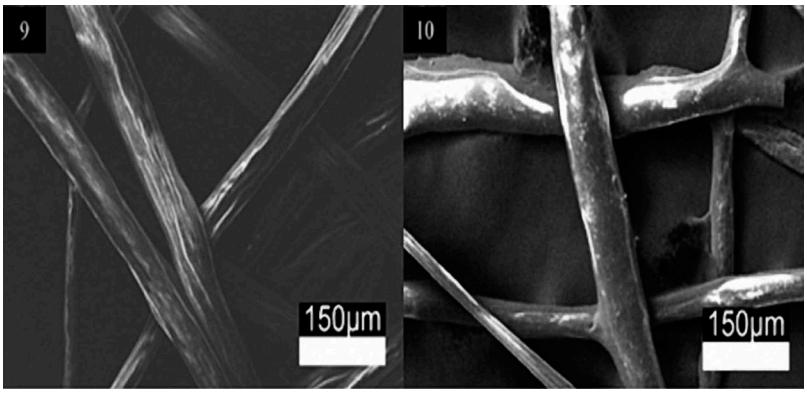


Figure 3. Micrograph of cationized starch fibers: (9) local and (10) commercial.

Chemical analysis

Cardenas et al. (Cárdenas et al. 2016), studied the starch fibers obtained from the wet electrospinning process and found that this process is completely safe for polymers such as potato starches. By means of this analytical technique, it was possible to observe the cationic groups incorporated into the structure of the starch (Figure 4).

The infrared spectra of the two types of fibers show some variation in signals. The presence of the intense signal at 1436 cm-1 in the fibers of cationized starch is assigned to the stretching of the C-N group. The peak at 3300 cm−1 is due to the O–H stretching vibration; the bands at 3050 and 1180 are due to the C–H stretching and C–O stretching vibrations, respectively. The signal at 1690 cm−1 is due to the first overtone of O–H bending. Two bands at 1030 and 1011 cm−1 are because of the CH2–O–CH2 stretching vibration. According to what has been reported in studies, the stretching and deformation vibrations of the CH_3 groups found in the trimethylammonium are to be expected in the 3100 to 3020 cm −1 range, with another signal at 1477 cm-1 (Pal, Mal, and Singh 2005).

Crystallographic analysis

In the diffractogram corresponding to the starch fibers R12 (Figure 5a) a crystallographic structure of starch cannot be seen. However, the fibers presented a signal at 20°, which is due to the compact hexagonal structure of amylopectin (McPherson and Jane 1999). After cationization, the signal of local starch fibers (Figure 5b) loses its intensity, difference that could indicate that the incorporation of the cationic groups into the starch structure drastically modify the ordered structure of amylopectin, which leads to higher material amorphicity.

The commercial starch fibers (Figure 5c) do not present a big difference when compared to that of local starch fibers. A signal close to 20° can be seen, showing a better definition in the spectrum,

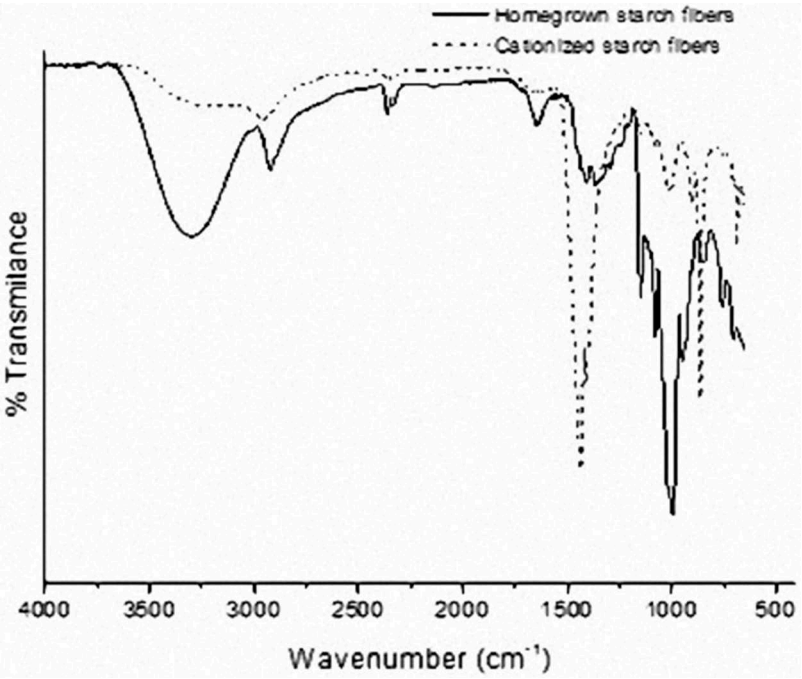


Figure 4. Infrared spectrum of local starch fibers and fibers of cationized starch.

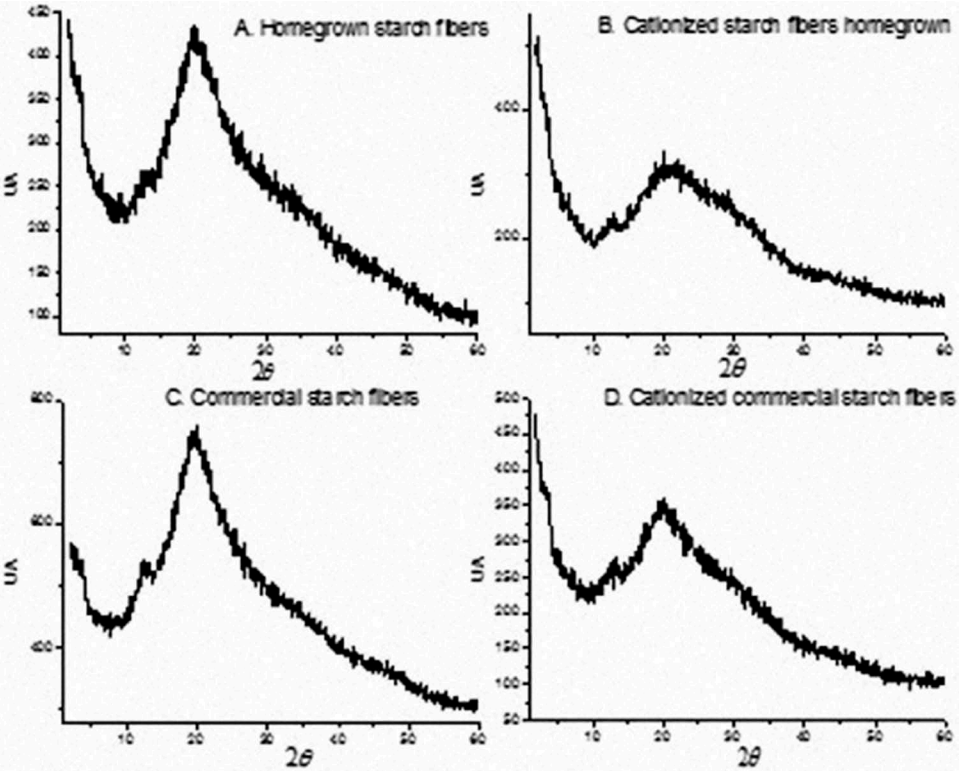


Figure 5. Diffractograms of fibers: local starch (a), cationized local (b), commercial starch (c) and cationized commercial starch (d).

possibly due to the purification process of this starch. By subjecting this commercial starch to cationization, the same thing happens as does with the fibers of local cationized starch.

Thermal degradation

In Figure 6a, the TGA analysis of the Aldrich starch fibers can be observed, showing a great similarity to the thermogram fibers R12 from potato starch reported by Cardenas et al. (Cárdenas et al. 2016). These fibers have an initial weight loss corresponding to 12% of their initial weight. This difference in the thermograms can be attributed to a higher concentration of impurities and moisture in these fibers. The weight of the fibers remains constant up to 245°C, temperature at which the fibers begin to lose weight. This process continues until they reach 316°C, which is quite similar to that observed in the local starch fibers. The great similarity these results show lead to the conclusion that the fibers from both the local and commercial starch possess high thermal stability, which gives potential use to either material in industry, medicine, and even food packaging in the way of reinforcements, given that these processes happen at temperatures below those at which the starch begins to degrade.

According to the thermogram of the Figure 6b, the fibers show weight loss up to 110°C as a consequence of moisture and volatile compounds. After this temperature, the fibers undergo another weight loss upwards of 150°C. It is stipulated that this new signal is due to the loss of the ammoniacal starch structure groups. This process occurs at a temperature of 240°C, since this temperature represents the last stage of decomposition of the starch. This loss is up to 325°C, 297° C being the temperature for rapid degradation. As stated above, it may indicate that the fibers of cationized starch have slightly lower temperature resistance.

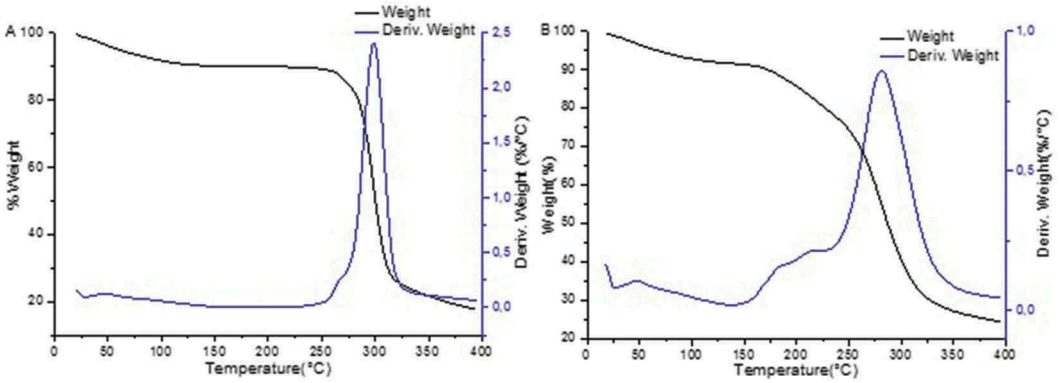


Figure 6. Thermogravimetric analysis of fibers: (a) commercial starch and (b) cationized starch.

Thermal transitions

The thermograms of commercial and local starch fibers are shown in Figure 7, demonstrating the material suffering the thermal transitions of heat application. By observing the DSC of the local and commercial starch fibers, one can notice three signals, two endothermic and one exothermic. The starch fibers present the first transition of gelatinization at temperatures between 50°C and 55°C, this temperature being reported as the solubilization temperature of the amorphous phase of starch (amylose) (Montoya López and Giraldo Giraldo 2010; Rodríguez, San Martín, and González de la Cruza 2001; Shiotsubo and Takahashi 1986; Tester and Debon 2000) due to the weakness of the hydrogen bonds of this structure.

In addition to the temperature factor, there may be the evaporation of volatiles and moisture present in the fibers. This signal found shows a similarity to those presented in the thermal analysis of potato starch by Shiotsubo et al. and Pardo et al. (Pardo Cuervo, Castañeda Mancipe, and Ortiz 2014; Shiotsubo and Takahashi 1986). After this energy absorption, fibers from both types of starch have an exothermic peak, also called crystalline, at 250°C and 256°C, respectively. This signal is given to a crystalline structure that occurs in the fibers when subjected to temperatures above 200°C. These results confirmed it to be the semi-crystalline structure of biodegradable polymers reported by Gomez et al. (Gómez-Pachón, Vera-Graziano, and Campos 2014), that correspond to the presence of the defined peaks in the DRX of local and commercial starch fibers.

The melting of the crystal structure of amylopectin (Montoya López and Giraldo Giraldo 2010; Rodríguez, San Martín, and de la Cruza 2001; Shiotsubo and Takahashi 1986; Tester and Debon 2000) is stipulated to be found in the endothermic signal at 299°C and 303°C for the fibers of local starch and

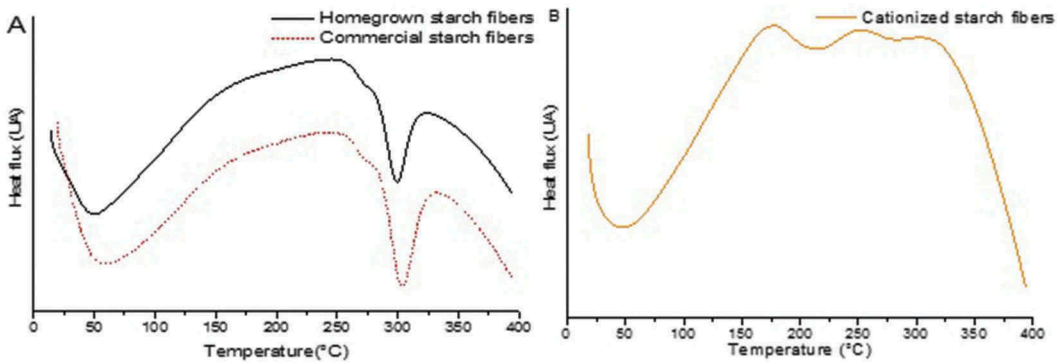


Figure 7. Differential scanning calorimetry of the fibers: (a) local and commercial starch, (b) cationized starch.

Table 4. Temperatures and energies of homegrown and commercial starch fibers.

	First Endothermic Peak		First Exothermic Peak		Second Endothermic Peak	
Type of Starch	Tp (°C)	ΔH (J/g)	Tp (°C)	ΔH (J/g)	Tp (°C)	ΔH (J/g)
Native Starch Fibers	49,59	70,0	250,9	53,5	299,35	118,8
Commercial Starch Fibers	55,86	80,2	256,8	58,6	303,50	126,0

Table 5. Energies and temperatures founded in the DSC analysis of cationized starch fibers.

	First endothermic peak		Second endothermic peak		Third endothermic peak	
Type of starch	Tp (°C)	ΔH (J/g)	Tp (°C)	ΔH (J/g)	Tp (°C)	ΔH (J/g)
Fibers cationized starch	45,69	60,05	212,39	47,97	280,47	8,30

commercial starch respectively. It was found that these values differ significantly from the results found by Montoya et al. (Montoya López and Giraldo Giraldo 2010), where a melt temperature of amylopectin potato starch at 200°C was found. The more heat-resistant fibers here can be attributed to very low moisture content, as moisture in the starch can generate a shift of the melting temperature of amylopectin to higher values.

Temperatures and energies found for the fibers of local and commercial starch are described in Table 4.

Regarding the DSC analysis of cationized starch fibers Table 5, a new endothermic signal is presented in comparison with the fibers found in unmodified starch. The DSC obtained cationized starch fibers (Figure 7b), with three endothermic signals corresponding to the gelatinization of amylose and amylopectin at 45°C and 280°C, respectively. The new found endothermic signal at 212°C is related to the melting process and separation of the cationic groups of the glycosidic chain, showing a great similarity to the thermal analysis of cationic starch by Muñoz et al. (Munoz, Palacios, and Rius 2012).

Figure 7b also shows the lower energy absorption region of the crystalline starch in the cationized melting fibers (8.3 J/g), compared to the energy of the fibers of local and commercial starch (118 and 126 J/g). This may be caused by the incorporation of cationic groups, which when detached at 212°C, decrease the structural stability of amylopectin.

These results show the difference in the thermal properties between cationized fibers in comparison with starch fibers (local and commercial). The cationized fibers present less thermic resistance according to the temperature of the first signal in the TGA and DSC analysis. This indicates that the cationized fibers have low stability, and therefore can have less degradation time in the environment.

Conclusions

We obtained electro-spun fibers with diameters below 50 micrometers, using both local and commercial starch and ethanol as the solvent in the wet electro-spinning process. Through infrared spectroscopy, the effectiveness of the microwave cationization method was demonstrated. Both types of cationized and non-cationized fibers are amorphous; however, non-cationized fibers present a higher degree of amorphicity. By means of DSC and TGA analysis, it was possible to observe that cationized starch fibers are less heat resistant, given the structural modification of polysaccharides.

Acknowledgments

To technical group members Josue Romero (SEM), Adriana Tejeda (DRX), Luis Paez (FTIR) and Jhon Riveros (TGA and DSC), who contributed in the characterization of the fibers obtained in the present investigation.

Funding

This work was supported by the UPTC.

References

Brown, P., and K. Stevens. 2007. *Nanofibers and nanotechnology in textiles*. Elsevier Science.

Cárdenas, W., E. Y. Gómez-Pachon, E. Muñoz, and R. Vera-Graziano. 2016. Preparation of potato starch microfibers obtained by electro wet spinning. *IOP Conference Series: Materials Science and Engineering* 138 (1):012001. doi:10.1088/1757-899X/138/1/012001.

Cuervo, P., O. Hernando, J. C. C. Mancipe, and C. A. Ortiz. 2014. Caracterización estructural y térmica de almidones provenientes de diferentes variedades de papa. *Acta Agronómica* 62 (4):7.

Gogotsi, Y. 2006. Nanotubes and Nanofibers. Taylor & Francis, CRC Press.

Gómez-Pachón, E. Y., R. Vera-Graziano, and R. Montiel Campos. 2014. Structure of poly(lactic-acid) PLA nanofibers scaffolds prepared by electrospinning. *IOP Conference Series: Materials Science and Engineering* 59 (1):012003. doi:10.1088/1757-899X/59/1/012003.

Jukola, H., L. Nikkola, M. E. Gomes, R. L. Reis, and N. Ashammakhi. 2008. Electrospun starch-polycaprolactone nanofiber-based constructs for tissue engineering. *AIP Conference Proceedings* 973 (1):971–74. doi:doi:10.1063/1.2896914.

Kong, L., and G. R. Ziegler. 2012. Role of molecular entanglements in starch fiber formation by electrospinning. *Biomacromolecules* 13 (8):2247–53. doi:10.1021/bm300396j.

Kong, L., and G. R. Ziegler. 2013. Quantitative relationship between electrospinning parameters and starch fiber diameter. *Carbohydrate Polymers* 92 (2):1416–22. doi:10.1016/j.carbpol.2012.09.026.

Kong, L., and G. R. Ziegler. 2014. Fabrication of pure starch fibers by electrospinning. *Food Hydrocolloids* 36:20–25. doi:10.1016/j.foodhyd.2013.08.021.

Lozano, C., K. Paola, J. G. S. Mendoza, and F. E. Garrido. 2013. Caracterización funcional de almidón catiónico de yuca (Manihot esculenta). *Revista ION* 26:31–38.

McPherson, A. E., and J. Jane. 1999. Comparison of waxy potato with other root and tuber starches. *Carbohydrate Polymers* 40 (1):57–70. doi:10.1016/S0144-8617(99)00039-9.

Milašius, R. 2010. Investigation of the possibility of forming nanofibres with potato starch. *Fibres & Textiles in Eastern Europe* 18 (5):82.

Montoya López, J., and G. A. Giraldo Giraldo. 2010. Caracterización físico-química de harina de trigo, masa y pan. *Reviews Invest University Quindío* 20:29–35.

Munoz, E., J. Palacios, and C. Rius. 2012. Microwave ans ultrasound activation effect on cationization of corn and potato starches. *Ciencia en Desarrollo* 4 (1):151–73.

Pal, S., D. Mal, and R. P. Singh. 2005. Cationic starch: An effective flocculating agent. *Carbohydrate Polymers* 59 (4):417–23. doi:10.1016/j.carbpol.2004.06.047.

Ramakrishna, S. 2005. *An Introduction to Electrospinning and Nanofibers*: World Scientific.

Reneker, D. H., and I. Chun. 1996. Nanometre diameter fibres of polymer, produced by electrospinning. *Nanotechnology* 7 (3):216. doi:10.1088/0957-4484/7/3/009.

Rodríguez, P., M. E. San Martín, and G. G. de la Cruza. 2001. Calorimetría diferencial de barrido y rayos-x del almidón obtenido por nixtamalización fraccionada. *Superficies Y Vacío. Soc. Mex. De Cien. Superficies Y Vacío* 13:61–65.

Shiotsubo, T., and K. Takahashi. 1986. Changes in enthalpy and heat capacity associated with the gelatinization of potato starch, as evaluated from isothermal calorimetry. *Carbohydrate Research* 158:1–6. doi:10.1016/0008-6215(86)84001-0.

Siau, C. L., A. A. Karim, M. H. Norziah, and W. D. Wan Rosli. 2004. Effects of cationization on DSC thermal profiles, pasting and emulsifying properties of sago starch. *Journal of the Science of Food and Agriculture* 84 (13):1722–30. doi:10.1002/(ISSN)1097-0010.

Sunthornvarabhas, J., P. Chatakanonda, K. Piyachomkwan, and K. Sriroth. 2011. Electrospun polylactic acid and cassava starch fiber by conjugated solvent technique. *Materials Letters* 65 (6):985–87. doi:10.1016/j.matlet.2010.12.038.

Tester, R. F., and S. J. J. Debon. 2000. Annealing of starch—A review. *International Journal of Biological Macromolecules* 27 (1):1–12.

Wang, H., W. Wang, S. Jiang, S. Jiang, L. Zhai, and Q. Jiang. 2011. Poly (vinyl alcohol)/oxidized starch fibres via electrospinning technique: Fabrication and characterization. *Iranian Polymer Journal* 20:551–58.

Wendorff, J. H., S. Agarwal, and A. Greiner. 2012. *Electrospinning: materials, processing, and applications*. Wiley.

Efectos del tratamiento térmico y del método de colección sobre la estructura cristalina de las nanofibras electrohiladas de ácido poli (láctico)

Effects of heat treatment and the method of collection on the crystal structure of the poly lactic acid electrospinned nanofibers

Edwin Gómez-Pachón[1*] Ricardo Vera-Graziano[2] Raúl Montiel[3]
William Cardenas-Aguazaco[4] Andrés Felipe Ochica[4]

Recibido 29 de octubre de 2017, aceptado 13 de septiembre de 2018
Received: October 29, 2017 Accepted: September 13, 2018

RESUMEN

Estudios anteriores indican que las nanofibras de ácido poli (láctico) (PLA) obtenidas por electrohilado reportan una baja resistencia mecánica. Por ello se pretende mostrar los cambios en las propiedades mecánicas de módulo de Young y resistencia a la tensión de las nanofibras de PLA por efectos del tipo de colección y de tratamiento térmico. Para ello se prepararon nanofibras de PLA por electrohilado colectadas aleatoria y ordenadamente con la aplicación de un tratamiento térmico a 80 ºC por 8 horas con el fin de incrementar el entrecruzamiento y la fase cristalina del andamio. Las nanofibras fueron caracterizadas por medio de microscopía electrónica de barrido (SEM), microscopía electrónica de transmisión (TEM), dispersión de rayos X a bajo ángulo (SAXS), calorimetría diferencial de barrido (DSC) y una evaluación a la resistencia a la tensión. Los resultados mostraron nanofibras orientadas con una estructura semicristalina claramente definida, con un menor diámetro promedio de fibra y un notorio aumento de resistencia a la tensión como del Módulo de Young en relación a las depositadas aleatoriamente. Por otra parte, el tratamiento térmico influenció en el diámetro promedio y la porosidad final del andamio, pero no generó un cambio notorio en las propiedades mecánicas en estudio. Por lo tanto, se concluye que el proceso de colección rotatorio genera un mayor ordenamiento molecular, incremento en las propiedades mecánicas en estudio, mientras el recocido extiende la cristalinidad de las nanofibras pero no afecta estas propiedades.

Palabras clave: Acido Poli (láctico), electrohilado, nanofibras, cristalinidad, propiedades mecánicas.

ABSTRACT

Previous studies indicate that poly (lactic acid) (PLA) nanofibers obtained by electrospinning report a low mechanical strength. Therefore, it is intended to show the changes in the mechanical properties of Young's modulus and tensile strength of PLA nanofibers due to the type of collection and thermal treatment. For this, PLA nanofibers were prepared by electrospinning collected randomly, and orderly with thermal treatment was carried out at 80 ºC for 8 hours to increase the cross-linking and the crystalline phase of the scaffolding. The nanofibers were characterized by means of scanning electron microscopy

[1] Grupo de investigación Diseño, Innovación y Asistencia Técnica de Materiales Avanzados DITMAV. Facultad Duitama. Universidad Pedagógica y Tecnológica de Colombia (UPTC), Carrera 18 con Calle 22, Duitama, Colombia. E-mail: edwin.gomez02@uptc.edu.co
[2] Instituto de Investigaciones en Materiales, UNAM Apdo. postal 70-360 Cd. Universitaria, CDMX, México. E-mail: graziano@unam.mx
[3] Departamento de polímeros. Universidad Autónoma Metropolitana-Iztapalapa (UAM-I), CDMX, México. E-mail: luar@xanum.uam.mx
[4] DANUM, Facultad de Ciencias Básicas. Universidad Pedagógica y Tecnológica de Colombia (UPTC). Avenida Central del Norte 39-115, Tunja, Colombia. E-mail: williamantonio.cardenas@uptc.edu.co; andres-felipe21@hotmail.com
* Autor de correspondencia: edwin.gomez02@uptc.edu.co

(SEM), transmission electron microscopy (TEM), low angle X-ray scattering (SAXS), differential scanning calorimetry (DSC), and stress evaluation. The results showed oriented nanofibers with a clearly defined semicrystalline structure and a smaller average fiber diameter and a notorious increase of tensile strength concerning those collected randomly. Additionally, the thermal treatment influenced the average diameter and the porosity of the scaffolding but did not generate a significant change in the mechanical properties. Therefore, it is concluded that the rotary collection process generates a higher molecular order, increase in the mechanical properties under study, while annealing extends the crystallinity of the nanofibers but does not affect these properties.

Key words: Poly Lactic Acid, electrospinning, nanofibers, crystallinity, mechanic properties.

INTRODUCCIÓN

La medicina regenerativa, es un campo interdisciplinario que combina los principios e innovaciones de la ingeniería y ciencias de la vida con el propósito de la mejora, reparación o sustitución de la función de un tejido u órgano [1]. En este campo de la ciencia se combinan células, andamios (matriz extracelular artificial) y tecnologías de diseño y fabricación de los nuevos tejidos u órganos, dado que cada tejido u órgano en nuestro cuerpo está compuesto de células del parénquima (células funcionales) y células madre mesenquimales (células de apoyo) contenidos dentro de una matriz extracelular (MEC) para formar un microambiente, los cuales en conjunto forman tejidos y órganos [2].

Entre las propiedades más importantes que deben poseer los andamios fabricados por electrohilado está la capacidad de promover la adhesión, crecimiento y diferenciación de células *in-vitro*, además de su biocompatibilidad, biodegradabilidad y soporte celular [2]. Para el desarrollo de andamios se han utilizado diferentes materiales tales como: sintéticos orgánicos (polímeros), sintéticos inorgánicos (hidroxiapatita, fosfato tricálcico, yeso, cerámica de vidrio), orgánicos de origen natural (colágeno, ácido hialurónico) e inorgánicos (hidroxiapatita) [3-7].

Los andamios celulares a base de fibras con diámetros nanométricos tienen varias ventajas en comparación con otro tipo de andamios. Por ejemplo, las nanofibras poseen mayor probabilidad de que se adhieran las células, así como una mejor porosidad para la entrada y salida de nutrientes, control de la degradación, entre otras. Sin embargo, dada su baja densidad y estructura requieren de propiedades mecánicas que permitan soportar todo el proceso que implica el desarrollo de los tejidos [8]. Las nanofibras poliméricas pueden presentar propiedades físicas, químicas y en algunos casos propiedades mecánicas similares a las que poseen algunos tejidos vivos (hueso, cartílago, músculo, venas y arterias). Además presentan propiedades como: elevada relación superficie/volumen, buena resistencia mecánica, posibilidad de funcionalizar su superficie y facilidad para adoptar la forma de un tejido, cuando se utiliza como andamio celular [1]. Las nanofibras poliméricas garantizan el soporte de las células durante un período de tiempo, para luego degradarse a medida que se obtiene el nuevo tejido, así como una respuesta biológica favorable del organismo receptor [9].

La técnica de electrohilado ha mostrado varias ventajas para fabricar redes o andamios de microfibras y nanofibras, ya que permite controlar el diámetro de las fibras, así como la estructura del andamio (dirección de nanofibras, porosidad, estructura, entre otros), lo que facilita la manufactura controlada de andamios celulares útiles en la ingeniería de tejidos [9, 10]. Los andamios poliméricos producidos por el proceso del electrohilado resultan ser una alternativa a los inconvenientes que presentan otros tipos de materiales porosos, que no permiten el desplazamiento de fluidos dentro de sus poros. El proceso de electrohilado ofrece la posibilidad de mejorar algunas propiedades de los polímeros para satisfacer los requerimientos mecánicos del andamio celular y del ambiente biológico al que va a estar sometido. Otra ventaja que presentan cuando el andamio se manufactura por electrohilado es su versatilidad para construir formas complejas en 2D y 3D [9, 11].

En estudios realizados con anterioridad se desarrolló un andamio con PLA e hidroxiapatita

para la regeneración dental, utilizando la técnica de electrohilado [12]. Se obtuvieron andamios de PLA mezclado e injertado con nano partículas de hidroxiapatita. Se lograron buenas propiedades mecánicas, químicas y biológicas, en comparación con otros andamios desarrollados hasta ese momento. Sin embargo, no se estableció una relación entre la caracterización estructural y sus propiedades mecánicas. Varios estudios se han enfocado en el análisis de las propiedades elásticas y resistencia a la tensión de nanofibras poliméricas [13, 14] y a la observación de la estructura superficial de nano y microfibras por técnicas como microscopía electrónica de barrido (SEM) [9], los cuales brindan algunas descripciones de la morfología, pero no han logrado hacer una correlación de la morfología interna de las nanofibras con sus propiedades elásticas, para usarse en el diseño de andamios celulares y materiales compuestos a base de nanofibras poliméricas.

El estudio reportado por You *et al.* [15], indica una disminución en el área de las fibras de PLA al ser sometidas a una temperatura de 180ºC, pero no se estudió el efecto de los diferentes tipos de colector y del tratamiento térmico de recocido sobre las estructura semicristalina interna de las fibras de PLA.

El objetivo del estudio consiste en evaluar el efecto generado en las nanofibras de acuerdo al método de colección y del tratamiento térmico. Para ello se utilizan diferentes técnicas analíticas para determinar los cambios morfológicos de las nanofibras de PLA, analizando específicamente los efectos sobre las propiedades estructurales cristalinas. Lo anterior pretende correlacionar estas propiedades morfológicas con las propiedades mecánicas, las cuales dan un avance significativo al desarrollo de andamios para la utilización en el campo de la ingeniería de tejidos.

MATERIALES Y MÉTODOS

Materiales

El PLA fue adquirido de Ingeo, Cargill Dow Co (división Natureworks 2002D) en forma de pellets. Para la obtención de los andamios de PLA fue utilizado el solvente 2,2,2-Trifluoroetanol (Nº CAS 75-89-8) el cual fue adquirido de Sigma-Aldrich a una concentración de 99%.

Electrohilado

Las soluciones de PLA fueron preparadas según la metodología usada por Vera *et al.* [12] usando 2,2,2-Trifluoroethanol (TFE) como solvente. Las soluciones fueron agitadas magnéticamente hasta lograr una solución homogénea. Los andamios se fabricaron utilizando el equipo de electrohilado (Figura 1) en el Instituto de Investigación en Materiales de la Universidad Nacional Autónoma de México (IIM-UNAM).

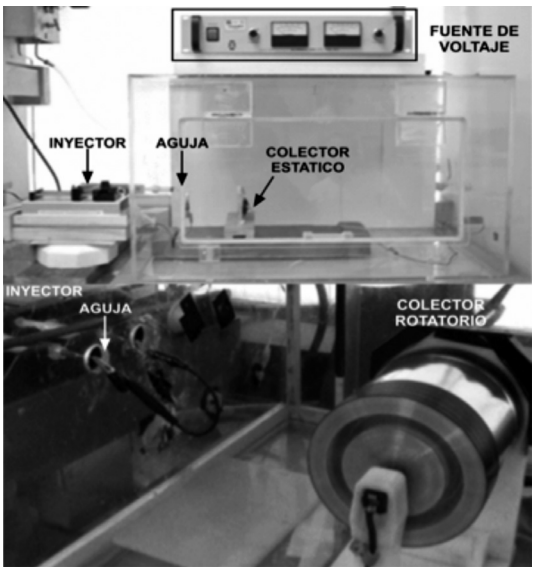


Figura 1. Equipo de electrohilado del IIM-UNAM.

Los parámetros utilizados en el electrohilado de las fibras colectadas aleatoriamente son descritos en la Tabla 1:

Tabla 1. Parámetros de electrohilado de las fibras colectadas aleatoriamente.

Parámetro	Valor
Distancia del colector al inyector	30 cm
Voltaje	15 KV
Velocidad de Inyección	0,6 ml/h
Temperatura del proceso	25 ºC

Para la obtención de las nanofibras de PLA ordenadas, se modificó el voltaje y la velocidad del colector rotatorio. Los valores son descritos en la Tabla 2.

Tabla 2. Parámetros de electrohilado usados en las fibras colectadas ordenadamente.

Voltaje (KV)	RPM	V_{tan} *(m/min)*
13,6	3491	1096.7
15	3876.9	1217.9
18	4703.6	1477.7

Tratamiento post electrohilado

Con el fin de mejorar las propiedades estructurales y mecánicas de las fibras, estas fueron sometidas a un proceso de calentamiento a 80 ºC durante 10 horas. La temperatura de este proceso fue dada de acuerdo a la temperatura de transición vítrea del polímero (Tg = 60 ºC), con lo cual se asegura un cambio en la estructura interna del polímero. Las muestras con post tratamiento térmico se presentan en los resultados como NAR (Nanofibras colectadas aleatoriamente recocidas) y NOR (Nanofibras colectadas ordenadamente recocidas).

Caracterización por SEM

Con la ayuda de la microscopia electrónica de barrido (SEM) fue posible observar los aspectos morfológicos, diámetro y porosidad de las nanofibras de PLA. Para tal fin fue utilizado el equipo JEOL-JSM-7600F (Japón) con filamento de Tungsteno, el cual poseen un cañón de electrones con un diferencial de 20.0 kV Para la realización de esta caracterización se tomó 0,5 cm^2 de las nanofibras obtenidas de los diferentes tratamientos descritos anteriormente. Para el análisis fue necesario recubrir con oro a un vacío de 10E-8 Torr con una corriente de 30 mA durante 5 minutos. Se tomaron dos fotografías de cada probeta en diferentes lugares con aumentos entre 1000x y 50000x. Con las imágenes obtenidas se realizó un análisis del diámetro y porosidad de las nanofibras mediante software Image J.

Caracterización por TEM

Con la Microscopía Electrónica de Transmisión (TEM) es posible observar los cambios de estructura interna de las nanofibras. Las nanofibras fueron encapsuladas en una resina epóxica (Epon® 812) y calentadas por tres días en un horno a 50 ºC. Posterior a este procedimiento, las nanofibras fueron cortadas en discos de 100 nm de espesor con un ultra micrótomo MRC-7000. Para obtener un buen contraste en las observaciones de TEM, las muestras fueron colocadas en un horno en presencia de tetróxido de rutenio durante 20 minutos, con el objetivo de oxidar el polímero y así poder observar claramente los contrastes entre las fases amorfas y las semicristalinas. El equipo utilizado en esta caracterización fue JEOL-2100f.

Caracterización por DRX y SAXS

La determinación de la estructura cristalina interna de las nanofibras fue llevada a cabo mediante caracterización por Dispersión de rayos X a bajo ángulo (SAXS), se empleó el equipo Xeuss SAXS/WAXS (Francia), el cual posee un tubo de rayos X Genix de baja divergencia y un detector Dectris pilatus 300K, con tubo de dispersión al vacío. Se usó el tubo de rayos X con un voltaje de 50 kV y una corriente de 0,6 mA. La emisión de rayos X fue de 120 segundos de exposición y la dispersión se realizó a ángulos inferiores de 1.

Este análisis se llevó a cabo al PLA en pellets, a las nanofibras colectadas aleatoriamente (NA) y a las nanofibras orientadas con una velocidad de 1480 m/min (NO 1480 m/min). La muestra de PLA y las nanofibras fueron analizadas con un espesor de la muestra de 0.5 mm, mientras que el tamaño de las muestras se ajustaron al diámetro por donde pasa el haz de rayos X.

Análisis por Calorimetría diferencia de barrido (DSC)

Las transiciones térmicas que presentan las nanofibras se determinaron por el equipo DSC 2910 TA Instruments. Las muestras se calentaron desde 0 ºC hasta 200 ºC a una rampa de calentamiento de 10 ºC/ min. Los termogramas obtenidos se analizaron por medio del software "TA Instruments Universal Analysis 2000".

Caracterización mecánica de los andamios de nanofibras de PLA

Se construyeron probetas ajustadas a la norma técnica ASTM D638, dado que actualmente no existe una norma específica para membranas de nanofibras. Se escogió esta norma porque está recomendada para membranas de materiales poliméricos con fibras reforzadas. Se usó la celda de carga de 50 gramos de fuerza de la empresa Honeywell Sensing & Control, Model 31 (Miniature Load Cell). Para el ensayo se utilizó el equipo universal de ensayo marca MTS minibionix 858. La velocidad del ensayo fue de 10mm/min. Los datos fueron procesados en

MatLab 2010®. Se probaron 5 probetas por cada tratamiento.

RESULTADOS Y DISCUSIÓN

Morfología por (SEM)

En un estudio realizado por Gómez *et al.* [16] se comparó el método de colección de las nanofibras de PLA, usando un colector rotacional y un colector fijo. En ese estudio se utilizó una velocidad rotacional de 1100 y 1217 m/min con el fin de determinar posibles cambios morfológicos y estructurales en las nanofibras. Se observó una relación en el diámetro de las nanofibras y la velocidad del colector, siendo a mayor velocidad mayor diámetro de las nanofibras. En el presente estudio se muestran los diámetros y la morfología de nanofibras de PLA obtenidas a una velocidad de 1480 m/min, además de los resultados obtenidos luego de realizar el proceso de calentamiento a las nanofibras. En la Figura 2 se puede apreciar las fibras obtenidas, encontrando una gran similitud respecto a la morfología de las fibras colectadas tanto aleatoria como ordenadamente. Las fibras no presentan microesferas (beads), fracturas o grietas, las cuales tienden a afectar las propiedades mecánicas de los andamios.

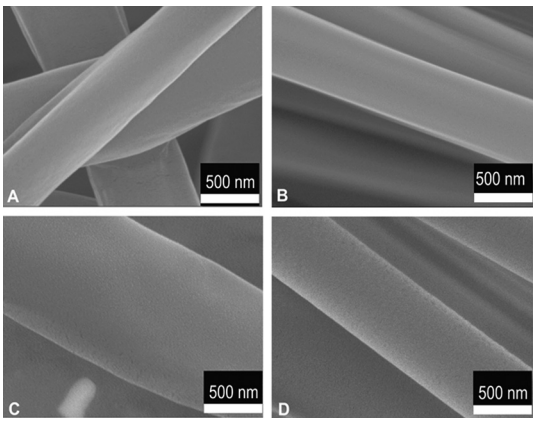


Figura 2. Micrografía electrónica de barrido de nanofibras: A. Colectadas aleatoriamente, B. Colectadas a 1100 m/min, C. Colectadas a 1217 m/min y D. Colectadas a 1480 m/min.

En la Tabla 3 se presentan los diámetros calculados de las nanofibras colectadas aleatoria y ordenadamente, así como de los diámetros de las nanofibras luego del proceso de recocido.

Tabla 3. Resultados de diámetro y porosidad en las nanofibras por microscopia electrónica de barrido.

Tipo de andamio	Diámetro promedio (nm)	Porosidad promedio (%)
NA[1]	992 +/- 25,7	37,6
NAR[2]	986 +/-21,1	44,3
NO[3] $_{1100\ m/min}$	643 +/-50	32,6
NOR[4] $_{1100\ m/min}$	562,884 +/-209,73	30,0
NO $_{1217\ m/min}$	747,04 +/-116,81	42,5
NOR $_{1217\ m/min}$	525,8 +/-90,44	40,7
NO $_{1480\ m/min}$	772 +/- 98	35,8
NOR $_{1480\ m/min}$	580+/- 90	34,2

[1] NA= nanofibras aleatorias.
[2] NAR= nanofibras aleatorias recocidas.
[3] NO= nanofibras ordenadas.
[4] NOR= nanofibras ordenadas recocidas.

Las nanofibras de PLA presentan una diferencia en los diámetros de las nanofibras colectadas ordenada y aleatoriamente, siendo estas últimas las de mayor diámetro promedio (992 nm) con una variación de 26 nm. Luego del recocido, estas nanofibras presentan un diámetro promedio de 986 nm con una variación de 21 nm, lo cual no indica un cambio significante en este parámetro. Sin embargo, se presenta un aumento del 7% en la porosidad de la membrana, la cual es atribuida al aumento de los espacios vacíos dada la disminución del diámetro de las nanofibras. En el caso de las nanofibras ordenadas colectadas a 1100m/min ($NO_{1100\ m/min}$) presentan un diámetro promedio de 643 nm, el cual es 350 nm menor que las obtenidas con el colector estacionario, luego del recocido estas fibras disminuyen 80 nm su diámetro promedio, así como disminuyen en un 2% la porosidad de la membrana. Esta disminución puede ser otorgada a la gran aglomeración de nanofibras en la membrana luego del tratamiento térmico, lo cual genera una disminución de las zonas oscuras en la imagen, parámetro por el cual se mide la porosidad de la membrana.

Con relación a las nanofibras colectadas a 1217 m/min ($NO_{1217\ m/min}$) se encuentra una disminución de 250 nm en el diámetro promedio en comparación con las nanofibras colectadas aleatoriamente y un aumento de 100 nm respecto a las nanofibras

colectadas a 1100m/min. Este incremento es otorgado a los parámetros de electrohilado como el potencial eléctrico y velocidad tangencial, los cuales al tener un mayor valor (15Kv y 1217m/min) tienen una gran influencia en el estiramiento del chorro expulsado por lo que el diámetro de las nanofibras aumenta. Al recocer las nanofibras de este tratamiento, el diámetro promedio y la porosidad de la membrana disminuye 220 nm y 2% respectivamente, siendo esto el resultado esperado dados los resultados obtenidos con las nanofibras colectadas a 1100 m/min.

Por último, el diámetro de las nanofibras colectadas a 1480m/min ($NO_{1480\ m/min}$) presenta una disminución en el diámetro promedio de 220 nm con relación a las nanofibras colectadas aleatoriamente y un aumento en esta variable de 130 y 30 nm en comparación con las nanofibras colectadas a 1100m/min y 1217 m/min respectivamente. Luego de realizar el tratamiento térmico a las fibras obtenidas a 1480 m/min, se presenta una disminución en el diámetro promedio de 200 nm aproximadamente, así como una leve disminución (1,6%) en la porosidad de la membrana, siendo esto similar a lo observado en las fibras obtenidas a menor potencial eléctrico y menor velocidad tangencial.

De acuerdo a estos resultados es posible notar un incremento en el diámetro de las fibras colectadas ordenadamente a medida que la velocidad tangencial y el potencial eléctrico aumentan, además no se observa una tendencia con relación a la porosidad de las membranas, dado que en los tres tratamientos de las fibras colectadas ordenadamente la membrana que presenta la mayor porosidad (42,5%) fue obtenida a una velocidad tangencial de 1217 m/min. También es posible notar una diferencia entre los diámetros de las nanofibras colectadas ordenadamente en comparación con las colectadas aleatoriamente, siendo estas últimas las que presentaron el mayor diámetro promedio. La disminución en el diámetro es otorgada al colector rotatorio, el cual, de acuerdo a la velocidad de colección, se genera un mayor o menor estiramiento de la fibra durante el proceso de electrohilado. Sin embargo, en los resultados se observó un aumento en el diámetro de las fibras a medida que aumentaba la velocidad tangencial, por lo tanto, se puede indicar que el voltaje es el factor determinante a la hora de obtener fibras con diámetros nanométricos.

Respecto al tratamiento térmico de las nanofibras, se observa una baja variación en el diámetro de las nanofibras colectadas aleatoriamente (NA), sin embargo en las nanofibras orientadas ($NO_{1100\ m/min}$, $NO_{1217\ m/min}$, $NO_{1480\ m/min}$) se presenta una disminución en el diámetro promedio del 12,5%, 29,6% y 24,87% respectivamente (Figura 3), la cual es otorgada al auto ensamble de las cadenas moleculares de PLA dispuestas en la nanofibra, dado que el tiempo y la temperatura aplicados permiten que las cadenas se organicen mejor para formar cristales más regulares.

La Figura 3 muestra el valor medio y la variación en los diámetros de las fibras obtenidas por los distintos tratamientos descritos anteriormente.

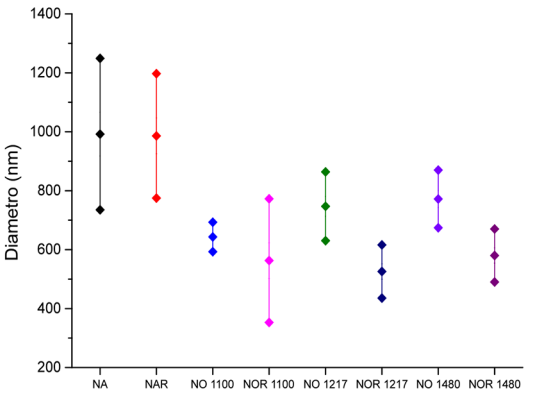


Figura 3. Efectos de la velocidad de colección y recocido en el diámetro de las fibras de PLA.

Se puede evidenciar una disminución en los máximos y mínimos de las fibras de casi todos los tratamientos. El tratamiento que está exento a esto es el tratamiento NOR 1100 dado que luego del recocido la desviación estándar de las fibras se ve incrementado, fenómeno que puede ser ocasionado por algunas fusiones de las fibras dado el tratamiento térmico. Con esto es posible indicar que el recocido es parte importante a la hora de obtener fibras con menor diámetro.

Morfología por microscopia electrónica de transmisión

En la Figura 4 se presentan las imágenes TEM obtenidas de la sección transversal de las nanofibras

colectadas a 1100 m/min y 1480 m/min. En las imágenes obtenidas es posible notar cambios y diferencias en la parte interna de las nanofibras, las cuales dadas las imágenes presentan un núcleo y una corteza.

En la Figura 4A se pueden observar nanofibras con diámetros homogéneos y de una sola tonalidad, mientras que en la Figura 3C, se observa con mayor nitidez el núcleo de las nanofibras NO 1100 m/min de una tonalidad oscura y la parte externa más clara.

A partir de lo observado es posible tener un indicio de la conformación y estructura interna de las nanofibras, en donde se asume que el núcleo presenta una fase con características amorfas mientras la corteza o parte externa de las nanofibras presentaría un estado cristalino. Además, dadas las imágenes se pueden notar dos tipos de nanofibras, las cuales son nanofibras que presentan diámetros grandes con una estructura distinguible y otras pocas con diámetros pequeños con una corteza delgada. Posiblemente esto sea un reflejo de que no todas las nanofibras tienen las mismas condiciones de electrohilado, debido a que algunas al momento de adherirse al tambor llegan más rápido que otras, lo que les impide estirarse y adelgazar [10]. Otra posible causa puede ser otorgada al movimiento de las nanofibras las cuales son afectadas por el movimiento turbulento del aire producido por la rotación del colector, generando una diferencia en el proceso de curado para cada una de ellas.

En cuanto a las nanofibras con recocido (Figura 5), se observan las nanofibras recocidas obtenidas con las tres velocidades de colección utilizadas en el electrohilado. En las imágenes se notan mayoritariamente fibras con un núcleo bastante homogéneo, lo que indica que se presentaron las condiciones de temperatura y tiempo adecuadas

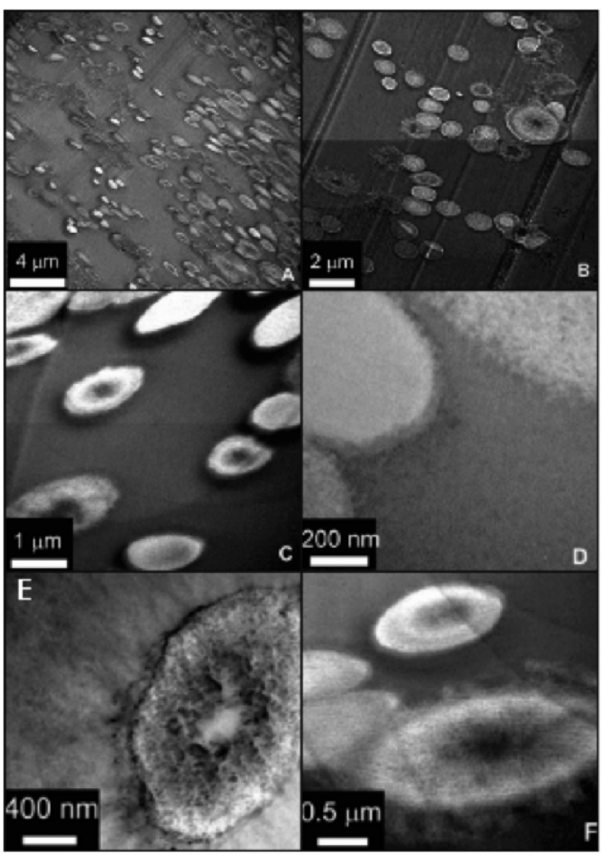


Figura 4. Microscopia electrónica de transmisión de nanofibras orientadas a 1100 m/min (A, C y E) y nanofibras orientadas a 1480m/min (B, D, y F).

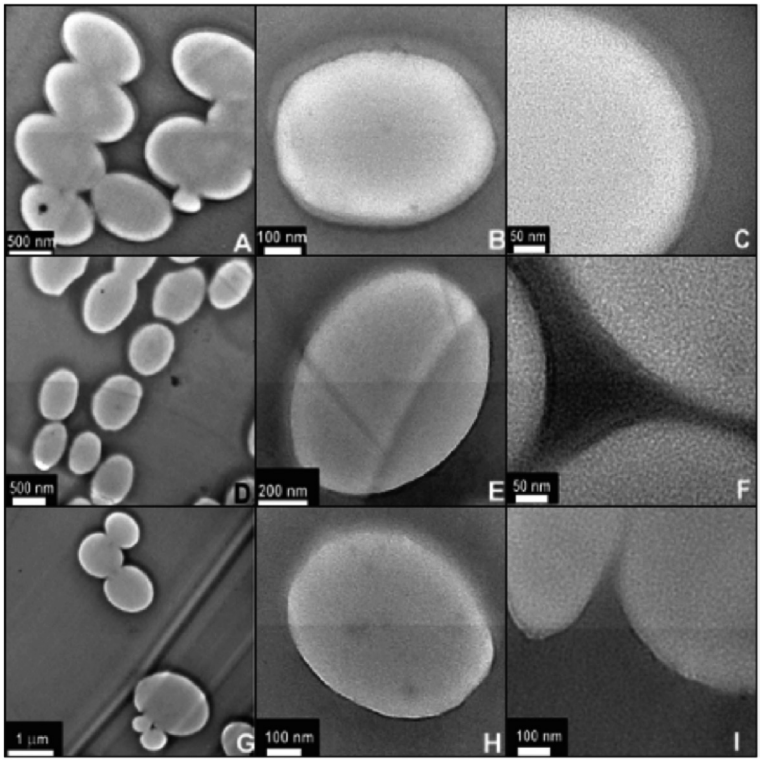


Figura 5. Observación de la estructura de las nanofibras orientadas recocidas mediante micrografías de TEM a diferentes aumentos. A), B) y C) sección transversal de NO 1100m/min. D), E) y F) sección transversal de NO 1217m/min. G), H) y I) sección transversal de NO 1480m/min.

para reorganizar las cadenas poliméricas, mejorando el grado de cristalinidad del polímero. Esto puede generar un mejoramiento en las propiedades mecánicas del material. La mencionada delgada capa de corteza, se puede observar claramente en la Figura 4 (C, F).

Estructura cristalina

En los resultados de DRX obtenidos por Gómez *et al.* [16], se presenta evidencia de un incremento en el estado amorfo de las nanofibras al ser colectadas ordenadamente, sin esta mayor a una mayor velocidad tangencial, pero luego del recocido de las nanofibras se presenta una señal definida a los 16,8º, por lo tanto es evidente que el tratamiento térmico realizado promueve una cristalización extensiva de las cadenas poliméricas. Estos resultados también presentan una gran similitud a lo observado en el difractograma de PLA grado ACS, además de ser similares a los reportados por Inai *et al*. [13].

Para obtener un análisis detallado sobre la estructura de las nanofibras, fue necesario realizar técnicas que presenten y revelen detalles a nivel nanométrico, por ello, mediante el análisis SAXS realizado a las nanofibras es posible determinar la conformación o estructura cristalina del polímero. La Figura 6 presenta los resultados obtenidos luego del análisis SAXS realizado tanto al PLA comercial como a las nanofibras colectadas aleatoria y ordenadamente (1480m/min).

Al igual que los resultados de DRX, los espectros obtenidos por SAXS de los andamios de nanofibras aleatorias (NA) y de nanofibras orientadas ($NO_{1480\ m/min}$) presentan una diferencia significativa con relación al espectro de PLA grado ACS. Al enfocar la atención en las nanofibras, se observa un corrimiento de la señal correspondiente al tamaño de cristal de las nanofibras colectadas ordenadamente.

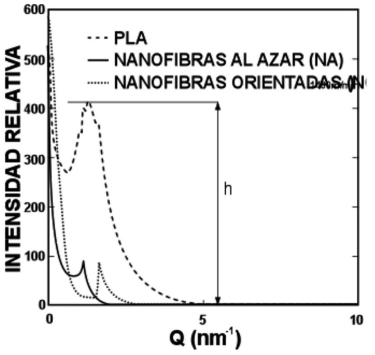


Figura 6. Espectros del PLA grado ACS, de las nanofibras colectadas aleatoriamente y de las nanofibras orientadas a una velocidad de 1480 m/min.

A partir de la curva de la Figura 7 se obtiene la distancia entre bloques cristalinos y el tamaño de los cristales del polímero en el material [17]. Se grafican las intensidades relativas en función del vector de dispersión (Q). A partir de la ecuación de dispersión (1), se calcula el valor del ángulo (θ) donde se generó la difracción, obteniendo Q de la figura y con una longitud de onda de rayos X incidente de λ = 1.5418Å.

$$Q = \frac{4\pi}{\lambda} seno\left(\frac{\theta}{2}\right) \quad (1)$$

Se calculó la distancia entre bloques a partir de la ecuación (2).

$$d = \frac{\lambda}{2seno\left(\frac{\theta}{2}\right)} \quad (2)$$

Para el cálculo del tamaño del cristal, se usa la ecuación (4).

$$B = \frac{K\lambda}{S\cos(\theta)} \quad (3)$$

$$S = \frac{K\lambda}{B\cos(\theta)} \quad (4)$$

Donde K es considerado como una constante igual a 0,94, *S* es el tamaño del cristal y B es el ancho de la línea a media altura máxima.

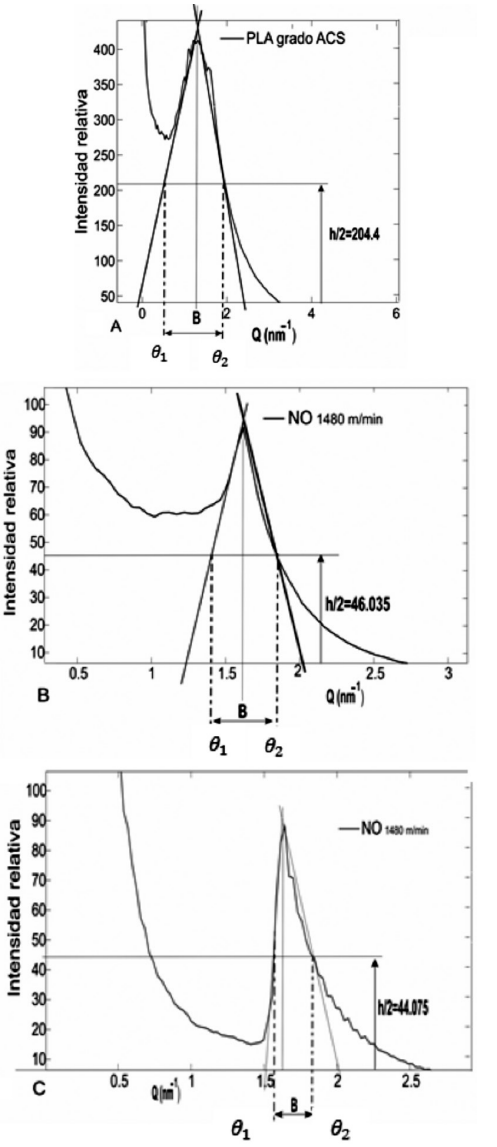


Figura 7. Geometrías para el cálculo de B y el cálculo del tamaño del cristal A.

Como en el caso actual los picos de dispersión no son simétricos, se debe proyectar líneas tangentes a las curvas y su corte con Q, determinan θ_1 y θ_2, donde $B = \theta_2 - \theta_1$ (expresado en radianes). En la Figura 10, se observan las líneas que resumen este procedimiento, aplicado a las 3 dispersiones.

En la Tabla 4 se resumen los valores para cada material probado por SAXS. Los resultados indican que el proceso de electrohilado aumenta hasta 4 veces el tamaño de los cristales, desde el PLA en

Tabla 4. Valores cristalográficos de las nanofibras obtenidas por SAXS.

Parámetro	PLA		
	Pellets	Nanofibras aleatorias	Nanofibras ordenadas a 1480m/min
Q(NM^{-1})	1,264	1,620	1,642
Angulo (Θ)	0,0310	0,0397	0,0403
Distancia entre bloques cristalinos (d)	4,971	3,879	3,827
B = (Θ_1-Θ_2) Rad	0,00124	$3,167e^{-4}$	$2,654e^{-4}$
Tamaño de cristal (s) nm	11,66	45,74	54,59

grado ASC hasta las nanofibras orientadas. Por otro lado, la nanofibra aumenta 5 veces el tamaño del cristal, cuando está orientada. Por esta razón no es detectable en DRX, siendo tan grande el tamaño de estos cristales no se pueden difractar los rayos X en las nanofibras. Por otro lado, se observa que el electrohilado disminuye la distancia entre bloques cristalinos y al orientar la nanofibra se disminuye más. La presencia de cristales grandes con menos distancia entre ellos indica una orientación de las nanofibras en su estructura interna.

Transiciones térmicas

En los análisis de DSC presentados por Gómez *et al.* [16] (Figura 8) se muestra una variación entre el tipo de colección y la velocidad de colección. Los pellets de PLA presentan un Tg a los 60 ºC, una cristalización cercana a 100 ºC y luego una última señal a 150 ºC. Este mismo patrón lo sigue las nanofibras colectadas aleatoriamente, sin embargo el último punto de fusión de las fibras con y sin recocido presenta dos señales, las cuales son otorgadas a la fusión de los componentes α y α'[18], por lo tanto se puede indicar que este método de colección genera fibras con PLA de dos diferentes estructuras. En esta temperatura se presenta inicialmente la fusión de la forma α' y su recristalización en la forma α, mientras que la segunda señal corresponde a la fusión de la forma α [19].

Allí también es posible dilucidar el grado de desorden molecular de las cadenas el cual es reflejado por la relajación entálpica, siendo esta alta en las NA en comparación con NAR y PLA grado ACS, que muestran valores de entalpia de 6,3 J/g, 5,8 J/g y 2,4 J/g, respectivamente.

Con relación a los termogramas de las nanofibras colectadas ordenadamente NO (Figura 8B) también se muestran picos de relajación entálpica alrededor de los 65ºC, con una entalpía de 5,8 J/g para $NO_{1100\ m/min}$, $NO_{1217\ m/min}$ y $NO_{1480\ m/min}$, valor que presenta similitud al observado en las nanofibras colectadas aleatoriamente. En el termograma de las nanofibras ordenadas (NO) no se observa temperatura de cristalización como el encontrado en la Figura 8A y una sola señal en su temperatura de

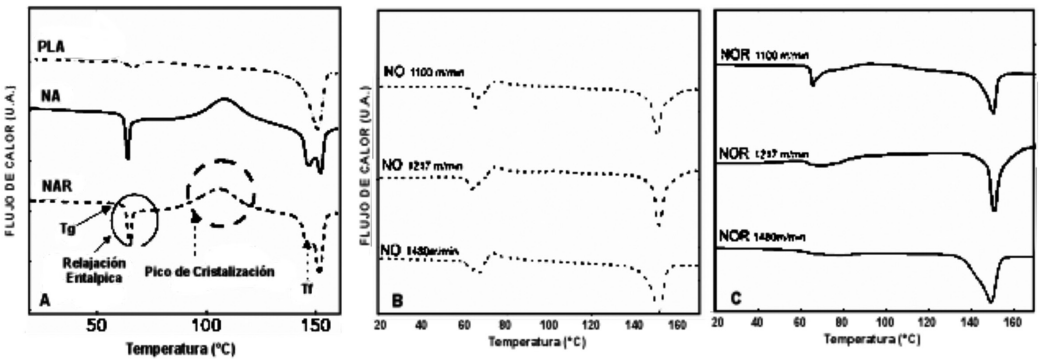


Figura 8. Calorimetría diferencial de barrido (A) PLA grado ACS y nanofibras colectadas aleatoriamente sin y con tratamiento térmico respectivamente (NA) y (NAR), (B) Nanofibras de PLA orientadas ($NO_{1100\ m/min}$, $NO_{1217\ m/min}$, $NO_{1480\ m/min}$) y (C) Nanofibras de PLA orientadas con recocido ($NOR_{1100\ m/min}$, $NOR_{1217\ m/min}$ y $NOR_{1480\ m/min}$).

fusión, por lo cual se puede indicar que este proceso de colección provoca una sola estructuración del polímero, la cual viene siendo la estructura α dada la temperatura requerida para la fusión.

Las nanofibras ordenadas y recocidas (NOR) presentan una diferencia con la Figura 8B, con relación a la temperatura de transición vítrea, dado se observa una tendencia la cual disminuye la energía de transición vítrea a medida que se incrementa la velocidad de colección, llegando hasta el punto de desaparecer la Tg, tal y como se observa con el termograma de las nanofibras recocidas colectadas a 1480m/min.

En la Tabla 5 se resumen los valores de la entalpia de cristalización, de fusión y el cálculo del porcentaje de cristalinidad tanto del PLA comercial en pellets, como en fibras obtenidas aleatorias y ordenadas.

Propiedades mecánicas de los andamios de PLA por tracción uniaxial

En las Figura 9A y 9B, se observa que las nanofibras colectadas aleatoriamente se presenta un pico bastante pronunciado después del punto de "fluencia" de la red en comparación con las nanofibras alineadas. Este punto llamado de "fluencia" refleja la rotura masiva de las nanofibras que se alinearon en la dirección de la carga para ambos tipos de andamios. Sin embargo, las nanofibras dispuestas aleatoriamente presentan una menor probabilidad de tener nanofibras alineadas en el andamio inicial y por lo tanto son muy pocas las fibras que se alinean para soportar la carga, mientras que en el caso de nanofibras orientadas (NO) existe una gran cantidad de fibras en la misma dirección generando una mayor resistencia a la rotura.

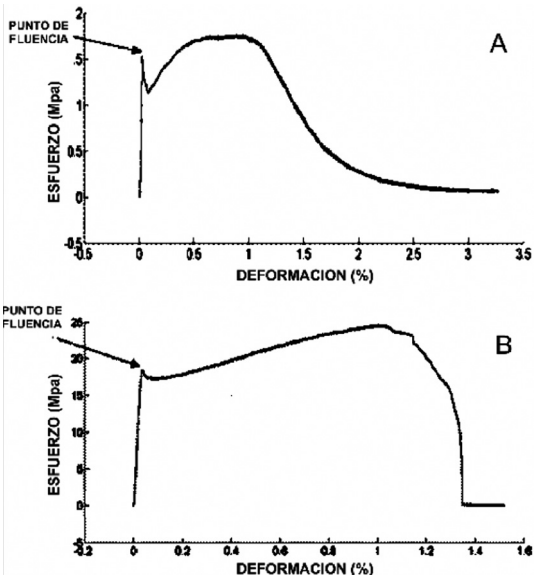


Figura 9. Comportamiento mecánico (A) nanofibras dispuestas al azar y (B) nanofibras orientadas $NO_{1100m/min}$.

En la Tabla 6, se presentan los resultados de los ensayos de tracción a los diferentes andamios. Los datos del módulo elástico presentan variabilidad debido a la estructura del andamio influenciada por distribución de poros, densidad, distribución

Tabla 5. Grado de cristalinidad de las nanofibras electrohiladas.

Tipo de PLA	ΔH_f	ΔH_c	**Cristalinidad considerando la cristalización** $= \frac{\chi_{bc}\,\Delta H_f}{\Delta H_f^0}$	**Cristalinidad después de la cristalización** $\chi_{ac} = \frac{\Delta H_f}{\Delta H_f^0}$
PLA grado ACS	28,60	N.E	30,75	30,75
NA	21,20	19,43	1,90	22,8
NAR	25,67	23,13	2,73	27,60
$NO_{1100\ m/min}$	28,63	3,947	26,54	30,78
$NOR_{1100\ m/min}$	19,39	7,69	12,58	20,9
$NO_{1217\ m/min}$	31,93	4,604	29,38	29,38
$NOR_{1217\ m/min}$	29,84	N.E	32,09	32,09
$NO_{1480\ m/min}$	29,43	4,109	27,22	31,64
$NOR_{1480\ m/min}$	29,89	N.E	32,14	32,14

de nanofibras y presencia de cúmulos con diferentes tamaños.

En la Figura 10, se realiza la comparación de los resultados de tracción. El módulo elástico y el esfuerzo a la tracción de los andamios con nanofibras orientadas (NO) fueron 7-9 veces y 10-13 veces respectivamente, mayor que los andamios con nanofibras dispuestas al azar (NA). Estas diferencias en las propiedades elásticas se explican en términos de la orientación molecular y de las nanofibras. En contraste, a los andamios con nanofibra aleatoria (NA), las nanofibras orientadas (NO) están orientadas paralelas a la dirección de carga. Por lo tanto, casi todas las nanofibras soportan y distribuyen la carga de forma simultánea durante el ensayo de tracción uniaxial.

Además, la orientación de las cadenas poliméricas sugerida por las pruebas de caracterización es mayor en las (NO) que en las (NA) debido al estiramiento de las (NO) durante el proceso de electrohilado. Como las cadenas de los polímeros se orientan a lo largo del eje principal de las nanofibras, el mejoramiento del módulo elástico en la dirección de las nanofibras es debido a la presencia de los fuertes enlaces covalentes entre los átomos de carbono en la cadena de polímero, en comparación con los enlaces intermoleculares entre las cadenas del polímero del PLA (enlaces de Van der Waals, enlaces de hidrógeno y otros). Durante el curso de los ensayos de tensión, las nanofibras de las NA en andamios fueron orientadas a lo largo de la dirección de la carga aplicada y por ello algunas nanofibras fallaron mientras otras soportaron la carga aplicada hasta que se produce la fractura final. Como resultado, los andamios con NA presentan los más pequeños esfuerzos de limite elástico σ_{ys} y resistencia a la tensión σ_{us} (esfuerzo último), en comparación con los andamios de nanofibras orientadas (NO).

El módulo elástico de Young de las (NO) colectado a 1480 m/min, es más alto que las colectadas a 1217m/min y que las colectadas a 1100 m/min, esto indica que a mayor rotación se genera una disminución del tamaño de cristal lo que influirá en el aumento del módulo de Young. En la Figura 11 se observa que las nanofibras con recocido $NOR_{1217m/min}$ no presentaron un efecto en las propiedades elásticas de las nanofibras orientadas ($NO_{1217m/min}$), ya que la alta desviación estándar en los resultados de ambos tipos de nanofibras muestra que son estadísticamente iguales (881.3+/-100.2 y 854.2+/-60.7 para $NO_{1217\ m/min}$ y $NO_{1217m/min}$). Este hecho sugiere que el cambio en la cristalización no afecta las propiedades elásticas de las nanofibras orientadas.

Esto se puede explicar porque el recocido genera una homogenización de los cristales hacia todas direcciones, por lo que no generaría un mejoramiento preferencial de la orientación de los cristales respecto de las nanofibras orientadas sin recocidas en la dirección de la aplicación

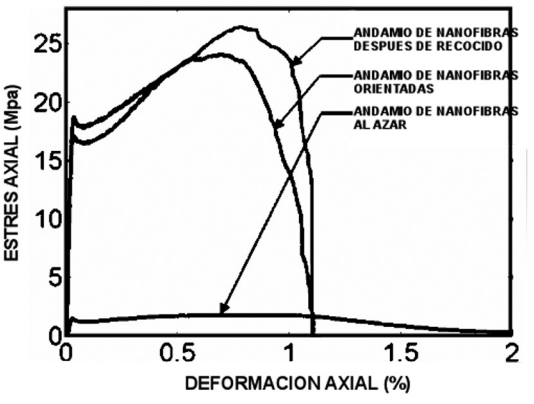


Figura 10. Ensayos de tracción de andamios con (NA) y andamios con ($NO_{1100\ m/min}$).

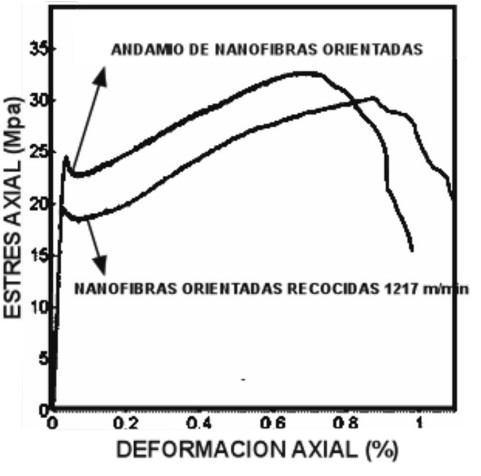


Figura 11. Comparación de resultados de los ensayos de tracción de andamios con $NO_{1217\ m/min.}$

Tabla 6. Resultados de los ensayos de tracción en los diferentes tipos de nanofibras.

Tipo de Andamio	Módulo de Young E (MPa)	Esfuerzo de fluencia σ_{ys} (MPa)	Deformación a la fluencia %	Resistencia a la tensión σ_{us} (MPa)	Deformación ultima max %
NA	96,8+/-32,5	1,7+/-0,2	4,2+/-2,4	2,8+/-0,6	129,6+/-32,5
$NO_{1100m/min}$	683,6+/-33,2	18,4+/-0,6	3,4+/-0,3	24,0+/-0,7	86,4+/-15,2
$NOR_{1100m/min}$	620,8+/- 74,2	13,8+/-4,8	3,6+/-0,4	20,3+/-8,8	95,5+/-10,0
$NO_{1217\ m/min}$	881,3+/-100,2	25,0+/-2,2	3,7+/-0,4	32,2/-2,9	75,0+/-7
$NOR_{1217m/min}$	854,2+/-60,7	19,4+/-1,1	3,5+/-0,7	31,0+/-3,0	93,0+/-4,9
$NO_{1480\ m/min}$	1026,73+/-320	29,23+/-2,2	4,73+/-1,7	30,29+/-2,5	75,2+/-1,9
$NOR_{1480\ m/min}$	1177,4+/-106	31,68+/-4,25	3,549+/-0,69	44,43+/-12,5	80,17+/-39,5

de la carga. Estos resultados contrastan con los obtenidos por C.T Lim *et al.* [20], donde indicaron un mejoramiento de las propiedades elásticas de nanofibras orientadas al azar de Policaprolactona por efecto del tratamiento térmico, pero en ese estudio no se compara con nanofibras orientadas, y como se ha indicado en el presente estudio la orientación de nanofibras genera una orientación molecular que afectarán el módulo de Young.

CONCLUSIONES

Mediante la aplicación de diferentes técnicas de caracterización se logró determinar las propiedades morfológicas y estructurales de las nanofibras con lo cual fue posible obtener una descripción completa y detallada de la estructura de las nanofibras de PLA y su relación con variables tales como la orientación de nanofibras en los andamios, velocidad de rotación del colector y tratamientos térmicos posteriores al electrohilado. Mediante esta experimentación se evidencio la relación y los cambios que genera el tipo de colector, siendo mejor el colector rotatorio debido a que disminuye los defectos en las fibras. En cuanto al recocido se presenta una mejora en la cristalinidad, sin embargo, no existe cambio considerable en las propiedades elásticas como en la respuesta a la resistencia a tensión. Este trabajo permitió observar las propiedades elásticas de nanofibras, a partir de las variables mencionadas, lo que se puede usar a futuro en el diseño de los andamios celulares de nanofibras de PLA. Además, las condiciones en que se realizó el electrohilado son aceptables y muy cercanos a los ideales.

AGRADECIMIENTOS

Se agradece el apoyo del Instituto de Investigaciones en Materiales, UNAM, así como de sus técnicos académicos por el apoyo en la realización de los análisis: Adriana Tejeda (DRX), Eriseth Fregoso (DSC), Omar Novelo and Esau González (SEM), Carlos Flores (TEM). Yiguel Ángel Canseco (ATR-FTIR). Se agradece también a DGAPA, UNAM por el apoyo económico a este trabajo a través del proyecto PAPIIT IN 108116.

REFERENCIAS

[1] C.P. Barnes, S.A. Sell, E.D. Boland, D.G. Simpson, and G.L. Bowlin. “Nanofiber technology: Designing the next generation of tissue engineering scaffolds”. Advanced Drug Delivery Reviews. Vol. 59, pp. 1413-1433. 2007.

[2] G. Chen, T. Ushida, and T. Tateishi. “Scaffold Design for Tissue Engineering”. Macromolecular Bioscience. Vol. 2, pp. 67-77. 2002.

[3] B.D. Ulery, L.S. Nair, and C.T. Laurencin. “Biomedical applications of biodegradable polymers”. Journal of Polymer Science Part B: Polymer Physics. Vol. 49, pp. 832-864. 2011.

[4] N. Ninan, M. Muthiah, I.-K. Park, A. Elain, T. W. Wong, S. Thomas, et al. “Faujasites incorporated tissue engineering scaffolds for wound healing: in vitro and in vivo analysis”. ACS applied materials & interfaces. Vol. 5, pp. 11194-11206. 2013.

[5] L. Kong, Y. Gao, G. Lu, Y. Gong, N. Zhao, and X. Zhang. “A study on the bioactivity

of chitosan/nano-hydroxyapatite composite scaffolds for bone tissue engineering". European Polymer Journal. Vol. 42, pp. 3171-3179. 2006.

[6] F.P. La Mantia, R. Arrigo, and M. Morreale. "Effect of the orientation and rheological behaviour of biodegradable polymer nanocomposites". European Polymer Journal. Vol. 54, pp. 11-17. 2014.

[7] K. Ghosal, M.S. Latha, and S. Thomas. "Poly(ester amides) (PEAs) – Scaffold for tissue engineering applications". European Polymer Journal. Vol. 60, pp. 58-68. 2014.

[8] R. Vasita and D.S. Katti. "Nanofibers and their applications in tissue engineering". International Journal of Nanomedicine. Vol. 1, pp. 15-30. 2006.

[9] C.T. Laurencin, S.G. Kumbar, S.P. Nukavarapu, R. James, and M.V. Hogan. "Recent patents on electrospun biomedical nanostructures: an overview". Recent patents on biomedical engineering. Vol. 1, pp. 68-78. 2008.

[10] L.M. D. Sánchez, L. Rodriguez, and M. López. "Electrospinning: la era de las nanofibras". Revista Iberoamericana de Polímeros. Vol. 14, pp. 10-27. 2013.

[11] T. Stylianopoulos, C.A. Bashur, A.S. Goldstein, S.A. Guelcher, and V.H. Barocas. "Computational predictions of the tensile properties of electrospun fibre meshes: effect of fibre diameter and fibre orientation". Journal of the mechanical behavior of biomedical materials. Vol. 1, pp. 326-335. 2008.

[12] R. Vera-Graziano, A. Maciel-Cerda, E. Moreno-Rondon, A. Ospina, and E. Gomez-Pachon. "Modified polylactide microfiber scaffolds for tissue engineering". In MRS Proceedings. 2012, pp. imrc11-1376-s11-09.

[13] R. Inai, M. Kotaki, and S. Ramakrishna. "Structure and properties of electrospun PLLA single nanofibres". Nanotechnology. Vol. 16, p. 208. 2005.

[14] E.P.S. Tan, S.Y.Ng, and C.T. Lim. "Tensile testing of a single ultrafine polymeric fiber". Biomaterials. Vol. 26, pp. 1453-1456. 2005.

[15] Y. You, S. Won Lee, S. Jin Lee, and W. H. Park. "Thermal interfiber bonding of electrospun poly(l-lactic acid) nanofibers". Materials Letters. Vol. 60, pp. 1331-1333. 2006/05/01/ 2006.

[16] E.Y. Gómez-Pachón, F.M. Sánchez-Arévalo, F.J. Sabina, A. Maciel-Cerda, R.M. Campos, N. Batina, et al. "Characterisation and modelling of the elastic properties of poly(lactic acid) nanofibre scaffolds". Journal of Materials Science. Vol. 48, pp. 8308-8319. 2013.

[17] R. Parmar, M. Mangrola, B. Parmar, and V. Joshi. "A software to calculate crystalline size by Debey-Scherrer Formula using VB.NET". Multi Disciplinary Edu Global Quest. Vol. 1, 2012.

[18] P. Pan, B. Zhu, W. Kai, T. Dong, and Y. Inoue. "Polymorphic Transition in Disordered Poly(l-lactide) Crystals Induced by Annealing at Elevated Temperatures". Macromolecules. Vol. 41, pp. 4296-4304. 2008/06/01 2008.

[19] P. Pan, W. Kai, B. Zhu, T. Dong, and Y. Inoue. "Polymorphous Crystallization and Multiple Melting Behavior of Poly(l-lactide): Molecular Weight Dependence". Macromolecules. Vol. 40, pp. 6898-6905. 2007/09/01 2007.

[20] C. Lim, E. Tan, and S. Ng. "Effects of crystalline morphology on the tensile properties of electrospun polymer nanofibers". Applied Physics Letters. Vol. 92, p. 141908. 2008.

pharmaceutics

MDPI

Article

Electrospun Scaffolds of Polylactic Acid, Collagen, and Amorphous Calcium Phosphate for Bone Repair

William Cárdenas-Aguazaco [1], Bernardo Camacho [1], Edwin Yesid Gómez-Pachón [2], Adriana Lorena Lara-Bertrand [1] and Ingrid Silva-Cote [1,*]

[1] Instituto Distrital de Ciencia, Biotecnología e Innovación en Salud-IDCBIS, Bogotá 111611, Colombia; wcardenas@idcbis.org.co (W.C.-A.); bacamacho@idcbis.org.co (B.C.); alara@idcbis.org.co (A.L.L.-B.)
[2] Facultad Duitama, Universidad Pedagógica y Tecnológica de Colombia-UPTC, Duitama 150462, Colombia; edwin.gomez02@uptc.edu.co
* Correspondence: izsilva@idcbis.org.co

Abstract: Most electrospun scaffolds for bone tissue engineering typically use hydroxyapatite (HA) or beta tricalcium phosphate (β-TCP). However, the biological activity of these crystalline compounds can be limited due to their low solubility. Therefore, amorphous calcium phosphate (ACP) may be an alternative in bone repair scaffolds. This study analyzes the morphology, porosity, mechanical strength, and surface chemistry of electrospun scaffolds composed of polylactic acid and collagen integrated with hydroxyapatite (MHAP) or amorphous calcium phosphate (MACP). In addition, the in vitro biocompatibility, osteogenic differentiation, and growth factor production associated with bone repair using human Wharton's jelly-derived mesenchymal stem cells (hWJ-MSCs) are evaluated. The results show that the electrospun MHAP and MACP scaffolds exhibit a fibrous morphology with interconnected pores. Both scaffolds exhibit favorable biocompatibility and stimulate the proliferation and osteogenesis of hWJ-MSCs. However, cell adhesion and osteocalcin production are greater in the MACP scaffold compared to the MHAP scaffold. In addition, the MACP scaffold shows significant production of bone-repair-related growth factors such as transforming growth factor-beta 1 (TGF-β1), providing a solid basis for its use in bone tissue engineering.

Keywords: electrospinning; bone repair; PLA; calcium phosphate; hydroxyapatite

check for updates

Citation: Cárdenas-Aguazaco, W.; Camacho, B.; Gómez-Pachón, E.Y.; Lara-Bertrand, A.L.; Silva-Cote, I. Electrospun Scaffolds of Polylactic Acid, Collagen, and Amorphous Calcium Phosphate for Bone Repair. *Pharmaceutics* **2023**, *15*, 2529. https://doi.org/10.3390/pharmaceutics15112529

Academic Editor: Frederico B. De Sousa

Received: 31 August 2023
Revised: 14 October 2023
Accepted: 16 October 2023
Published: 25 October 2023

Copyright: © 2023 by the authors. Licensee MDPI, Basel, Switzerland. This article is an open access article distributed under the terms and conditions of the Creative Commons Attribution (CC BY) license (https://creativecommons.org/licenses/by/4.0/).

1. Introduction

Bone repair is a major challenge in tissue engineering due to the high incidence of fractures and bone defects caused by trauma, disease, and non-union fractures [1,2]. Researchers have developed methods in tissue engineering that use biomaterials, cells, and bioactive substances to address these challenges [3]. Biomaterials such as natural or synthetic polymers, inorganic composites, and hybrid blends are critical for the fabrication of bone scaffolds that provide mechanical stability, biocompatibility, biodegradability, osteoconductivity, and osteoinductivity [4,5].

Polylactic acid (PLA) is a biodegradable and biocompatible synthetic polymer widely used in biomedical applications for bone tissue due to its ease of processing, mechanical stability, and versatility [6]. PLA has some notable drawbacks, such as low hydrophilicity, slow degradation, and limited bioactivity [7]. To overcome these limitations, PLA can be combined with other biomaterials, including collagen (COL) and calcium phosphates (CaPs). COL, a natural protein found in the extracellular matrix of bone, has high biocompatibility, bioactivity, and hydrophilicity [8]. Meanwhile, bioceramics known as CaPs have become a common choice for bone repair systems. Their excellent biocompatibility, osteoconductivity, and similarity to the natural bone mineral phase have made them a widely adopted solution [9]. CaPs can be classified based on their chemical composition, crystal structure, and solubility; they include HAP, β-TCP, octacalcium phosphate (OCP), and ACP [10]. Each type of CaP has advantages and disadvantages for bone regeneration

applications depending on specific properties such as mechanical strength, degradation rate, and bioactivity [11]. HAP is the CaP that is more frequently used in bone tissue engineering because it is the primary inorganic component of bone mineral. This bioceramic possesses remarkable osteoinductive and osteoconductive properties [12]. Furthermore, research has demonstrated that combining it with PLA and COL to fabricate scaffolds is a feasible option for bone tissue engineering [13].

On the other hand, there are several techniques to create scaffolds by combining these three materials. One such technique is electrospinning, a versatile and reproducible method that uses an electric field on a polymer solution to produce micro or nanofibers [14]. Electrospun scaffolds have high porosity and a large specific surface area, and they incorporate the properties of each material, facilitating cellular interaction and the infiltration of nutrients and growth factors [15]. In addition, electrospinning allows for control over the fiber diameter, orientation, composition, and incorporation of bioactive agents [16].

Several studies have reported on the fabrication and characterization of electrospun PLA, COL, and HAP scaffolds for bone applications. These studies showed promising results regarding morphology, composition, mechanical properties, and biological performance [17,18]. However, HAP's high crystallinity and stoichiometry can result in a relatively slow dissolution rate, which could negatively affect bone repair processes [19]. An alternative to HAP is ACP; due to its disordered structure and structural defects, ACP is a precursor phase of HAP that exhibits higher reactivity, solubility, and bioactivity [20]. ACP can release calcium and phosphate ions in a physiological context. This phenomenon promotes the growth of HAP crystals on the scaffold's surface and enhances the bone cell differentiation process towards osteogenesis [21].

Although few studies have investigated the integration of ACP into electrospun scaffolds for bone applications [22,23], these scaffolds have shown that they are promising for bone tissue engineering and have the potential to promote bone regeneration due to their rapid mineralization and improved cell adhesion [24–26]. The quantity and evenness of ACP dispersion in the electrospun fibers have an impact on the morphology, stability, and functional traits of the resulting scaffolds. The overabundance or deficiency of ACP could potentially compromise both the mechanical and bioactive properties of these scaffolds. In addition, the physicochemical properties of electrospun scaffolds incorporating ACP in conjunction with proteins such as collagen have not been studied, nor have their effects on primary cells been evaluated.

The hWJ-MSCs are primary cells with a high proliferative capacity, low immunogenicity, and ability to differentiate into osteoblasts, chondrocytes, and adipocytes. Previous studies have shown the potential of hWJ-MSCs for tissue regeneration, particularly in cartilage and bone. These cells possess immunoprivileged or hypo-immunogenic properties [27,28], which make them a viable option for allogeneic therapies. Additionally, hWJ-MSCs generate paracrine factors and immunomodulators that aid in the recruitment of other cells for tissue repair [29].

To better comprehend the effects of ACP on the physicochemical characteristics of electrospun scaffolds made of PLA and COL, and their implications for bone regeneration, we created and analyzed the physicochemical properties, as well as evaluated the biological properties of electrospun scaffolds incorporating PLA and COL alongside HAP or ACP, labeled MHAP and MACP. The aim is to investigate the impact of bioceramics on scaffold properties and their subsequent influence on the behavior of hWJ-MSCs in regenerative medicine studies.

2. Materials and Methods

2.1. Materials

Calcium hydroxide ($Ca(OH)_2$, 95% purity), orthophosphoric acid (H_3PO_4, 85% purity), ammonium hydroxide solution (NH_4OH, 28–30%), HAP (<200 nm particle size), and COL (from calf skin type I) were acquired from Sigma-Aldrich (St Louis, Missouri, USA). PLA

(Mw 90 kDa) was acquired from 3DBOTS, and the solvent, 2, 2, 2 trifluoroethanol (TFE, 99% purity), was acquired from Merck Millipore (Darmstamdt, Hesse, Germany).

2.2. Synthesis of Amorphous Calcium Phosphate

A wet chemical precipitation reaction was used to obtain ACP [30]. A total of 79.55 g of $Ca(OH)_2$ was dissolved in 500 mL of distilled water at room temperature. Then, 97.35 g of H_3PO_4 was added at 1.5 mL/min. This solution remained at room temperature for 24 h while stirring continuously. Then, 10 g of NH_4OH was added drop by drop until the solution was brought to a pH level of 10, in order to generate the precipitation of the solid. This precipitate was filtered under a vacuum and dried at 100 °C for one hour.

2.3. HAP and ACP Characterization

The morphology, size, and calcium/phosphorus ratio of HAP and the synthesized ACP were examined using scanning electron microscopy (SEM) and X-ray dispersive spectroscopy (EDX). To accomplish this, a microscope (JSM-6510, JEOL, Tokyo, Japan) equipped with an EDX detector (INCA Energy, Oxford Instruments, Abingdon, UK) was utilized. Images were captured at various magnifications, and the average diameter of the compounds was determined using ImageJ software (https://imagej.net/software/fiji/downloads (accessed on 27 July 2023)). EDX spectra were also obtained in the 0–10 keV range, with a resolution of 10 eV and an acquisition time of 60 s. The INCA software (https://www.etas.com/en/products/inca_software_products.php (accessed on 24 July 2023)) was employed to calculate the atomic and weight percentages of the detected elements.

XRD data were collected using a high-resolution X-ray diffractometer PANalytical from the X'PERT PRO line (Malvern Panalytical, Malvern, UK) equipped with a copper (Cu) X-ray source (λ = 1.5406 Å) operating at 40 kV and 30 mA. Data were collected using a scintillation detector with a 2-s counting time per step, over a 2θ range of 20° to 50° and a step size of 0.02°. The diffraction patterns obtained from the sample underwent processing to yield 2θ vs. intensity plots.

2.4. Electrospun Scaffold Fabrication

MHAP and MACP solutions were mixed at a weight ratio of 10:1:1 (PLA:COL:CaP) according to the ratios proposed by Akkouch et al. [31], with some modifications (see Table 1). Additionally, a control scaffold of neat PLA was used. The materials were homogenized in TFE at 500 rpm and 30 °C for a duration of 3 h. Electrospinning was then conducted at 20 °C using a square horizontal static collector measuring 5 cm × 5 cm, following the parameters outlined by Gomez-Pachón et al. [32], with some modifications (15 kV, 15 cm, and 2 mL/h). The resulting scaffolds were placed in a desiccator until they were ready to be used for physicochemical characterization or cellular assays.

Table 1. Specifications of solutions prepared for electrospinning.

Nomenclature	Calcium Phosphate	PLA (mg/mL)	COL (mg/mL)	CaP (mg/mL)
MHAP	Hydroxyapatite	100	10	10
MACP	Amorphous	100	10	10
PLA	N/A	100	-	-

2.5. Scaffold Characterization

A Fourier transform infrared spectroscopy (FTIR) analysis was conducted to identify the functional groups present in the scaffolds. For this purpose, a spectrophotometer (Nicolet 510P, Thermo Scientific, Waltham, MA, USA) equipped with an attenuated total reflectance (ATR) accessory was utilized. Spectra were recorded in the range of 4000–500 cm^{-1}, with a resolution of 4 cm^{-1} and 32 scans.

The elemental composition of the scaffolds was determined through X-ray photoelectron spectroscopy (XPS). Measurements were performed using a spectrometer (VERSAPROB II, Physical Electronics GmbH, Feldkirchen, Bavaria, Germany) with a 200 W Mg X-ray source (h = 1253.6 eV) and a 50 eV hemispherical analyzer. Spectra were recorded in the range of 0–1100 eV, with a resolution of 0.1 eV and a step of 0.05 eV. To correct the charge shift, the C1s peak at 284.8 eV was used as an internal reference.

The diameters, porosity, and morphology of the electrospun fibers were observed using SEM (JEOL-JSM-7600F, Tokyo, Japan). Prior to analysis, the scaffolds were coated with gold using a sputter coater. From the obtained images, the average diameter of the fibers was determined using ImageJ software (https://imagej.net/software/fiji/downloads (accessed on 2 February 2023)).

The glass transition temperature (Tg), crystallization temperature (Tc), and melting temperature (Tm) of the electrospun scaffolds were determined through a calorimetric analysis (DSC). A calorimeter (DSC Q100, TA Instrument, New Castle, DE, USA) with nitrogen as the purge gas was employed. Approximately 5 mg of each sample was weighed and subjected to a heating ramp from 20 °C to 250 °C, with a heating rate of 10 °C/min.

Finally, the tensile test was performed following ASTM D1708 standards using an INSTRON 1125 (INSTRON, Norwood, MA, USA) universal uniaxial tensile testing machine. The test was conducted at a speed of 10 mm/min with a load of 5 kN. Five specimens were tested to calculate the Young's modulus of the scaffolds. All procedures described above were carried out at room temperature.

2.6. Cytotoxicity Assay

The in vitro cytotoxicity test was performed as a direct contact assay in accordance with ISO 10993-5 [33]. The hWJ-MSCs were seeded at a density of 3×10^4 cells/well in 24-well plates and cultured in Dulbecco's Modified Eagle Medium (DMEM) supplemented with human platelet lysate (hPL, 10% *v*/*v*), 100 IU/mL penicillin, 2.5 µg/mL streptomycin, and 80 µL heparin and incubated at 37 °C in a humidified atmosphere containing 5% CO_2 for 24 h. After 24 h of cell culture, the scaffolds were carefully placed on the cell monolayer in the center of each of the replicate wells and incubated for 24 and 48 h [34]. The culture medium was then removed, and resazurin was introduced to determine the cytotoxic effects. The redox dye resazurin (0.01 mg/mL, Sigma-Aldrich, St. Louis, MO, USA) was added to each well at a concentration of 1% (*v*/*v*). The wells were then incubated for three hours at 37 °C in an atmosphere that contained 5% CO_2 and was protected from light. After incubation, the supernatant was collected and transferred to a 96-well plate. The Synergy MX spectrophotometer microplate reader (Biotek Synergy, Winooski, VT, USA) was used to measure the reduction of resazurin (non-fluorescent blue dye) to resorufin (pink fluorescent) at an excitation wavelength of 570 nm and an emission wavelength of 600 nm [35]. Three cell donors were used, and three replicates were performed for each condition.

2.7. Cell Adhesion and Proliferation

To assess the effects of the electrospun scaffolds on cell adhesion and proliferation, we utilized hWJ-MSCs that were transduced with green fluorescent protein (hWJ-MSCs-GFP). The scaffolds were cut into circular discs 1 cm in diameter and plated in 48-well plates. Subsequently, the scaffold discs were sterilized using the BIOBEAM 2000 caesium-137 gamma irradiation device (Eckert & Ziegler BEBIG GmbH, Berlin, Germany). Two doses of 25 Gray each were administered at room temperature for 15 min under light-protected conditions. After sterilization, a cell density of 5×10^4 cells was seeded in Dulbecco's Modified Eagle Medium (DMEM) supplemented with human platelet lysate (hPL, 10% *v*/*v*), 100 IU/mL penicillin, 2.5 µg/mL streptomycin, and 80 µL heparin. The cells were incubated at 37 °C in a humidified atmosphere containing 5% CO_2 for 24 h to facilitate cell adhesion. Following this, 400 microliters of the supplemented DMEM medium were added to the cells and changed every 2 to 3 days. The cells' adhesion, morphology, and

proliferation were observed using a Leica fluorescence microscope (DMi8-M). Images were captured with a Leica camera (Leica Microsystems GmbH, Wetzlar, Hesse, Germany) on days 1, 3, and 5.

In addition, cell organization on the scaffolds was evaluated after 7 days of culture with hWJ-MSCs by staining with phalloidin red (1:100 in PBS, Biolegend, San Diego, CA, USA) and 4′,6-diamidino-2-phenylindole dihydrochloride (DAPI, 0.1 ug mL^{-1} in deionized water, Thermo-Fisher Scientific), which allows precise visualization of the distribution of F-actin in the cell cytoskeleton and the location of nuclei, respectively. Images were captured using a confocal laser scanning microscope (Olympus FV1000, Tokyo, Japan) and analyzed with Fiji software (https://imagej.net/software/fiji/downloads (accessed on 11 August 2023)).

The proliferation of hWJ-MSCs on the PLA, MHAP, MACP, and TCP scaffolds was evaluated on days 1, 3, and 5 using the resazurin assay (Sigma-Aldrich). For each time point, 500 µL of a 1% resazurin solution in a fresh culture medium was added and incubated for 3 h after replacing the supplemented culture medium. After completion, 100 µL of supernatant from each treatment was collected, and the absorbance was recorded in a microplate reader (Synergy; BioTek, Winooski, VT, USA) at 570 nm and 600 nm [35]. A positive control group of cells seeded in tissue culture plate (TCP) was included.

2.8. Secretion of Growth Factors

The quantification of the platelet-derived growth factor (PDGFbb), basic fibroblast growth factor (bFGF), angiopoietin I, vascular endothelial growth factor (VEGF), and transforming growth factor-β1 (TGF-β1) secretion was performed using a magnetic bead-bound immunoassay (Luminex LXSAHM-08 from R&D Systems, Minneapolis, MN, USA) according to the manufacturer's instructions. The Luminex plate was read on the Luminex® Bio-Plex® 200 system. In total, 5×10^4 hWJ-MSCs from three donors were cultured on 1 cm diameter electrospun scaffolds (PLA, MHAP and MACP) under standard conditions. Supernatants were collected at 12, 24, 48, 72, and 96 h, centrifuged at 1200 rpm for 6 min to remove cellular debris, and stored at −20 °C. In addition, the protein concentration in the supplemented culture medium (0 h) and the supernatant of hWJ-MSCs seeded on tissue culture plates (TCP) were used as controls.

2.9. Osteogenic Differentiation

To induce osteogenic differentiation, hWJ-MSCs were seeded on the PLA, MHAP, and MACP scaffolds as previously described and treated with an osteogenic differentiation medium (StemPro Osteogenesis Differentiation Kit, Life Technologies, Carlsbad, CA, USA) 48 h after seeding. The medium was changed every 3 days until day 7. Calcium deposition was confirmed by staining sections of the samples with alizarin red (Sigma-Aldrich). Cells seeded on TCP were used as a control.

2.10. Immunohistochemical Analysis

Immunohistochemistry was performed on MHAP/hWJ-MSC and MACP/hWJ-MSC samples cultured in the supplemented DMEM and osteogenic differentiation medium to detect osteocalcin (OCN). Mouse monoclonal anti-OCN was used at 10 µg/mL (MAB1419, R&D Systems, Minneapolis, MN, USA). The procedure was performed according to the manufacturer's instructions using the Vectastain Elite ABC Kit (Vector Laboratories, Burlingame, CA, USA). Briefly, deparaffinized and hydrated tissue sections were treated with urea tris buffer (pH 9.5) at 95 °C for 15 min to recover epitopes. Endogenous peroxidase activity was then blocked by treatment with 0.3% hydrogen peroxide in methyl alcohol for 10 min. The samples were incubated with the appropriate blocking serum (10% [*v*/*v*] goat, rabbit, or horse serum in phosphate-buffered saline (PBS), Vector Laboratories Vectastain Elite ABC Kit (Burlingame, CA, USA), followed by incubation with the primary antibody at 4 °C overnight. After three washes with PBS, sections were incubated with the appropriate biotinylated secondary antibody, followed by ABC peroxidase. The peroxidase

reaction was developed using a substrate kit containing 3-3′-diaminobenzidine (Vector Laboratories, Newark, NJ, USA), and the reaction was terminated with distilled water.

2.11. SEM Imaging of Cells

After 7 days of culture in the supplemented DMEM and osteogenic differentiation medium, cells on the PLA, MHAP, and MACP scaffolds were fixed with 4% PFA (Sigma-Aldrich) for 1 h at 25 °C. The samples were rinsed three times with PBS and dehydrated in a series of alcohol solutions with increasing ethanol concentrations (50%, 70%, 90%, 96%, and 100%). They were then incubated in hexamethyldisilazane (HDMS, Sigma-Aldrich). After the complete evaporation of HDMS, the samples were coated with a gold layer and imaged by SEM.

2.12. Statistical Analysis

Statistical data analyses were conducted using ANOVA and Tukey's post hoc test for multiple comparisons with GraphPad Prism version 8 software. In all instances, statistical significance was set at $p < 0.05$. All experiments were repeated three times.

3. Results

3.1. HAP and ACP Characterization

Figure 1a,b display SEM images of HAP and ACP, respectively. HAP presents a homogeneous particle size of 0.372 ± 0.196 µm and a regular, smooth surface. Conversely, amorphous calcium phosphate exhibits erratic aggregates measuring 3.212 ± 1.807 µm, together with a rougher and more porous texture. The discrepancy results from the structural differences between hydroxyapatite and amorphous calcium phosphate. Hydroxyapatite features a compact and orderly structure, whereas amorphous calcium phosphate has a less dense and disordered structure [36].

The EDX analysis evaluated the elemental composition of HAP and ACP, as shown in Figure 1c,d, respectively. The EDX spectra show the presence of calcium (Ca) and phosphorus (P) signals in both materials, confirming their identical elemental composition. Specifically, HAP shows atomic percentages of 3.37% for P and 5.50% for Ca, while ACP shows higher atomic percentages of 6.74% for P and 8.23% for Ca. However, the differences in the Ca/P ratio between the two compounds (1.63 for HAP and 1.22 for ACP) suggest variations in their degree of crystallinity. Based on the data presented by Munir et al. [37], it is clear that HAP is equivalent to calcium hydroxyapatite, while ACP is classified as amorphous calcium phosphate.

The XRD spectra, shown in Figure 1e, revealed distinct patterns for each material. In the HAP sample, three high-intensity peaks were observed at a 2θ angle of 31.72, 32.18, and 32.91, corresponding to the crystallographic planes (211), (112), and (300), respectively. The noticeable peaks and regions indicate the ordered crystalline structure of the material. These findings align with the HAP crystal structure [38]. On the other hand, ACP exhibits three peaks at 27.79, 31.03, and 34.39, which correspond to the crystallographic planes (214), (210), and (220), respectively. These peaks match with the primary peaks of an apatitic structure relating to β-tricalcium phosphate (β-TCP) [39].

The results support the extensively documented crystal structure of HAP, as evidenced by the characteristic peaks visible in its XRD patterns. In contrast, the XRD spectrum of ACP only showed a few low-intensity diffraction peaks, suggesting the presence of a minimal amount of crystalline material, which adopts a tricalcium beta-phosphate conformation. The significant absence of identifiable diffraction signals suggests that ACP is mostly composed of amorphous material.

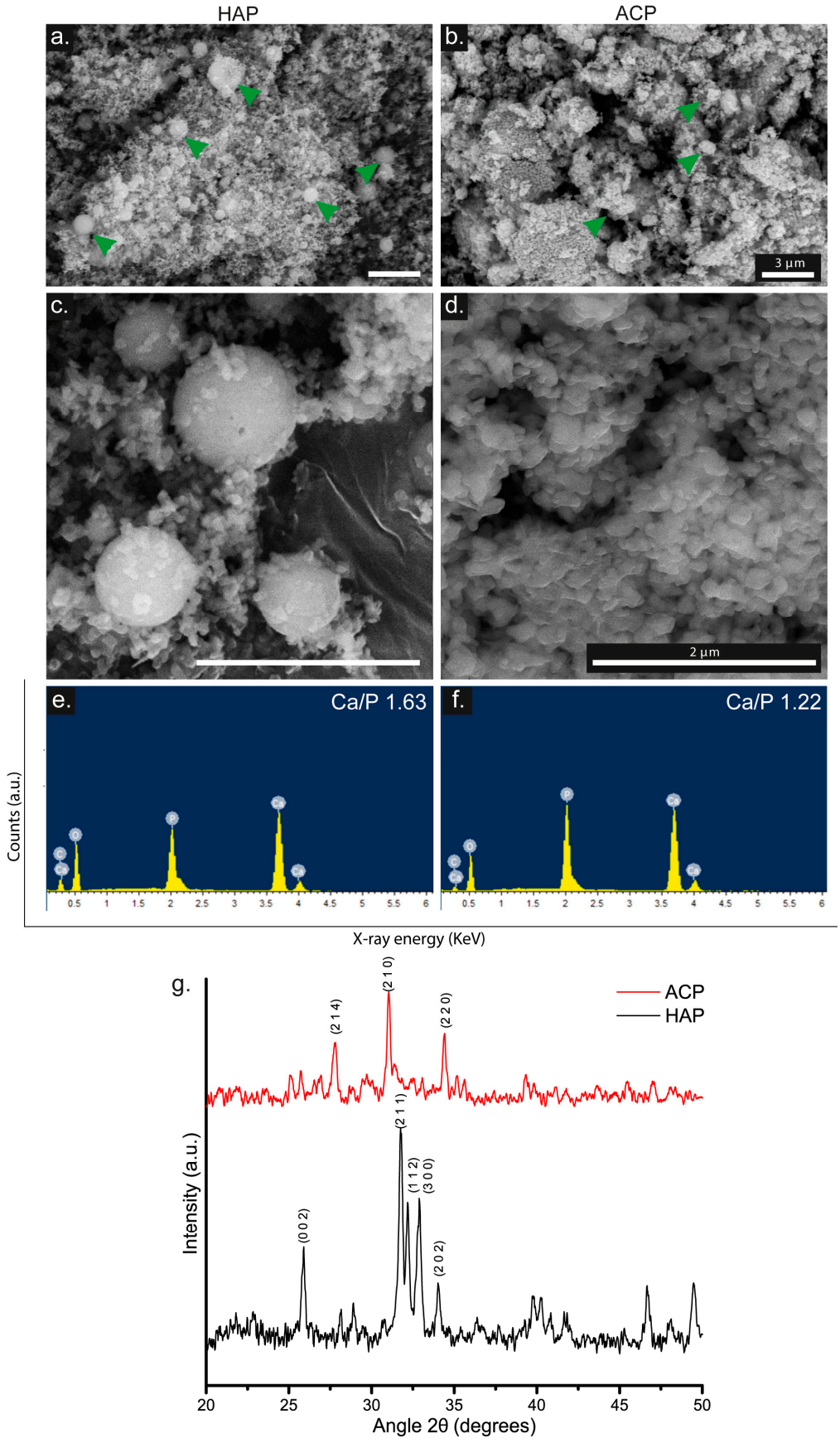


Figure 1. SEM images of (**a**,**c**) HAP and (**b**,**d**) ACP (Scale Bar = 3 µm; green arrows indicate the bioceramic). EDS spectrum of (**e**) HAP and (**f**) ACP. (**g**) XRD pattern of HAP and ACP.

3.2. FTIR-ATR of Electrospun Scaffolds

The infrared spectra shown in Figure 2, sections d–f show signals that match the functional groups found in PLA. Specifically, three higher intensity bands are visible at 1751 cm^{-1}, 1184 cm^{-1}, and 1087 cm^{-1}, corresponding to the stretching of the C=O bond, the asymmetric stretching of the C-O-C (ester) group, and the asymmetric stretching of the C-O-C (ether) group, respectively [40].

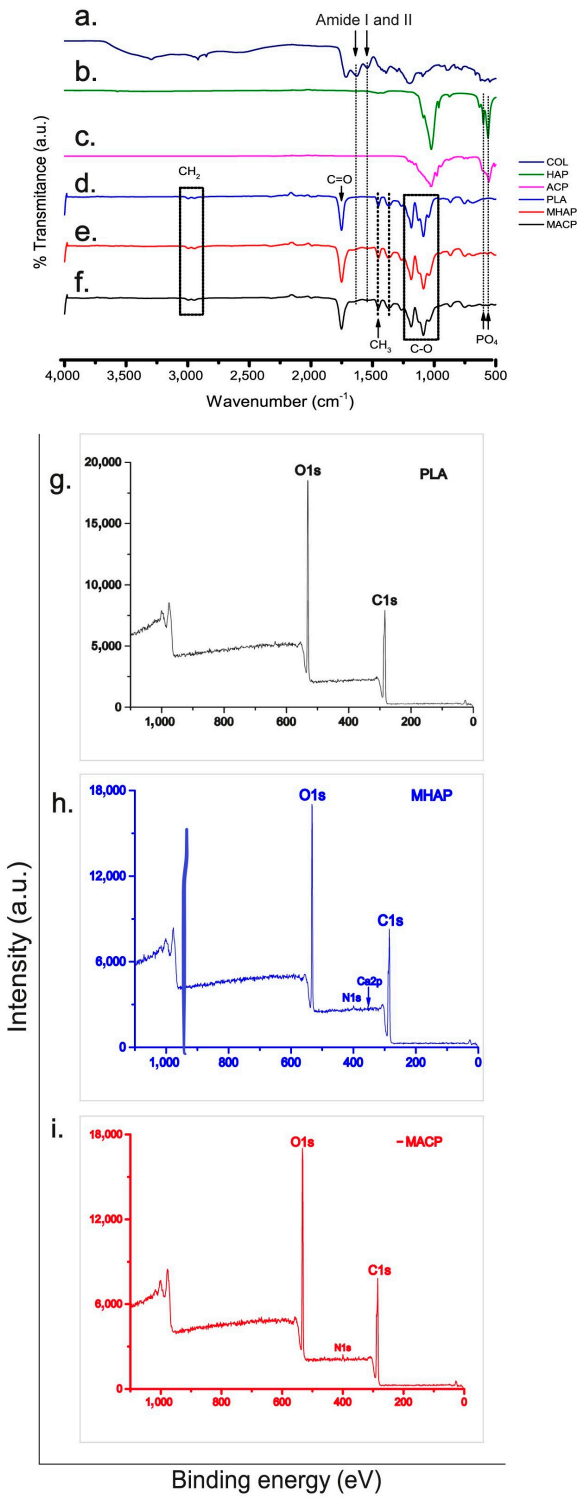


Figure 2. Infrared spectra of (**a**) COL, (**b**) HAP, (**c**) ACP, (**d**) PLA, (**e**) MHAP, and (**f**) MACP. XPS spectrum of (**g**) PLA, (**h**) MHAP, and (**i**) MACP scaffolds.

The MHAP and MACP spectra (Figure 2e,f) exhibit vibrations that correspond to the amide I observed at 1651 cm^{-1} and amide II observed at 1546 cm^{-1} of collagen (Figure 2a) [41]. Furthermore, the vibrational modes of the PO_4^{-3} group at 604 cm^{-1} and 567 cm^{-1}, which are particular to calcium phosphates (HAP and ACP, Figure 2b,c), are also present [42]. However, due to the concentrations of these components in the membrane, the signals are weak and may overlap with the vibrations of the polyester.

3.3. XPS

The XPS spectra (Figure 2g–i) reveal the elemental composition and chemical bonding of the materials on the scaffold surface. The PLA scaffold (Figure 2g) exhibits characteristic C1s and O1s signals, indicating the presence of this aliphatic polyester. Similarly, the MHAP and MACP scaffolds (Figure 2h and 2i, respectively) display the C1s and O1s signals along with the N1s and Ca2p signals, indicating the existence of COL and calcium phosphate compounds on the scaffold surface. The deconvoluted signals from each XPS spectrum are depicted in Supplementary Figure S1.

The C1s signals exhibit three distinct bands related to the C-C/C-H, C-O, and O-C=O bonds, ranging from 284.5 eV to 289.9 eV. This implies the existence of carbon in varying chemical environments, likely due to the different components of the scaffolds. The O1s signals reveal the O-C=O* and *O-C=O bands, ranging from 531.5 eV to 534.2 eV, indicating the presence of oxygen in distinct bonding environments, predominantly in carbonyl groups. The peak at 400.3 eV in the N1s signal suggests the presence of nitrogen in the collagen element of the scaffolds [43]. The calcium signal in MHAP exhibits two peaks, namely the 2p 1/2 and 2p 3/2 bonds, with binding energies of 347.7 eV and 351.3 eV, respectively [44]. These peaks indicate calcium's binding to phosphate groups, which is in line with the literature. This confirms the presence of hydroxyapatite in the scaffold, as calcium is found in a chemical environment common to calcium phosphates [45,46].

A detection around 135 eV was expected for the phosphorus signal, but an abnormally low intensity was observed. This phenomenon is in line with Deng et al. results [44], which suggest that it could be due to the prevalent distribution of HAP particles within the fibers, without any exposure on their surface. Notably, no foreign elements are present in the materials used, as evidenced by the spectra.

3.4. SEM

The SEM images shown in Figure 3a–c display scaffolds featuring crosslinked fibers with even surfaces, uniform diameters, and no defects or beads. It is worth mentioning that the MHAP scaffold (Figure 3b) displays some agglomerations less than one micrometer in size, while the MACP scaffold (Figure 3c) exhibits agglomerations of approximately three micrometers deposited onto the electrospun fibers (green arrows). This phenomenon is caused by the non-homogeneous inorganic compound within the polymer solution.

To establish the fiber diameter, measurements were performed on every scaffold with ImageJ software (https://imagej.net/software/fiji/downloads (accessed on 1 May 2023)). The fiber diameter was determined by perpendicular measurements of their width at various points along their longitudinal axis. At least 60 fibers of each scaffold type were analyzed using ImageJ software (https://imagej.net/software/fiji/downloads (accessed on 27 July 2023)), from which the average diameter and standard deviation of the fibers constituting the electrospun scaffolds were calculated. The results demonstrated that the mean fiber diameter (Figure 3d–f) in the PLA scaffold was 412 ± 58 nm. In contrast, the mean diameters in the MHAP and MACP scaffolds were 240 ± 33 nm and 297 ± 81 nm, respectively. This indicates a reduction in the fiber diameter of up to 42% in the MHAP and MACP scaffolds due to the incorporation of COL and the calcium phosphate compounds into these scaffolds. Additionally, EDX (Figure 3g–i) also displays the elemental makeup of every scaffold, with MHAP and MACP retaining their Ca/P ratio.

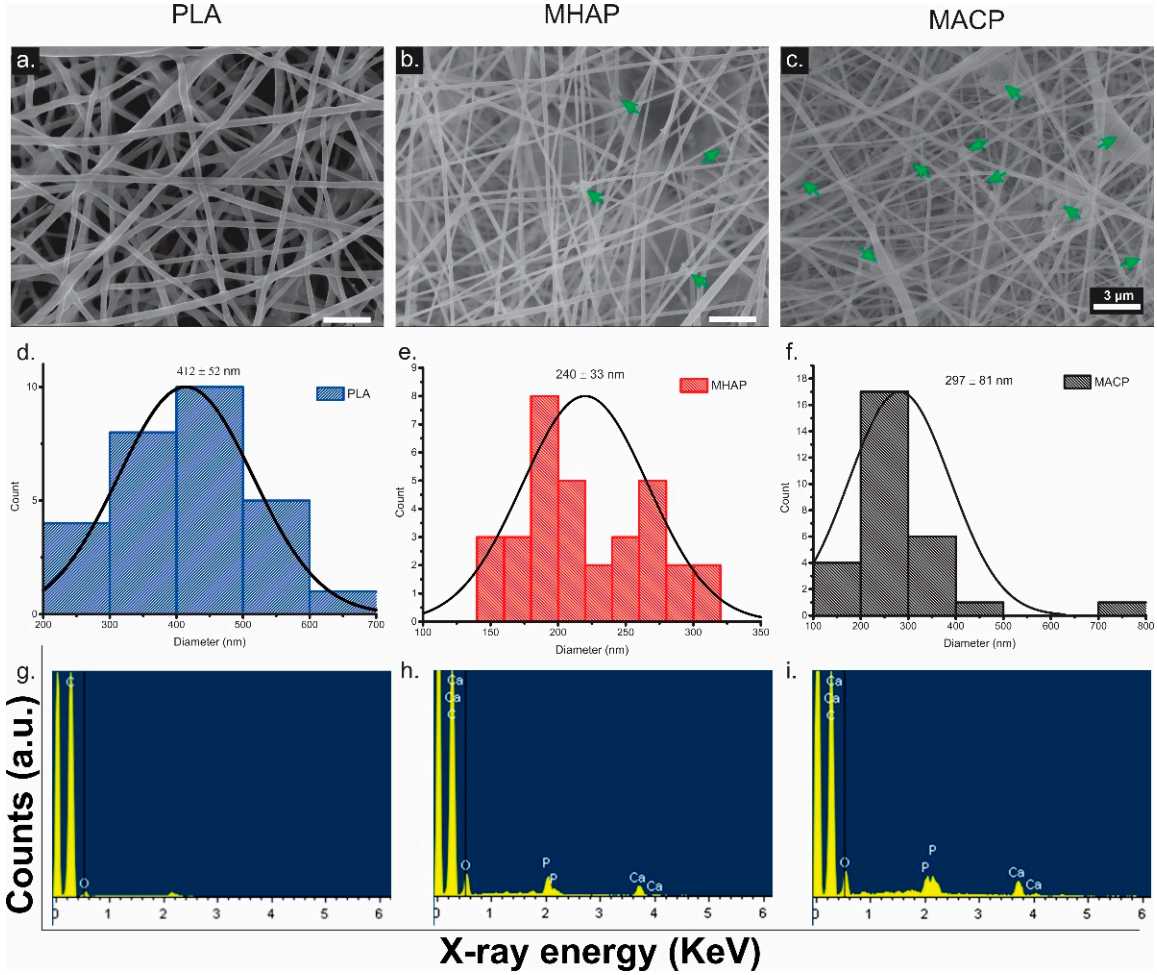


Figure 3. SEM images of electrospun scaffolds of (**a**) PLA, (**b**) MHAP, and (**c**) MACP. (Scale bar = 3 µm, green arrows indicate CaP). Histogram of fiber diameters of (**d**) PLA, (**e**) MHAP, and (**f**) MACP electrospun scaffolds. EDX spectra of (**g**) PLA, (**h**) MHAP, and (**i**) MACP scaffolds.

3.5. DSC

Figure 4a–c illustrates the thermal behavior of three scaffolds. All scaffolds displayed two endothermic signals at 60 °C and 166 °C, as well as one exothermic signal at 87 °C. These signals were associated with the glass transition, melting, and crystallization of PLA, respectively [47]. Comparing the PLA scaffold (Figure 4a) to the MHAP and MACP scaffolds (Figure 4b,c), we observe a decrease in the crystallization temperature (Tc) and an increase in the melting temperature (Tm). The presence of COL and calcium phosphate compounds during the fiber formation in electrospinning modified the thermal behavior of the scaffold. Table 2 summarizes the temperatures and enthalpies calculated for each signal utilizing TA Instruments software (https://www.tainstruments.com/soporte/software-downloads-support/descargas/?lang=es (accessed on 27 July 2023)).

Table 2. Temperatures and enthalpies of MHAP, MACP, and PLA scaffolds.

Scaffold	Tg (°C)	Δ*Hg* (J/°C)	Tc (°C)	Δ*Hc* (J/°C)	Tm (°C)	Δ*Hm* (J/°C)
MHAP	60.29	2.62	79.88	10.80	170.16	35.28
MACP	60.59	4.14	78.64	11.76	169.42	35.04
PLA	59.47	6.91	87.76	13.79	166.16	38.51

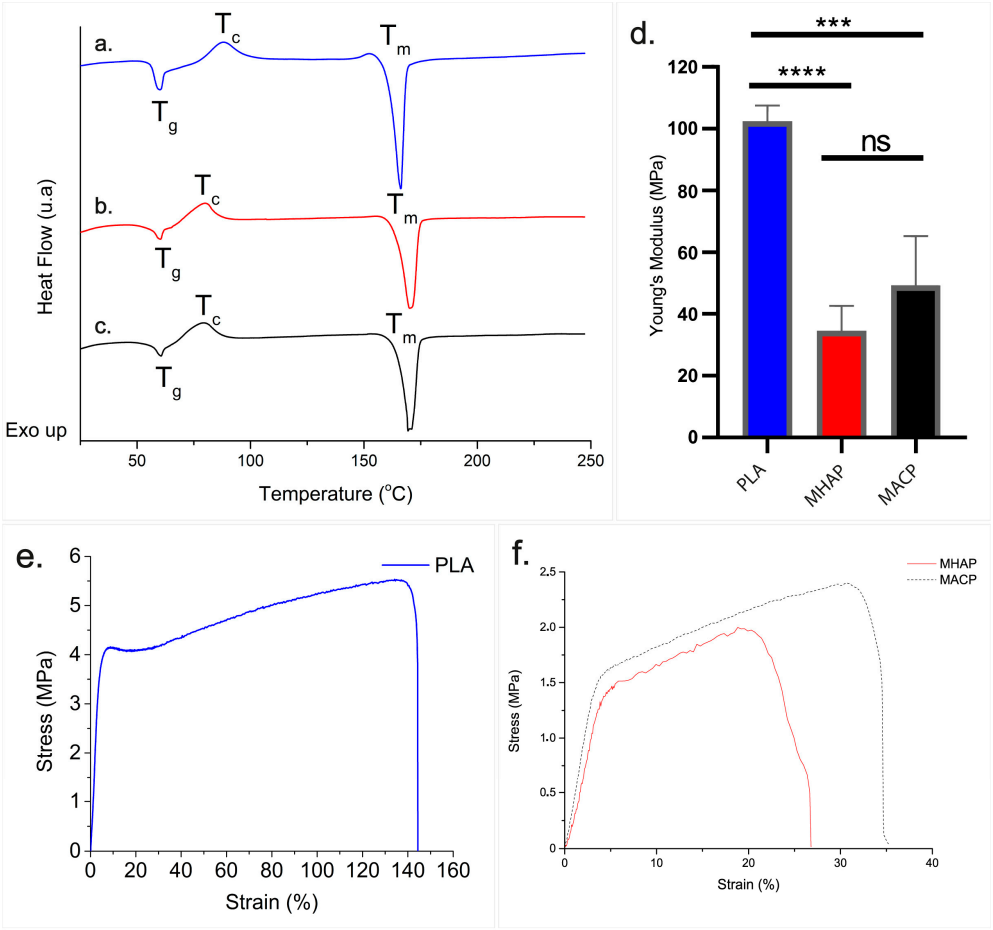


Figure 4. DSC of (**a**) PLA, (**b**) MHAP, and (**c**) MACP electrospun scaffolds. (**d**) Young's modulus of the scaffolds (*** $p < 0.001$, **** $p < 0.0001$, ns: no significative). Stress vs. strain plot of (**e**) PLA and (**f**) MHAP and MACP electrospun scaffolds.

From the values of the crystallization and melting enthalpies of PLA in each scaffold, the percent crystallinity of the polymer in the scaffolds was determined using Equations (1) and (2) [48].

$$Xc = \frac{\Delta H_m - \Delta H_c}{\Delta H_m^*} \times 100\% \quad (1)$$

where ΔH_m is the enthalpy of fusion of the sample, ΔH_c is the enthalpy of crystallization, and ΔH^*_m is the theoretical enthalpy of fusion of crystalline PLA (93.7 J/g) [49]. The absolute crystallinity of PLA in the scaffolds was calculated as *Xp*:

$$Xp = \frac{Xc}{w} \quad (2)$$

where w is the weight fraction of PLA in the scaffolds.

According to the calculations, the PLA, MHAP, and MACP scaffolds obtained crystallinity values of 26.38%, 31.47%, and 29.82%, respectively.

3.6. Young's Modulus of Scaffolds

The uniaxial traction test of the scaffolding was carried out with a relative humidity of 55%. The Young's modulus values (Figure 4d) and stress-strain diagram (Figure 4e,f) of each scaffold are presented in Figure 4.

The Young's modulus values were calculated by determining the slope of the stress-strain diagram within the elastic zone for every scaffold. The PLA scaffold displayed values

of 102 MPa ± 4 MPa, whereas the MHAP and MACP scaffolds showed a decrease with values of 34 MPa ± 7 MPa and 49 MPa ± 13 MPa, respectively.

The stress-strain diagram of electrospun PLA (Figure 4e) shows a deformation close to 7% with 4 MPa of uniaxial yield stress. Beyond the elastic limit, the polymer undergoes up to a 143% plastic deformation with an ultimate stress point of around 5.5 MPa. On the contrary, the elastic limit of both the MHAP and MACP scaffolds is reached (as shown in Figure 4f) at 1.45 MPa and 1.55 MPa, respectively, which corresponds to the yield stress, leading to a 5% and 4% deformation, respectively. Additionally, the plastic deformation is reduced to 20% for MHAP and 32% for MACP in these electrospun polymer matrices, each with an ultimate stress point of approximately 1.9 MPa and 2.4 MPa, respectively. This suggests that MHPA and MACP have lower elastic properties (Young's modulus and yield stress) compared to PLA, resulting in less mechanical resistance. Additionally, PLA has greater ductility when plastically deformed, while MHPA and MACP are more brittle.

3.7. Adhesion and Proliferation Cellular

Fluorescence microscopy was used to observe the distribution and adhesion of hWJ-MSCs-GFP on electrospun scaffolds. Cells with an elongated morphology and extended filopodia were present on all three scaffolds from the first day of culture. However, the adhesion of cells on the MACP scaffold (Figure 5g–i) was greater than that on the MHAP (Figure 5d–f) and PLA (Figure 5a–c) scaffolds, with more cells present on the scaffold on days 3 and 5 compared to the other two scaffolds. These results indicate that the MACP scaffold provides better support for cell adhesion and proliferation.

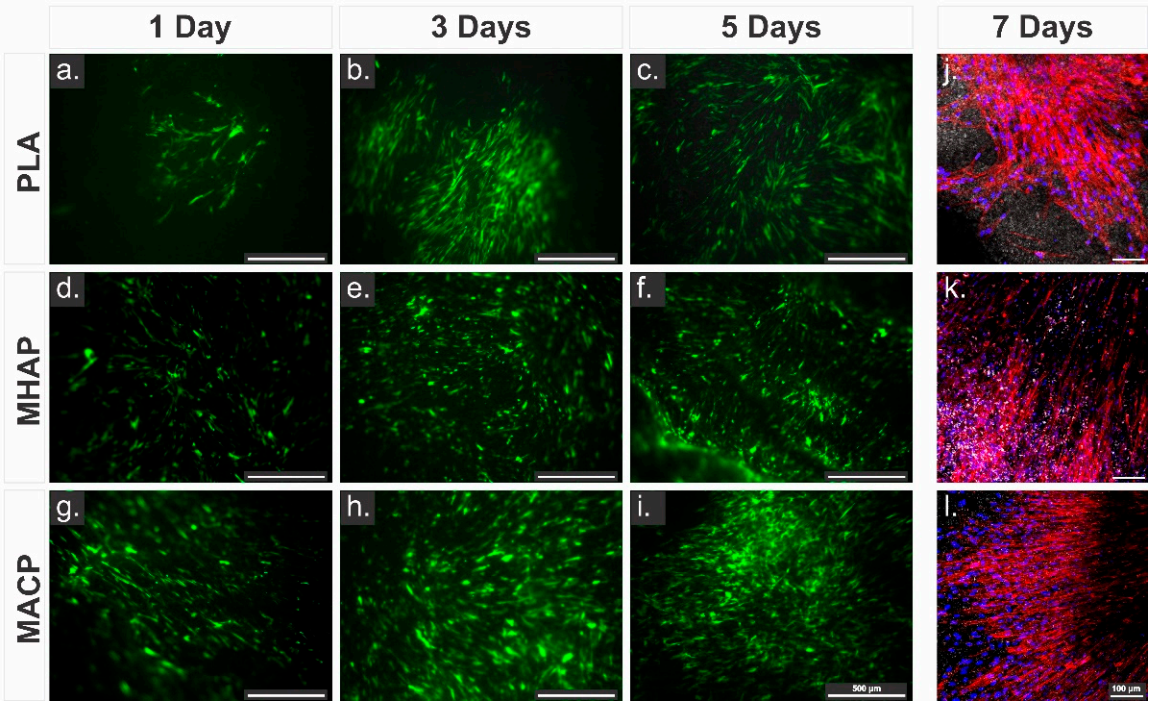


Figure 5. hWJ-MSCs-GFP seeded on electrospun scaffolds and imaged at different time points. (**a**–**c**) PLA scaffolds, (**d**–**f**) MHAP scaffolds, and (**g**–**i**) MACP scaffolds (Scale bar = 500 µm, Green color show the presence of GFP-transduced cells.) and confocal images of hWJ-MSCs staining with DAPI (blue) and red phalloidin (red) seeded 7 days on (**j**) PLA, (**k**) MHAP, and (**l**) MACP scaffolds (Scale bar = 100 µm).

Figure 5j–l shows the confocal microscopy images of the cytoskeleton (red, phalloidin) and nuclei (blue, DAPI) of hWJ-MSCs on the electrospun scaffolds. Several spindle-shaped spreading cells adhered to the scaffolds. Furthermore, all three scaffold types show a well-developed cytoskeletal arrangement characterized by network-like structures and

robust interconnections with neighboring cells. Correspondingly, the fluorescence analysis shows that the incorporation of COL and calcium phosphate compounds increases cell density. In particular, the MACP scaffold (Figure 5l) shows the highest cell density among the scaffolds.

The effects of the scaffolds on cell viability were examined by resazurin assay (Figure 6a). The non-cytotoxicity and cell compatibility related to the MACP and MHAP scaffolds were observed compared to the control (hWJ-MSCs on TCP) at 24 and 48 h, which confirms the biocompatible nature and safety of these scaffolds for their possible use in clinical applications [50].

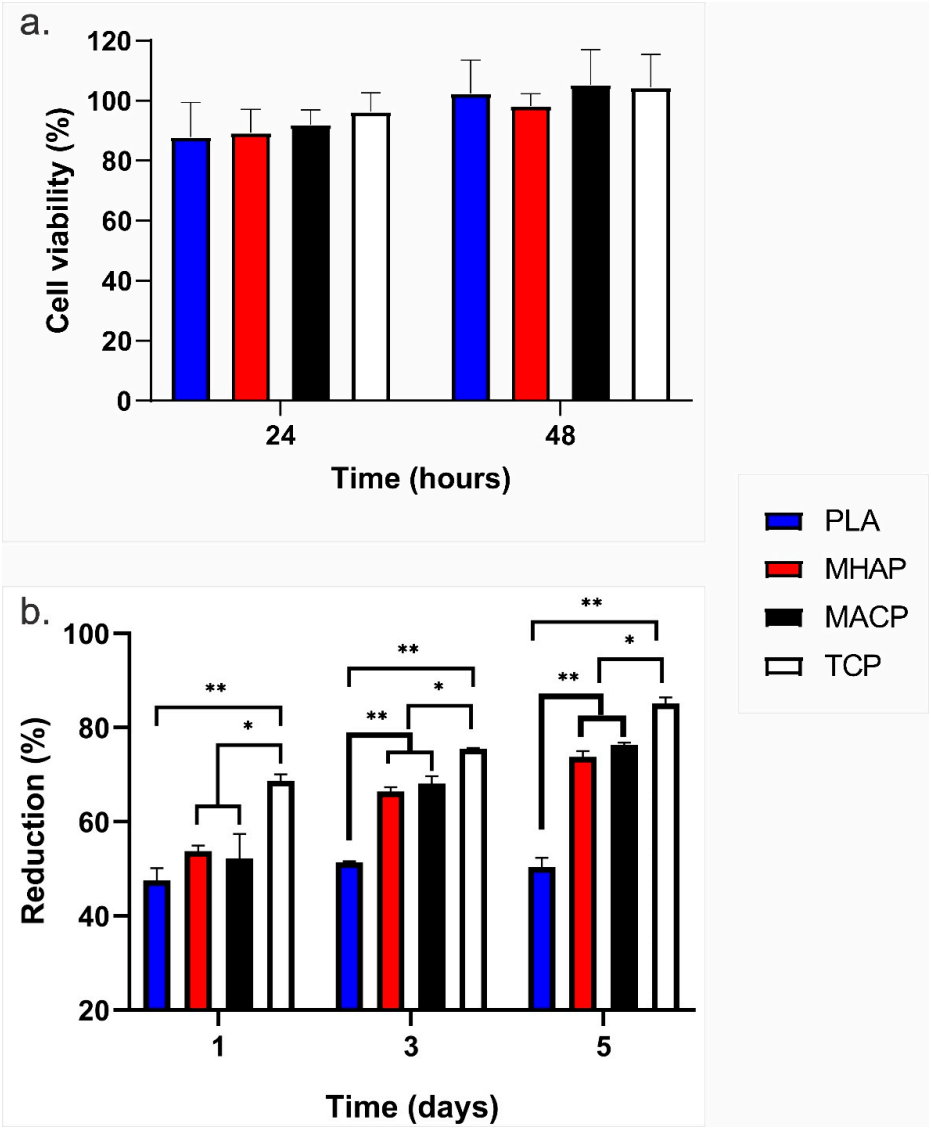


Figure 6. (**a**) Cell viability of hWJ-MSCs cultured in direct contact with PLA, MHAP, and MACP scaffolds for 24 and 48 h. (**b**) Proliferation of hWJ-MSCs seeded on PLA, MHAP, MACP, and TCP scaffolds (* $p < 0.05$, ** $p < 0.01$).

Similarly, the proliferation of hWJ-MSCs seeded on the PLA, MHAP, MACP and TCP scaffolds is shown in Figure 6b. On the first day of the culture, cell proliferation was 40% in the PLA scaffolds, whereas it exceeded 50% in the MHAP and MACP scaffolds. Subsequently, the cell proliferation in the MACP and MHAP scaffolds surpassed 60% and 75% after three and five days, respectively, while the PLA scaffold attained values approximating 50%. Note that starting from the third day of culture, the MHAP and MACP

scaffolds displayed a significant deviation compared to the PLA scaffold, which suggests the impact of COL and CaPs on cell proliferation within these scaffolds. Additionally, significant differences in cell proliferation were observed between the scaffolds and the control (TCP) at all evaluated time points.

3.8. Quantification of Growth Factors

The growth factors quantified in this study play a role in bone healing [51]. We measured the secretion of basic fibroblast growth factor (bFGF), transforming growth factor beta 1 (TGF-β1), angiopoietin-1, and platelet-derived growth factor bb (PDGF-bb) in all conditions (PLA, MACP, and MHAP).

Additionally, we analyzed the culture-supplemented medium to determine the concentration of growth factors in the medium. Likewise, the cells cultured in standard tissue culture plates (TCP) were used as a control to determine the secretory factors under typical culture conditions. The secretion of bFGF by cells cultured in the MACP scaffold was the highest after 24 and 48 h of culture. At 48 h, the MACP constructs had a bFGF concentration of 133 pg/mL, compared to 93 pg/mL in the MHAP, 30 pg/mL in the polylactic acid (PLA) scaffold, and 8.6 pg/mL in the TCP. These concentrations exhibited significant differences ($p < 0.05$ for PLA and $p < 0.01$ for TCP) (Figure 7a).

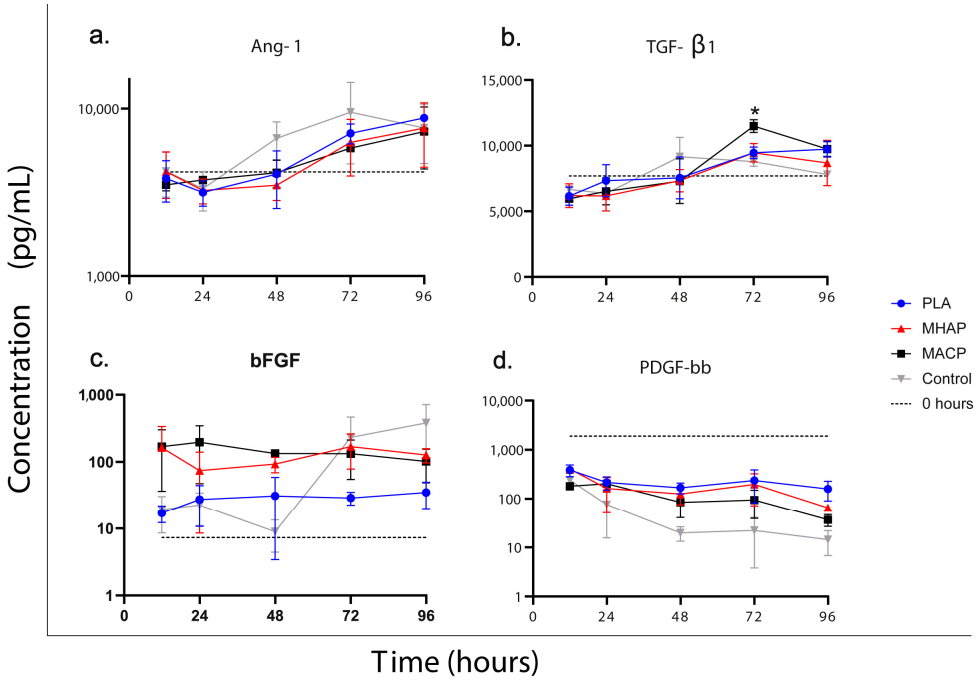


Figure 7. Quantification of (**a**) angiopoietin-1, (**b**) transforming growth factor beta 1, (**c**) basic fibroblast growth factor and (**d**) platelet-derived growth factor bb evaluated in hWJ-MSCs seeded on PLA, MHAP, MACP, and TCP scaffolds. Different signs in the same graph indicate significant differences (* $p < 0.05$) PLA vs. other treatments.

On the other hand, both TGF-β1 and angiopoietin-1 demonstrated similar behavior in all conditions. Their values were lower (7688 pg/mL and 4190 pg/mL, respectively) than those found in the culture medium for up to 48 h. However, after 72 h, their production became evident, with TGF-β1 reaching 10,300 pg/mL and angiopoietin-1 reaching 12,900 pg/mL (see Figure 7b,c). PDGF-bb, on the other hand, showed a trend of consumption in all treatments, with an initial concentration of 1900 pg/mL in the culture medium. It was gradually reduced in all treatments to values ranging from 120 pg/mL (PLA) to 15 pg/mL (TCP) over the evaluated period (Figure 7d).

3.9. Calcium Phosphate Compounds-Containing Scaffolds Induce the Osteogenic Differentiation of hWJ-MSCs

Considering the potential of hWJ-MSCs to differentiate toward osteogenic lineages, we finally sought to test whether hWJ-MSCs cultured on PLA, MHAP, and MACP could induce their differentiation toward osteogenic lineages. The hWJ-MSCs were seeded on the PLA, MHAP, and MACP scaffolds and cultured with the supplemented DMEM and osteogenic differentiation medium. After 7 days of culture, samples of PLA/hWJ-MSCs, MHAP/hWJ-MSCs, and MACP/hWJ-MSCs were fixed for evaluation by SEM, alizarin red staining, and immunohistochemical detection of osteocalcin.

SEM images showed cell adhesion in all scaffolds, but the inherently hydrophobic nature of the PLA scaffold resulted in a lower number of cells present (Figure 8a–l). Conversely, the MHAP scaffold showed higher cell density when cultured with the osteogenic differentiation medium. Furthermore, when hWJ-MSCs were seeded onto the MACP scaffold, they formed a uniform and dense cell layer covering the electrospun fibers, with cells evenly distributed throughout the scaffold. Extracellular matrix (ECM) formation and prominent cell extensions were observed, indicating the presence of a three-dimensional network of proteins and molecules secreted by the cells into their environment. This network provides structural and biochemical support and suggests a beneficial interaction between cells and the scaffold, enabling cell adhesion and growth in the scaffold environment [52].

To evaluate the mineralization of hWJ-MSCs on the scaffolds cultured with supplemented DMEM and osteogenic culture media, we performed alizarin red staining after 7 days of culture. The staining shows an increase in staining intensity for both the MHAP and MACP scaffolds (Figure 8m). This increase in staining is evident in the scaffolds cultured in both supplemented DMEM and osteogenic differentiation media. The formation of calcium-rich deposits in the scaffold indicates the ability of these matrices to promote bone differentiation processes [53,54]. In the PLA/hWJ-MSCs, low formation of calcium deposits was observed in the scaffold exposed to the osteogenic differentiation medium [54]. No mineralization was observed in the cells seeded in TCP (Figure 8m).

Similarly, immunohistochemical analyses performed on the MHAP (Figure 9a,b,e,f) and MHAP (Figure 9c,d,g,h) scaffolds show staining for osteocalcin, indicating the potential of these scaffolds to induce osteogenic differentiation. The PLA and TCP controls (Supplementary Figure S2) did not show staining, which may indicate that CaPs in the scaffolds induce cell differentiation to the osteogenic lineage. More intense staining for osteocalcin expression was observed in the MACP scaffold, suggesting a microenvironment conducive to the process of osteogenesis. Similarly, the MHAP scaffold showed a slightly reduced but still notable level of osteocalcin presence, indicating its potential to stimulate osteogenic activity. These results highlight the influence of scaffold composition on cellular behavior and suggest that both the MACP and MHAP scaffolds have great potential in bone tissue engineering.

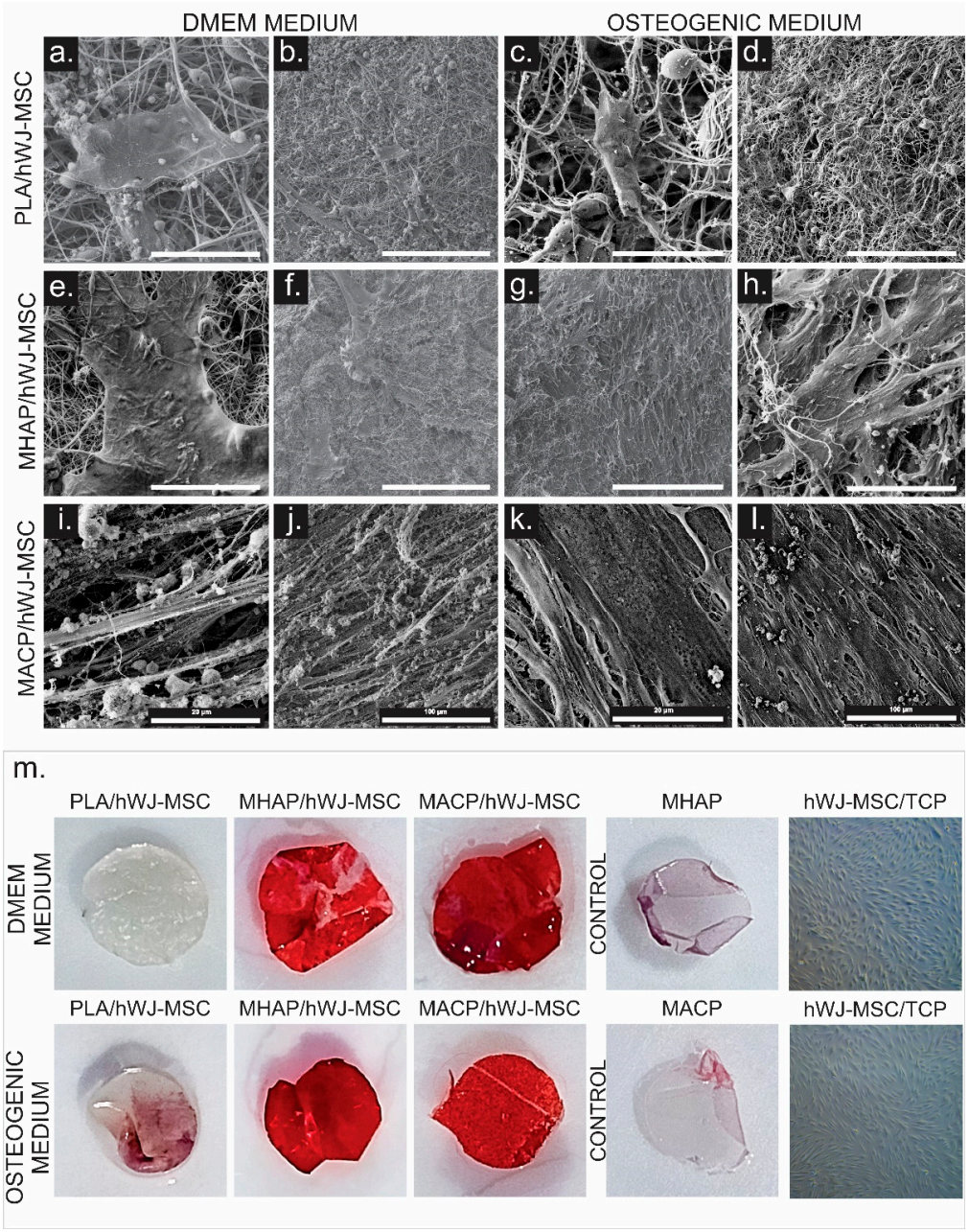


Figure 8. SEM images of hWJ-MSCs seeded on PLA, MHAP, and MACP scaffolds. Images (**a**,**b**,**e**,**f**,**i**,**j**) show cells cultured with the supplemented DMEM medium, while images (**c**,**d**,**g**,**h**,**k**,**l**) show cells cultured with the osteogenic differentiation medium. Image (**m**) shows alizarin red staining performed on PLA, MHAP, and MACP scaffolds with hWJ-MSCs seeded with both the supplemented DMEM medium and osteogenic differentiation medium.

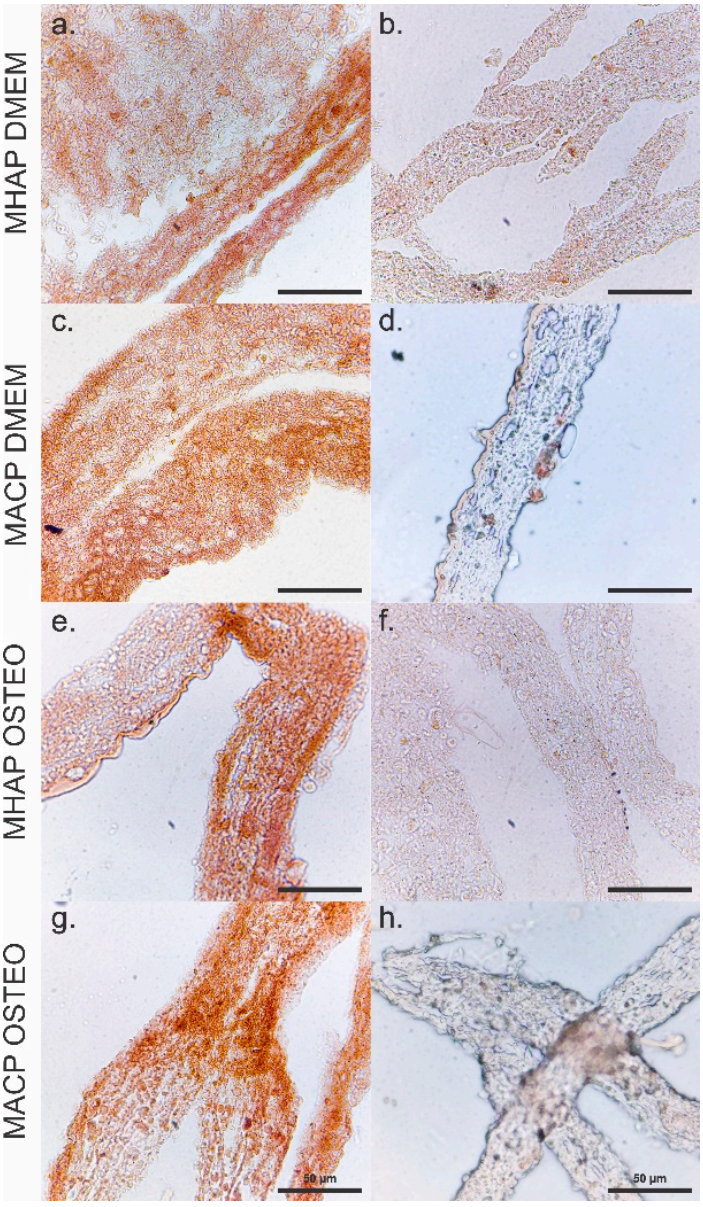


Figure 9. Osteocalcin immunohistochemical staining of hWJ-MSCs seeded on MHAP and MACP scaffolds after 7 days of culture with (**a**,**c**) and without (**e**,**g**) osteogenic media condition. Negative control staining for scaffolds cultured in the DMEM medium (**b**,**d**) and scaffolds cultured in the osteogenic differentiation medium (**f**,**h**). Scale bar = 50 µm.

4. Discussion

A tissue engineering strategy that relies on scaffolds seeded with MSCs is a promising approach for treating bone defects. Currently, we have a good understanding of how various scaffold characteristics can affect cell behavior and the efficiency of the regenerative process. For instance, it is known how the scaffold materials can affect cell infiltration, viability, migration, and differentiation. HAP is one of the main inorganic compounds used in bone tissue engineering matrices. However, studies have shown a slow dissolution rate that hinders bone repair [55]. As a result, researchers have turned to ACP as a substitute. ACP has a structural unit similar to HAP, which allows it to play a critical role in apatite formation both in vitro and in vivo. ACP has a disordered structure that confers high reactivity in body fluids, resulting in high solubility and the rapid precipitation of apatite [56].

SEM images demonstrated that ACP exhibits a rougher surface and greater dimensional variability compared to HAP, which had a smoother surface and uniform sizes. Also, the dimensions of the hydroxyapatites affect their distribution in the scaffolds, since the size of the HAP allows it to be more easily and homogeneously distributed on the electrospun fibers. In contrast, the MACP scaffold deposits amorphous calcium phosphate in agglomerations of mostly over 1 micron inside the scaffold and a small amount on the electrospun fibers.

Regarding the EDX spectrum, it indicates that ACP has a Ca/P ratio indicative of a predominantly amorphous ceramic, whereas HAP has a ratio indicative of a crystalline ceramic [57]. When comparing our amorphous calcium phosphate with the results of Abidi et al. [30], differences in Ca/P were found. These differences are attributed to variations in the pH level of the solution during the bioceramic synthesis. The XRD analysis allowed the identification of the ACP phase, characterized by its minimal crystallinity, with no other phases detected within the defined limits of detection. The data indicates that the detected signal aligns with the peaks of a β-TCP structure. However, it should be noted that the crystalline structural formation of this bioceramic necessitates temperatures exceeding 500 °C [58]. Considering the synthesis conditions, morphology, Ca/P ratio, and XRD results of the ACP ceramic, it can be inferred that it is largely composed of amorphous CaP. The compositional profile of ACP is particularly dependent on the pH level of the solution and the concentrations of the mixed solutions, resulting in different Ca/P ratios ranging from 1.18 to 2.5 [59]. There is an ongoing debate regarding the apatitic nature of ACP, with one perspective suggesting that its apatitic structure consists of extremely fine crystals, rendering it X-ray amorphous. Alternatively, one hypothesis suggests that the basic structural unit of ACP is a roughly spherical ion cluster with a diameter of 9.5 Å and a composition of $Ca_9(PO_4)_6$ [60]. These clusters are the initial nuclei during the crystallization of hydroxyapatite, supporting a model that elucidates hydroxyapatite formation as a stepwise assembly of these basic units [61].

On the other hand, the morphological evaluation of electrospun scaffolds revealed that the fibers obtained from all treatments had a random submicron distribution without defects or beads. This confirms that the parameters used were appropriate for obtaining smooth and homogeneous electrospun fibers. Furthermore, imaging revealed a decrease in fiber diameter in the MACP and MHAP scaffolds due to COL and CaPs compounds. These materials increase polarity and Coulomb interaction forces, thereby increasing electrostatic repulsion, reducing fiber diameter, and producing high surface area scaffolds [62]. This feature helps to create a network of interconnected micropores that promote cell signaling and the transport of nutrients and factors during tissue regeneration [63].

Another important feature of a bone scaffold is its chemical composition, which must have functional groups, such as those provided by COL and HAP, that promote cell adhesion, proliferation, and differentiation. The incorporation of COL and CaPs compounds into the scaffolds was confirmed by the visualization of amide groups I and II and phosphate groups by FTIR-ATR and N1s and Ca2p signals by XPS. In addition, the DSC analysis has demonstrated that these materials enhance the melting enthalpy of scaffolds, which is linked to the recrystallization of the polyester. Because PLA crystallizes at a slow rate and its glass transition temperature (Tg) is greater than the ambient temperature (T amb), a crystalline fraction of this polyester exists that facilitates recrystallization during electrospinning [64]. The presence of hydroxyapatites constrains the mobility of the PLA molecular chain during recrystallization. It serves as a site for nucleation that promotes the formation of flawed crystals [65], which demand less energy but a higher temperature to liquefy, leading to a Tm shift in these frameworks [66]. The thermal changes of the scaffolds (Tg, Tc, and Tm) are located at temperatures exceeding 38 °C; thus, the physical temperature would not impact the features of the PLA, MHAP, and MACP frameworks. In addition, polymer degradation may be facilitated by microstructural changes, as highly crystalline PLA takes longer to degrade [67]. Also, the polymer microstructure underwent changes due to the aggregation of organic and inorganic compounds. The addition of CaPs to the

MHAP and MACP scaffolds significantly affected their mechanical properties. This was due to a decrease in the yield stress and Young's modulus in the scaffolds, mainly caused by the aggregation of CaPs. Such an aggregation affected the intermolecular linkages within the PLA molecules, resulting in a higher incidence of mesostructural defects within the polymer. As a result, the ability of the scaffolds to stretch before reaching the failure point was greatly reduced [25,36,68].

The in vitro cellular response of the electrospun scaffolds was evaluated with hWJ-MSCs. The scaffolds demonstrated non-cytotoxicity by meeting the ISO 10993-5 standards with values above 75%, which is similar to other literature reports using these materials [69,70]. The MACP scaffold demonstrated greater in vitro adhesion and proliferation of hWJ-MSCs than both the MHAP and PLA scaffolds. These findings align with those presented in Zhao et al.'s study, which utilized electrospun ACP scaffolds and MG63 cells [25]. Moreover, cellular receptors, including glycoprotein VI, integrins, discoidin domain receptors, and receptors with an affinity for non-collagenous domains, detect specific COL peptide sequences that regulate cell behaviors, such as adhesion, differentiation, and proliferation [71]. COL also plays a crucial role in tissue regeneration by contributing to the retention, local storage, and delivery of growth factors or cytokines [72].

Additionally, the Luminex analysis revealed that cells seeded on the MACP scaffolds during the initial 48 h secreted higher levels of bFGF compared to MHAP, PLA, and the control. bFGF is a critical growth factor for bone regeneration and its presence influences many mesodermal and neuroectodermal cell types. As for TGF-β1 and angiopoietin 1, the production of these growth factors was observed after 48 h of culture. The concentrations at each time point were comparable between the scaffolds, except for a higher TGF-β1 production observed in the PLA scaffold at 72 h. However, by 96 h, the levels of this factor in the PLA scaffold were similar to those in the other treatments. Finally, the concentration of PDGFbb decreases in all treatments over time, suggesting that hWJ-MSCs are consuming this factor. This phenomenon is attributed to the high concentration of this factor in the platelet lysate [73]; therefore, the cells do not produce it but rather consume it.

TGF-β1 and PDGF-bb factors are stimulated upon injury to promote the proliferation of mesenchymal cells and osteoblasts in fractures and experimental bone defects (37). Additionally, Angiopoietin-1 facilitates vascular growth and promotes the formation of new blood vessels to enable oxygen, nutrients, osteoinductive factors, and stem cells to reach the damaged area. It also aids in the formation of the vascular wall, promoting the migration of osteoblast precursor cells to the target site [74]. The secretion of these growth factors stimulates the recruitment and storage of growth factors involved in bone formation and repair [75].

Notably, the MACP scaffolds not only facilitate cell adhesion and proliferation and stimulate the release of growth factors associated with bone repair, but also have the remarkable ability to induce the formation of calcium reservoirs, an extracellular matrix, and essential bone regeneration peptides, including osteocalcin by hWJ-MSCs. These findings provide further insight into the bioactive potential of the MACP scaffolds in the field of bone regeneration. The extracellular matrix is actively synthesized by the cells on the scaffolds, either in the supplemented DMEM medium or in the specialized osteogenic differentiation medium, to the extent that it completely covers the scaffold surface. The observed extracellular matrix indicates a beneficial interaction between the scaffold and the cells. This interaction suggests that the environment is conducive to bone differentiation and repair [76]. With respect to osteocalcin, the staining intensity indicates increased production of this protein in the MACP scaffolds with hWJ-MSCs. OCN, a major non-collagenous protein in the bone matrix, is present at high levels during bone formation and has the ability to directly or indirectly influence bone mass, mineral size, and alignment [77].

5. Conclusions

This study comprehensively characterizes hydroxyapatite (HAP) and amorphous calcium phosphate (ACP) and their incorporation into electrospun scaffolds, highlighting their potential for bone tissue engineering. The SEM analysis reveals distinct morphological differences between HAP and ACP, with HAP exhibiting uniform particle size and a smooth surface, while ACP forms irregular aggregates with a rough texture. The Ca/P ratio variations are verified by the EDX analysis. Successful scaffold incorporation is demonstrated by the FTIR-ATR spectra, and calcium binding to phosphate groups is revealed by the XPS analysis. The addition of collagen and calcium phosphate causes changes in thermal behavior, as indicated by the DSC results. Young's modulus values evidence the changes in scaffold mechanics. Cellular studies showed that the MACP scaffolds significantly increased the adhesion, proliferation, osteogenic differentiation, and growth factor secretion of hWJ-MSCs. In addition, SEM and alizarin red staining demonstrated their mineralization potential, positioning the MACP scaffolds as promising candidates for bone tissue engineering. These results highlight the critical role of scaffold composition in influencing cellular behavior and tissue regeneration. Future research aims to evaluate the mineralization of MACP in simulated body fluid (SBF) following ISO 23317:2014 standards to demonstrate the viability of calcium phosphates incorporated in scaffold matrices for use in biomedical applications. It should be noted that the degradation of these types of scaffolds has yet to be comprehensively understood. Therefore, our ongoing research endeavors to address these critical knowledge gaps. This study offers insight into the intricate function of calcium phosphates in regulating mineralization processes and degradation mechanisms of scaffolds, thereby improving their potential for biomedical applications.

Supplementary Materials: The following supporting information can be downloaded at: https://www.mdpi.com/article/10.3390/pharmaceutics15112529/s1, Figure S1: Deconvolution of the C1s, O1s, N1s and Ca2p signals of PLA (a,d), MHAP (b,e,g,i) and MACP (c,f,h) electrospun scaffolds; Figure S2: OCN immunohistochemical staining of hWJ-MSCs cultured on PLA scaffolds. Images (a,c) show positive staining for OCN in cells exposed to supplemented DMEM culture medium, while images (b,d) show negative staining. Images (e,g) show positive staining for OCN in cells in TCP exposed to osteogenic differentiation medium, while images (f,h) show negative staining.

Author Contributions: W.C.-A. and I.S.-C. participated extensively in the execution, writing, analysis, and interpretation of the results of the study. E.Y.G.-P. played a crucial role as the co-director of the study and in critically reviewing the final document. A.L.L.-B. assisted in the execution of the in vitro evaluations and in the adjustment of all figures. B.C. was responsible for securing funding for the development of the study and for critically reviewing the final manuscript. All authors have read and agreed to the published version of the manuscript.

Funding: This research was funded by IDCBIS FFDS–CD-0539-2019 and Universidad Pedagógica y Tecnológica de Colombia-UPTC (project code SGI 3476).

Institutional Review Board Statement: Not applicable.

Informed Consent Statement: Not applicable.

Data Availability Statement: The datasets used and/or analyzed during the current study are available from the corresponding author.

Acknowledgments: We are grateful for the support of the Instituto de Investigación en Materiales-IIM of the UNAM, for their collaboration with the characterizations by SEM, EDX, XRD, XPS, FTIR-ATR, DSC, and mechanical tests of the scaffolds.

Conflicts of Interest: The authors declare no conflict of interest. The funders had no role in the design of the study; in the collection, analyses, or interpretation of data; in the writing of the manuscript; or in the decision to publish the results.

References

1. Iaquinta, M.R.; Mazzoni, E.; Bononi, I.; Rotondo, J.C.; Mazziotta, C.; Montesi, M.; Sprio, S.; Tampieri, A.; Tognon, M.; Martini, F. Adult Stem Cells for Bone Regeneration and Repair. *Front. Cell Dev. Biol.* **2019**, *7*, 485383. [CrossRef]
2. Shang, F.; Yu, Y.; Liu, S.; Ming, L.; Zhang, Y.; Zhou, Z.; Zhao, J.; Jin, Y. Advancing Application of Mesenchymal Stem Cell-Based Bone Tissue Regeneration. *Bioact. Mater.* **2021**, *6*, 666–683. [CrossRef]
3. Chandra, P.K.; Soker, S.; Atala, A. Tissue Engineering: Current Status and Future Perspectives. *Princ. Tissue Eng.* **2020**, 1–35. [CrossRef]
4. Bharadwaz, A.; Jayasuriya, A.C. Recent Trends in the Application of Widely Used Natural and Synthetic Polymer Nanocomposites in Bone Tissue Regeneration. *Mater. Sci. Eng. C* **2020**, *110*, 110698. [CrossRef]
5. Collins, M.N.; Ren, G.; Young, K.; Pina, S.; Reis, R.L.; Oliveira, J.M. Scaffold Fabrication Technologies and Structure/Function Properties in Bone Tissue Engineering. *Adv. Funct. Mater.* **2021**, *31*, 2010609. [CrossRef]
6. Fusco, A.; Contaldo, M.; Maleki, H.; Azimi, B.; Ismaeilimoghadam, S.; Danti, S. Poly (Lactic Acid)-Based Electrospun Fibrous Structures for Biomedical Applications. *Appl. Sci.* **2022**, *12*, 3192. [CrossRef]
7. Singhvi, M.S.; Zinjarde, S.S.; Gokhale, D.V. Polylactic Acid: Synthesis and Biomedical Applications. *J. Appl. Microbiol.* **2019**, *127*, 1612–1626. [CrossRef] [PubMed]
8. Zhu, X.; Wang, C.; Bai, H.; Zhang, J.; Wang, Z.; Li, Z.; Zhao, X.; Wang, J.; Liu, H. Functionalization of Biomimetic Mineralized Collagen for Bone Tissue Engineering. *Mater. Today Bio.* **2023**, *20*, 100660. [CrossRef] [PubMed]
9. Edén, M. Structure and Formation of Amorphous Calcium Phosphate and Its Role as Surface Layer of Nanocrystalline Apatite: Implications for Bone Mineralization. *Materialia* **2021**, *17*, 101107. [CrossRef]
10. Eliaz, N.; Metoki, N. Calcium Phosphate Bioceramics: A Review of Their History, Structure, Properties, Coating Technologies and Biomedical Applications. *Materials* **2017**, *10*, 334. [CrossRef]
11. Shaheen, M.Y. Nanocrystalline Hydroxyapatite in Periodontal Bone Regeneration: A Systematic Review. *Saudi Dent. J.* **2022**, *34*, 647–660. [CrossRef]
12. Baino, F.; Fiume, E.; Barberi, J.; Kargozar, S.; Marchi, J.; Massera, J.; Verné, E. Processing Methods for Making Porous Bioactive Glass-Based Scaffolds—A State-of-the-Art Review. *Int. J. Appl. Ceram. Technol.* **2019**, *16*, 1762–1796. [CrossRef]
13. Espitia-Quiroz, L.C.; Fernández-Orjuela, A.L.; Anaya-Sampayo, L.M.; Acosta-Gómez, A.P.; Sequeda-Castañeda, L.G.; Gutiérrez-Prieto, S.J.; Roa-Molina, N.S.; García-Robayo, D.A. Viability and Adhesion of Periodontal Ligament Fibroblasts on a Hydroxyapatite Scaffold Combined with Collagen, Polylactic Acid–Polyglycolic Acid Copolymer and Platelet-Rich Fibrin: A Preclinical Pilot Study. *Dent. J.* **2022**, *10*, 167. [CrossRef] [PubMed]
14. Garkal, A.; Kulkarni, D.; Musale, S.; Mehta, T.; Giram, P. Electrospinning Nanofiber Technology: A Multifaceted Paradigm in Biomedical Applications. *New J. Chem.* **2021**, *45*, 21508–21533. [CrossRef]
15. Zhang, Y.; Zhang, M.; Cheng, D.; Xu, S.; Du, C.; Xie, L.; Zhao, W. Applications of Electrospun Scaffolds with Enlarged Pores in Tissue Engineering. *Biomater. Sci.* **2022**, *10*, 1423–1447. [CrossRef] [PubMed]
16. Liu, Z.; Ramakrishna, S.; Liu, X. Electrospinning and Emerging Healthcare and Medicine Possibilities. *APL Bioeng.* **2020**, *4*, 030901. [CrossRef]
17. Ielo, I.; Calabrese, G.; De Luca, G.; Conoci, S. Recent Advances in Hydroxyapatite-Based Biocomposites for Bone Tissue Regeneration in Orthopedics. *Int. J. Mol. Sci.* **2022**, *23*, 9721. [CrossRef] [PubMed]
18. Capuana, E.; Lopresti, F.; Ceraulo, M.; La Carrubba, V. Poly-l-Lactic Acid (PLLA)-Based Biomaterials for Regenerative Medicine: A Review on Processing and Applications. *Polymers* **2022**, *14*, 1153. [CrossRef]
19. Bernardo, M.P.; da Silva, B.C.R.; Hamouda, A.E.I.; de Toledo, M.A.S.; Schalla, C.; Rütten, S.; Goetzke, R.; Mattoso, L.H.C.; Zenke, M.; Sechi, A. PLA/Hydroxyapatite Scaffolds Exhibit in Vitro Immunological Inertness and Promote Robust Osteogenic Differentiation of Human Mesenchymal Stem Cells without Osteogenic Stimuli. *Sci. Rep.* **2022**, *12*, 2333. [CrossRef]
20. Santhakumar, S.; Oyane, A.; Nakamura, M.; Koga, K.; Miyata, S.; Muratsubaki, K.; Miyaji, H. In Situ Precipitation of Amorphous Calcium Phosphate Nanoparticles within 3D Porous Collagen Sponges for Bone Tissue Engineering. *Mater. Sci. Eng. C* **2020**, *116*, 111194. [CrossRef]
21. Hoeher, A.J.; Mergelsberg, S.T.; Borkiewicz, O.J.; Michel, F.M. Impacts of Initial Ca/P on Amorphous Calcium Phosphate. *Cryst. Growth Des.* **2021**, *21*, 3736–3745. [CrossRef]
22. Bahremandi-Toloue, E.; Mohammadalizadeh, Z.; Mukherjee, S.; Karbasi, S. Incorporation of Inorganic Bioceramics into Electrospun Scaffolds for Tissue Engineering Applications: A Review. *Ceram. Int.* **2022**, *48*, 8803–8837. [CrossRef]
23. Aprile, P.; Letourneur, D.; Simon-Yarza, T. Membranes for Guided Bone Regeneration: A Road from Bench to Bedside. *Adv. Healthc. Mater.* **2020**, *9*, 2000707. [CrossRef]
24. Niu, X.; Liu, Z.; Tian, F.; Chen, S.; Lei, L.; Jiang, T.; Feng, Q.; Fan, Y. Sustained Delivery of Calcium and Orthophosphate Ions from Amorphous Calcium Phosphate and Poly (L-Lactic Acid)-Based Electrospinning Nanofibrous Scaffold. *Sci. Rep.* **2017**, *7*, 45655. [CrossRef] [PubMed]
25. Ma, Z.; Chen, F.; Zhu, Y.-J.; Cui, T.; Liu, X.-Y. Amorphous Calcium Phosphate/Poly (D, L-Lactic Acid) Composite Nanofibers: Electrospinning Preparation and Biomineralization. *J. Colloid Interface Sci.* **2011**, *359*, 371–379. [CrossRef] [PubMed]

26. Zhang, H.; Fu, Q.-W.; Sun, T.-W.; Chen, F.; Qi, C.; Wu, J.; Cai, Z.-Y.; Qian, Q.-R.; Zhu, Y.-J. Amorphous Calcium Phosphate, Hydroxyapatite and Poly (D, L-Lactic Acid) Composite Nanofibers: Electrospinning Preparation, Mineralization and in Vivo Bone Defect Repair. *Colloids Surfaces B Biointerfaces* **2015**, *136*, 27–36. [CrossRef]
27. Wang, Q.; Yang, Q.; Wang, Z.; Tong, H.; Ma, L.; Zhang, Y.; Shan, F.; Meng, Y.; Yuan, Z. Comparative Analysis of Human Mesenchymal Stem Cells from Fetal-Bone Marrow, Adipose Tissue, and Warton's Jelly as Sources of Cell Immunomodulatory Therapy. *Hum. Vaccines Immunother.* **2016**, *12*, 85–96. [CrossRef]
28. Manochantr, S.; U-pratya, Y.; Kheolamai, P.; Rojphisan, S.; Chayosumrit, M.; Tantrawatpan, C.; Supokawej, A.; Issaragrisil, S. Immunosuppressive Properties of Mesenchymal Stromal Cells Derived from Amnion, Placenta, W Harton's Jelly and Umbilical Cord. *Intern. Med. J.* **2013**, *43*, 430–439. [CrossRef]
29. Liu, S.; Jia, Y.; Yuan, M.; Guo, W.; Huang, J.; Zhao, B.; Peng, J.; Xu, W.; Lu, S.; Guo, Q. Repair of Osteochondral Defects Using Human Umbilical Cord Wharton's Jelly-Derived Mesenchymal Stem Cells in a Rabbit Model. *Biomed Res. Int.* **2017**, *2017*. [CrossRef]
30. Abidi, S.S.A.; Murtaza, Q. Synthesis and Characterization of Nano-Hydroxyapatite Powder Using Wet Chemical Precipitation Reaction. *J. Mater. Sci. Technol.* **2014**, *30*, 307–310. [CrossRef]
31. Akkouch, A.; Zhang, Z.; Rouabhia, M. A Novel Collagen/Hydroxyapatite/Poly(Lactide-Co-ε-Caprolactone) Biodegradable and Bioactive 3D Porous Scaffold for Bone Regeneration. *J. Biomed. Mater. Res. A* **2011**, *96*, 693–704. [CrossRef] [PubMed]
32. Gómez-Pachón, E.; Vera-Graziano, R.; Montiel, R.; Cardenas-Aguazaco, W.; Ochica, A.F.; Gómez-Pachón, E.; Vera-Graziano, R.; Montiel, R.; Cardenas-Aguazaco, W.; Ochica, A.F. Effects of Heat Treatment and the Method of Collection on the Crystal Structure of the Poly Lactic Acid Electrospinned Nanofibers. *Ingeniare. Rev. Chil. Ing.* **2019**, *27*, 586–599. [CrossRef]
33. *ISO 10993-5:2009*; Biological Evaluation of Medical Devices—Part 5: Tests for in Vitro Cytotoxicity. ISO: Geneva, Switzerland. Available online: https://www.iso.org/standard/36406.html (accessed on 2 October 2023).
34. Miguez, M.; Sabarots, M.G.; Cid, M.P.; Salvatierra, N.A.; Comín, R. Fabrication and Characterization of Gelatin/Calcium Phosphate Electrospun Composite Scaffold for Bone Tissue Engineering. *Fibers Polym.* **2022**, *23*, 1915–1923. [CrossRef]
35. Lee, A.; Jain, A. Measuring Cell-Viability by Resazurin (Alamarblue®) Assay Using Photopette® Cell. Appl. note, Tip Biosyst. Cell Viability Life Sci. 2017. Available online: http//tipbiosystems.com/tbs/wpcontent/uploads/2017/06/AN016-Cell-Viability-using-Resazurin-Dye_2017_05_29.pdf (accessed on 15 May 2020).
36. Lopresti, F.; Carfì Pavia, F.; Vitrano, I.; Kersaudy-Kerhoas, M.; Brucato, V.; La Carrubba, V. Effect of Hydroxyapatite Concentration and Size on Morpho-Mechanical Properties of PLA-Based Randomly Oriented and Aligned Electrospun Nanofibrous Mats. *J. Mech. Behav. Biomed. Mater.* **2020**, *101*, 103449. [CrossRef]
37. Munir, M.U.; Salman, S.; Ihsan, A.; Elsaman, T. Synthesis, Characterization, Functionalization and Bio-Applications of Hydroxyapatite Nanomaterials: An Overview. *Int. J. Nanomed.* **2022**, *17*, 1903. [CrossRef]
38. Padmanabhan, V.P.; Kulandaivelu, R.; Panneer, D.S.; Vivekananthan, S.; Sagadevan, S.; Lett, J.A. Microwave Synthesis of Hydroxyapatite Encumbered with Ascorbic Acid Intended for Drug Leaching Studies. *Mater. Res. Innov.* **2019**, *24*, 171–178. [CrossRef]
39. Xidaki, D.; Agrafioti, P.; Diomatari, D.; Kaminari, A.; Tsalavoutas-Psarras, E.; Alexiou, P.; Psycharis, V.; Tsilibary, E.C.; Silvestros, S.; Sagnou, M. Synthesis of Hydroxyapatite, β-Tricalcium Phosphate and Biphasic Calcium Phosphate Particles to Act as Local Delivery Carriers of Curcumin: Loading, Release and in Vitro Studies. *Materials* **2018**, *11*, 595. [CrossRef]
40. Xie, Q.; Guo, G.; Lu, W.; Sun, C.; Zhou, J.; Zheng, Y.; Shan, G.; Bao, Y.; Pan, P. Polymorphic Homocrystallization and Phase Behavior of High-Molecular-Weight Poly (L-Lactic Acid)/Poly (D-Lactic Acid) Racemic Mixture with Intentionally Enhanced Stereocomplexation Ability via Miscible Blending. *Polymer* **2020**, *201*, 122597. [CrossRef]
41. Gieroba, B.; Przekora, A.; Kalisz, G.; Kazimierczak, P.; Song, C.L.; Wojcik, M.; Ginalska, G.; Kazarian, S.G.; Sroka-Bartnicka, A. Collagen Maturity and Mineralization in Mesenchymal Stem Cells Cultured on the Hydroxyapatite-Based Bone Scaffold Analyzed by ATR-FTIR Spectroscopic Imaging. *Mater. Sci. Eng. C* **2021**, *119*, 111634. [CrossRef]
42. Apalangya, V.A.; Rangari, V.K.; Tiimob, B.J.; Jeelani, S.; Samuel, T. Eggshell Based Nano-Engineered Hydroxyapatite and Poly(Lactic) Acid Electrospun Fibers as Potential Tissue Scaffold. *Int. J. Biomater.* **2019**, *2019*. [CrossRef] [PubMed]
43. Scarano, A.; Lorusso, F.; Orsini, T.; Morra, M.; Iviglia, G.; Valbonetti, L. Biomimetic Surfaces Coated with Covalently Immobilized Collagen Type I: An X-Ray Photoelectron Spectroscopy, Atomic Force Microscopy, Micro-CT and Histomorphometrical Study in Rabbits. *Int. J. Mol. Sci.* **2019**, *20*, 724. [CrossRef] [PubMed]
44. Deng, L.; Li, Y.; Zhang, A.; Zhang, H. Characterization and Physical Properties of Electrospun Gelatin Nanofibrous Films by Incorporation of Nano-Hydroxyapatite. *Food Hydrocoll.* **2020**, *103*, 105640. [CrossRef]
45. Demri, B.; Muster, D. XPS Study of Some Calcium Compounds. *J. Mater. Process. Technol.* **1995**, *55*, 311–314. [CrossRef]
46. Murphy, B.; Baez, J.; Morris, M.A. Characterising Hydroxyapatite Deposited from Solution onto Novel Substrates: Growth Mechanism and Physical Properties. *Nanomaterials* **2023**, *13*, 2483. [CrossRef] [PubMed]
47. Leonés, A.; Peponi, L.; Lieblich, M.; Benavente, R.; Fiori, S. In Vitro Degradation of Plasticized PLA Electrospun Fiber Mats: Morphological, Thermal and Crystalline Evolution. *Polymers* **2020**, *12*, 2975. [CrossRef]
48. Vidović, E.; Faraguna, F.; Jukić, A. Influence of Inorganic Fillers on PLA Crystallinity and Thermal Properties. *J. Therm. Anal. Calorim.* **2017**, *127*, 371–380. [CrossRef]

49. Seraji, A.A.; Goharpey, F.; Khademzadeh Yeganeh, J. Highly Crystallized and Tough Polylactic Acid through Addition of Surface Modified Cellulose Nanocrystals. *J. Appl. Polym. Sci.* **2022**, *139*, e52871. [CrossRef]
50. Dao, T.T.-T.; Nguyen, C.T.-H.; Vu, N.B.; Le, H.T.-N.; Nguyen, P.D.-N.; Van Pham, P. Evaluation of Proliferation and Osteogenic Differentiation of Human Umbilical Cord-Derived Mesenchymal Stem Cells in Porous Scaffolds. In *Proceedings of the Tissue Engineering and Regenerative Medicine*; Springer: Berlin/Heidelberg, Germany, 2019; pp. 207–220. [CrossRef]
51. Ren, X.; Zhao, M.; Lash, B.; Martino, M.M.; Julier, Z. Growth Factor Engineering Strategies for Regenerative Medicine Applications. *Front. Bioeng. Biotechnol.* **2020**, *7*, 469. [CrossRef]
52. Jenkins, T.L.; Little, D. Synthetic Scaffolds for Musculoskeletal Tissue Engineering: Cellular Responses to Fiber Parameters. *NPJ Regen. Med.* **2019**, *4*, 15. [CrossRef]
53. Posa, F.; Di Benedetto, A.; Ravagnan, G.; Cavalcanti-Adam, E.A.; Lo Muzio, L.; Percoco, G.; Mori, G. Bioengineering Bone Tissue with 3D Printed Scaffolds in the Presence of Oligostilbenes. *Materials* **2020**, *13*, 4471. [CrossRef]
54. Lv, Y.; Sang, X.; Tian, Z.; Jiang, S.; Li, C.; Guo, Q.; Wang, C.; Hu, P.; Liu, Y. Electrospun Hydroxyapatite Loaded L-Polylactic Acid Aligned Nanofibrous Membrane Patch for Rotator Cuff Repair. *Int. J. Biol. Macromol.* **2022**, *217*, 180–187. [CrossRef]
55. Sanosh, K.P.; Chu, M.C.; Balakrishnan, A.; Kim, T.N.; Cho, S.J. Preparation and Characterization of Nano-Hydroxyapatite Powder Using Sol-Gel Technique. *Bull. Mater. Sci.* **2009**, *32*, 465–470. [CrossRef]
56. Alrebaish, A.S.; Wilson, O.C., Jr. Mesocrystal Aggregation of Biological Apatite Nanocrystals. *Med. Devices Sens.* **2021**, *4*, e10155. [CrossRef]
57. Boukha, Z.; Yeste, M.P.; Cauqui, M.Á.; Gonzalez-Velasco, J.R. Influence of Ca/P Ratio on the Catalytic Performance of Ni/Hydroxyapatite Samples in Dry Reforming of Methane. *Appl. Catal. A Gen.* **2019**, *580*, 34–45. [CrossRef]
58. Bakan, F. A Systematic Study of the Effect of PH on the Initialization of Ca-Deficient Hydroxyapatite to β-TCP Nanoparticles. *Materials* **2019**, *12*, 354. [CrossRef] [PubMed]
59. Vecstaudza, J.; Locs, J. Novel Preparation Route of Stable Amorphous Calcium Phosphate Nanoparticles with High Specific Surface Area. *J. Alloys Compd.* **2017**, *700*, 215–222. [CrossRef]
60. Dorozhkin, S. V Calcium Orthophosphates in Nature, Biology and Medicine. *Materials* **2009**, *2*, 399–498. [CrossRef]
61. Lotsari, A.; Rajasekharan, A.K.; Halvarsson, M.; Andersson, M. Transformation of Amorphous Calcium Phosphate to Bone-like Apatite. *Nat. Commun.* **2018**, *9*, 4170. [CrossRef]
62. Barbosa, F.; Ferreira, F.C.; Silva, J.C. Piezoelectric Electrospun Fibrous Scaffolds for Bone, Articular Cartilage and Osteochondral Tissue Engineering. *Int. J. Mol. Sci.* **2022**, *23*, 2907. [CrossRef]
63. Flores-Rojas, G.G.; Gómez-Lazaro, B.; López-Saucedo, F.; Vera-Graziano, R.; Bucio, E.; Mendizábal, E. Electrospun Scaffolds for Tissue Engineering: A Review. *Macromol* **2023**, *3*, 524–553. [CrossRef]
64. Chen, W.; Zhong, C.; Li, S.; Wen, D.; Zhou, D.; Shao, J.; Chen, S.; Hou, H.; Xiang, S. The Crystallization Behavior of Poly (D-Lactic Acid)/Poly (L-Lactic Acid) Asymmetric Blends: Effect of Morphology of Stereocomplex Crystals on the Formation of Homochiral Crystals. *J. Polym. Environ.* **2023**, 1–12. [CrossRef]
65. Georgiopoulos, P.; Christopoulos, A.; Koutsoumpis, S.; Kontou, E. The Effect of Surface Treatment on the Performance of Flax/Biodegradable Composites. *Compos. Part B Eng.* **2016**, *106*, 88–98. [CrossRef]
66. Akindoyo, J.O.; Beg, M.D.H.; Ghazali, S.; Heim, H.P.; Feldmann, M. Impact Modified PLA-Hydroxyapatite Composites–Thermo-Mechanical Properties. *Compos. Part A Appl. Sci. Manuf.* **2018**, *107*, 326–333. [CrossRef]
67. Cifuentes, S.C.; Lieblich, M.; Saldaña, L.; González-Carrasco, J.L.; Benavente, R. In Vitro Degradation of Biodegradable Polylactic Acid/Mg Composites: Influence of Nature and Crystalline Degree of the Polymeric Matrix. *Materialia* **2019**, *6*, 100270. [CrossRef]
68. Leonés, A.; Salaris, V.; Mujica-Garcia, A.; Arrieta, M.P.; Lopez, D.; Lieblich, M.; Kenny, J.M.; Peponi, L. PLA Electrospun Fibers Reinforced with Organic and Inorganic Nanoparticles: A Comparative Study. *Molecules* **2021**, *26*, 4925. [CrossRef] [PubMed]
69. Moncayo Donoso, M.Á. Desarrollo de Prototipos de Soportes Tridimensionales a Base de Colágeno Tipo I e Hidroxiapatita Para Regeneración Ósea. Ph.D. Thesis, Universidad de Málaga, Málaga, Spain, 2022. Available online: https://repositorio.unal.edu.co/handle/unal/77380 (accessed on 2 October 2023).
70. Jeong, D.; Jang, J.; Lee, D.Y. Electrospun Poly (D, L-Lactic Acid)/Gelatin Membrane Using Green Solvent for Absorbable Periodontal Tissue Regeneration. *J. Korean Cryst. Growth Cryst. Technol* **2023**, *33*, 104–109.
71. Chowdhury, S.R.; Mh Busra, M.F.; Lokanathan, Y.; Ng, M.H.; Law, J.X.; Cletus, U.C.; Binti Haji Idrus, R. Collagen Type I: A Versatile Biomaterial. *Adv. Exp. Med. Biol.* **2018**, *1077*, 389–414. [CrossRef]
72. Rico-Llanos, G.A.; Borrego-González, S.; Moncayo-Donoso, M.; Becerra, J.; Visser, R. Collagen Type I Biomaterials as Scaffolds for Bone Tissue Engineering. *Polymers* **2021**, *13*, 599. [CrossRef]
73. Notodihardjo, S.C.; Morimoto, N.; Kakudo, N.; Mitsui, T.; Le, T.M.; Tabata, Y.; Kusumoto, K. Comparison of the Efficacy of Cryopreserved Human Platelet Lysate and Refrigerated Lyophilized Human Platelet Lysate for Wound Healing. *Regen. Ther.* **2019**, *10*, 1–9. [CrossRef]
74. Choi, H.; Jeong, B.C.; Hur, S.W.; Kim, J.W.; Lee, K.B.; Koh, J.T. The Angiopoietin-1 Variant COMP-Ang1 Enhances BMP2-Induced Bone Regeneration with Recruiting Pericytes in Critical Sized Calvarial Defects. *PLoS ONE* **2015**, *10*, e0140502. [CrossRef]
75. Toosi, S.; Behravan, J. Osteogenesis and Bone Remodeling: A Focus on Growth Factors and Bioactive Peptides. *Biofactors* **2020**, *46*, 326–340. [CrossRef] [PubMed]

76. Wang, F.; Cai, X.; Shen, Y.; Meng, L. Cell–Scaffold Interactions in Tissue Engineering for Oral and Craniofacial Reconstruction. *Bioact. Mater.* **2023**, *23*, 16–44. [CrossRef] [PubMed]
77. Carvalho, M.S.; Cabral, J.M.S.; da Silva, C.L.; Vashishth, D. Synergistic Effect of Extracellularly Supplemented Osteopontin and Osteocalcin on Stem Cell Proliferation, Osteogenic Differentiation, and Angiogenic Properties. *J. Cell. Biochem.* **2019**, *120*, 6555–6569. [CrossRef] [PubMed]

Disclaimer/Publisher's Note: The statements, opinions and data contained in all publications are solely those of the individual author(s) and contributor(s) and not of MDPI and/or the editor(s). MDPI and/or the editor(s) disclaim responsibility for any injury to people or property resulting from any ideas, methods, instructions or products referred to in the content.

Regenerative Therapy 26 (2024) 145–160

Contents lists available at ScienceDirect

Regenerative Therapy

journal homepage: http://www.elsevier.com/locate/reth

Review

Exploring calcium-free alternatives in endochondral bone repair tested on *In vivo* trials - A review

William Cárdenas-Aguazaco, Adriana Lorena Lara-Bertrand, Leonardo Prieto-Abello, Nicolás Barreto-López, Bernardo Camacho, Ingrid Silva-Cote*

Unidad de Ingeniería Tisular, Instituto Distrital de Ciencia, Biotecnología e Innovación en Salud-IDCBIS, Colombia

ARTICLE INFO

Article history:
Received 28 March 2024
Received in revised form
10 May 2024
Accepted 26 May 2024

Keywords:
Bone defects
Endochondral ossification
Regeneration
Biomaterials
Cells
Calcium-free alternatives

ABSTRACT

Bone repair via endochondral ossification is a complex process for the critical size reparation of bone defects. Tissue engineering strategies are being developed as alternative treatments to autografts or allografts. Most approaches to bone regeneration involve the use of calcium composites. However, exploring calcium-free alternatives in endochondral bone repair has emerged as a promising way to contribute to bone healing. By analyzing researches from the last ten years, this review identifies the potential benefits of such alternatives compared to traditional calcium-based approaches. Understanding the impact of calcium-free alternatives on endochondral bone repair can have profound implications for orthopedic and regenerative medicine. This review evaluates the efficacy of calcium-free alternatives in endochondral bone repair through *in vivo* trials. The findings may guide future research to develop innovative strategies to improve endochondral bone repair without relying on calcium. Exploring alternative approaches may lead to the discovery of novel therapies that improve bone healing outcomes.
© 2024, The Japanese Society for Regenerative Medicine. Production and hosting by Elsevier B.V. This is an open access article under the CC BY-NC-ND license (http://creativecommons.org/licenses/by-nc-nd/4.0/).

Contents

1. Introduction 146
1.1. Natural materials 146
1.2. Synthetic materials 148
1.2.1. Polymers 148
1.2.2. Metallic scaffolds 153
1.3. Cells and cellular scaffolds 153
1.3.1. Cell approaches 153
1.3.2. Cartilaginous templates 154
1.4. Mixed scaffolds and other treatments 156

Abbreviations: BTE, Bone Tissue Engineering; EO, Endochondral ossification; TCP, Tricalcium phosphate; HAP, Hydroxyapatite; ACP, amorphous calcium phosphate; OCP, Octacalcium phosphate; DCBM, Decellularized Cancellous Bone Matrix; ASC, Adipose Stromal Cells; BMP-6, Bone Morphogenetic Protein 6; BMP-2, Bone Morphogenetic Protein 2; SSC, Skeletal Stromal Cells; VEGF, Vascular Endothelial Growth Factor; SAA, Salvianic acid; HA, Hyaluronic acid; GAG, Glycosaminoglycans; DBM, Decellularized Bone Matrix; EDC, 1-ethyl-3-carbodiimide hydrochloride; NHS, N-Hydrosuccinimide; bFGF, Basic Fibroblast Growth Factor; PCL, Poly(ε-caprolactone); PEG, Poly-ethylene glycol; PGA, Poly-glycolic acid; MMP, Metalloproteinases; PGS, poly(glycerol sebacate); PLLA, Poly-L-Lactic acid; MSCs, Mesenchymal stromal cells; BMSCs, Bone marrow stromal cells; hBMSCs, human Bone marrow stromal cells; rBMSCs, rat Bone marrow stromal cells; HUVECs, Human umbilical cord vein endothelial cells; Ad-MSCs, Exogenous adipose-derived mesenchymal stem cells; hOAs, human osteoarthritic articular chondrocytes; PDCs, human periosteum-derived cells; iPSCs, human pluripotent stem cells; MAG, Mangiferin; LLP2A-Ale, LLP2A alendronate; HyC, hypertrophic cartilage; hHyC-ECM, Devitalized human hypertrophic cartilage extracellular matrix; PDCM, Particulate decellularized cartilage matrix; PRP, Platelet-rich plasma; Vac-OS, Vacuum-assisted osmotic shock; EBR, Endochondral bone regeneration; PTHrP, hap-loinsufficiency of endogenous parathyroid hormone-related peptide; MEW, Melt Electrowriting.

* Corresponding author. Carrera 32 # 12-81, Secretaria Distrital de Salud, Bogotá, Colombia.
E-mail addresses: wcardenas@idcbis.org.co (W. Cárdenas-Aguazaco), alara@idcbis.org.co (A.L. Lara-Bertrand), lprieto@idcbis.org.co (L. Prieto-Abello), nbarreto@idcbis.org.co (N. Barreto-López), bacamacho@idcbis.org.co (B. Camacho), izsilva@idcbis.org.co (I. Silva-Cote).
Peer review under responsibility of the Japanese Society for Regenerative Medicine.

https://doi.org/10.1016/j.reth.2024.05.017
2352-3204/© 2024, The Japanese Society for Regenerative Medicine. Production and hosting by Elsevier B.V. This is an open access article under the CC BY-NC-ND license (http://creativecommons.org/licenses/by-nc-nd/4.0/).

2. Conclusions and perspectives 157
Author contributions 157
Declaration of competing interest 158
Acknowledgements 158
References 158

1. Introduction

Critical-size bone defects resulting from trauma, congenital disorders, and tissue resection require more than two million bone grafts annually [1]. These defects exceed the self-healing capacity of natural bone and can significantly affect a patient's appearance and musculoskeletal function [2]. Autogenous bone grafting is the clinical "gold standard" due to its exceptional immunocompatibility and inherent osteoinductive, osteoconductive, and osteogenic properties. However, it has limitations such as donor site morbidity, limited graft availability, and decreased regenerative potential with donor age [3]. Allografting is less common due to the risk of immune rejection and disease transmission [4], while xenografting raises concerns such as infection and rejection [5]. In addition, these treatments require multiple surgeries, bone fixation devices, and slow regeneration processes. This can sometimes lead to improper graft integration, hindering healing [6].

As an alternative, bone tissue engineering (BTE) strategies have transformed bone healing and regeneration treatments. BTE is an interdisciplinary field that combines engineering and life science principles to develop bioartificial bone tissue to repair bone defects caused by trauma or congenital disorders and to restore, maintain, or improve tissue function [7]. Strategies developed in BTE utilize biomaterials, extracellular matrices, osteogenic cells, growth factors, and gene therapy [8]. Various biomaterials, including metals, natural or synthetic polymers, and ceramics, including calcium compounds such as tricalcium phosphate (TCP), hydroxyapatite (HAP), amorphous calcium phosphate (ACP), and octacalcium phosphate (OCP), have shown promise in bone repair applications [8–12]. In addition, the integration of natural and synthetic materials with cell therapies and bioactive molecules has produced remarkable results in large bone defect models through chondrocyte hypertrophy, cartilage matrix template, mineral deposition, and bone formation [13].

Historically, BTE approaches have focused on scaffold design using calcium compounds as the primary osteoinductive composite, a topic that has been extensively researched and reviewed [13–15]. However, materials other than calcium-based composites have gradually become the focus of attention in bone tissue engineering constructs. Research on non-calcium-based composites has led to the development of innovative scaffold materials and fabrication techniques that may improve outcomes in BTE [16]. The use of non-calcium-based composites reduces the risk of unwanted calcification or mineralization in surrounding tissues, a common problem with calcium-based materials. In addition, non-calcium composites may offer better biocompatibility for certain applications, which could reduce immune responses or adverse reactions in the body [16]. However, non-calcium-based composites also have limitations. These composites may not have the osteoconductive properties of calcium-based materials, such as hydroxyapatite, which are essential for promoting bone growth and integration. In addition, different non-calcium-based composites may have different degradation rates in the body, potentially compromising the overall structural integrity and longevity of the scaffold [17]. The interactions between non-calcium-based composites and host tissues may also be more complex and less predictable than those with calcium-based materials, requiring additional research and optimization for successful integration [18].

This review analyzes and presents new approaches developed in the last decade to repair severe bone injuries without relying on calcium composites in the context of endochondral bone repair. The review explores non-calcium-based composites prepared with natural and synthetic polymers, metals, bioactive molecules, growth factors, and stem cells as potential substitutes for traditional calcium-based composites in bone tissue engineering. This review aims to assess the efficacy and potential impact of non-calcium alternatives on bone regeneration by analyzing the current research landscape and the results of these innovative approaches. It will also provide insight into the future potential of these emerging strategies and their impact on bone tissue engineering. Fig. 1 summarizes the major groups of materials used in the fabrication of non-calcium based scaffolds or constructs for endochondral ossification research that have been evaluated *in vivo*.

1.1. Natural materials

Natural materials have emerged as promising alternatives in tissue engineering for repairing large bone defects, due to inherent properties such as high biocompatibility, close resemblance to

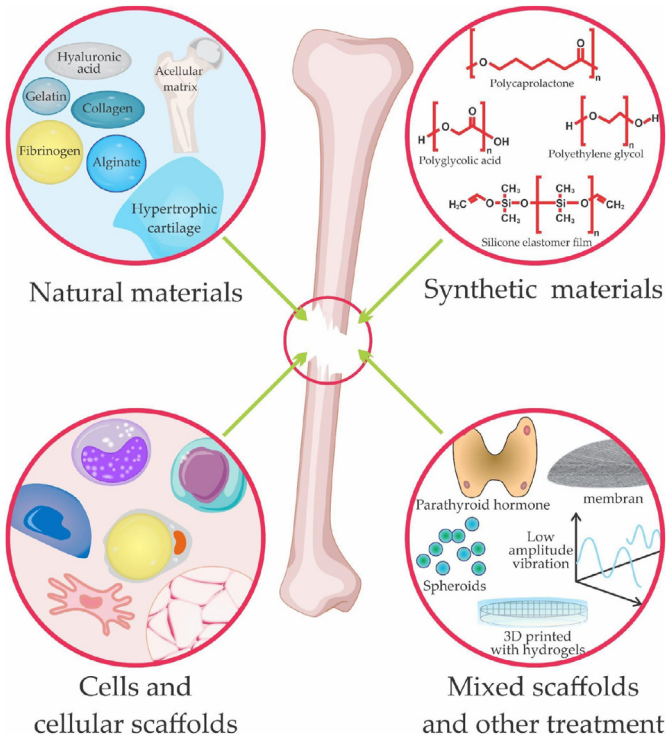


Fig. 1. Strategies used and evaluated *in vitro* and *in vivo* for bone repair via endochondral ossification without calcium composites.

natural tissues, and gradual degradation over time. Gelatin, fibrinogen, collagen, and alginate, as well as bone and cartilage from autologous, allogeneic, or xenogeneic sources, are used to create hydrogels or scaffolds for bone tissue engineering and EO promotion that do not contain calcium compounds. These materials and methods have been tested in relevant environments with promising results; some of which are shown in Fig. 2.

Some examples of the scaffolds mentioned that have been tested include ground cortical bone powder with bone marrow stem cells (BMSCs) in a fibrinogen gel [22], or constructs containing MSCs micropellets and fibrin that have been shown to stimulate bone formation in injectable bone graft substitutes [23], and cancellous bone that has been decellularized and partially demineralized [24] in rabbit femur and murine models. These results showed decreased fibrotic tissue in the affected area, new trabeculae formation, vascularization, and significant bone formation or calcified cartilage due to EO [22,24].

Collagen has been extensively studied for its role in bone repair because it is a major component of cartilage and the bone's extracellular matrix [25,26]. As a result, collagen has been tested with different geometric structures and cell types, including adipose stromal cells (ASCs), skeletal stromal cells (SSC's), and mesenchymal stromal cells (MSCs), to take advantage of order to capitalize on their combined properties for EO-mediated bone repair. Collagen with geometric structures based on oriented channels demonstrated greater potential for bone repair by EO than random collagen structures that did not contain growth factors or cells within the scaffold [27]. Similarly, ASCs and collagen formed a cartilaginous matrix *in vitro* that was then implanted subcutaneously in mice, resulting in a hypertrophic cartilage matrix via endochondral ossification, with potential use in long bone repair [28]. Collagen and SSC's have also been evaluated for their ability to form bone via EO in an ectopic approach in mice, showing great potential for bone repair [29]. The MSCs approach involves chondrogenic differentiation within the collagen scaffold, consisting in the combination of BMSC's suspension with collagen type I and a reconstitution buffer, subsequently seeded with chondrogenic differentiation medium for 3 weeks and hypertrophic differentiation medium for another 2 weeks for posterior subcutaneous implantation. This method induces endochondral ossification in mice, resulting in the formation of blood vessels and the deposition of various types of collagens, including types I, II, and X (Fig. 2a) [19].

Collagen-based scaffolds loaded with bioactive molecules or growth factors are a promising approach to develop effective bone tissue engineering techniques [30]. Bioactive molecules such as angiostatin [31], bone morphogenetic protein 2 (BMP-2), vascular endothelial growth factor (VEGF) [32], oxysterol [33], and salvianic acid [34] have been shown to promote EO alongside collagen sponges and matrices with unidirectional architecture, decrease the expression of inflammatory and angiogenic genes, and increase the expression of EO markers, thereby accelerating the transition from cartilage to bone. These collagen scaffolds containing bioactive molecules have been tested in mice, rats and rabbits.

Gelatin, a collagen derivative, is biodegradable and biocompatible, with lower antigenicity than collagen, making it an ideal material for bone repair [35]. In terms of EO, gelatin crosslinked

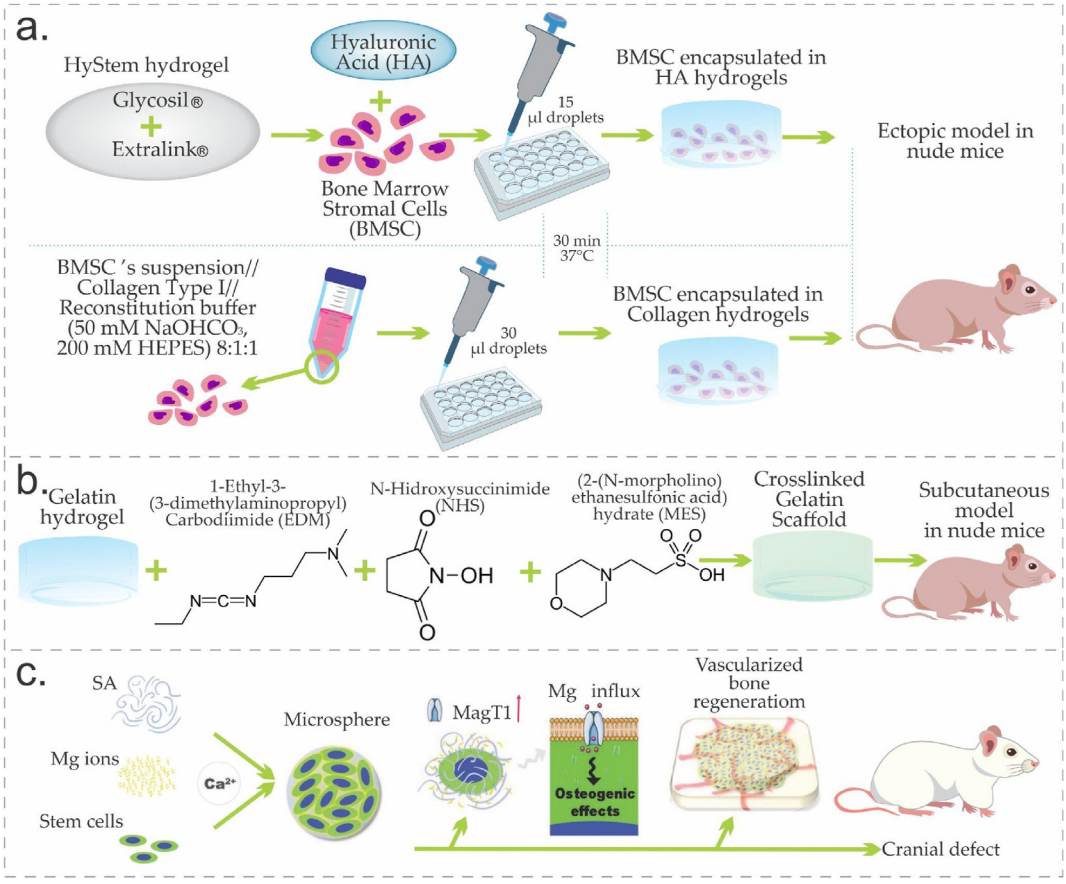


Fig. 2. Some strategies using natural materials for bone repair by EO in *in vivo* models. a. Fabrication method of hyaluronic acid (HA) and collagen hydrogels with encapsulated BMSCs to promote endochondral ossification (adapted from Ref. [19]). b. Materials needed to obtain cross-linked gelatin scaffold by carbodiimide chemistry (EDC and NHS) with a reconstitution buffer (MES). (Adapted from Ref. [20]). c. Schematic construction of the Mg-enriched 3D culture system promoting MagT1 expression for bone regeneration and evaluation in rat cranial defects. (adapted from Ref. [21]).

with 1-ethyl-3-carbodiimide hydrochloride (EDC) and N-hydroxysuccinimide (NHS) via carbodiimide chemistry produced varying degrees of stiffness and allowed for chondrogenic and osteogenic differentiation of mouse mesenchymal stem cell line, C3H10T1/2, and pre-osteoblastic MC3T3-E1 cells over time *in vitro*. For *in vivo* approach, BMSC's were seeded on these gelatin scaffolds, resulting in increased stem cell-mediated trabecular bone formation in stiffer scaffolds tested in C57BJL/6 mice (Fig. 2b) [20].

Gelatin, like collagen, can be loaded with various growth factors and bioactive molecules that enhance bone repair capacity via endochondral ossification. Gelatin hydrogels loaded with basic fibroblast growth factor (bFGF) significantly improved bone healing in a femoral fracture model in C57BL/6 mice [36]. BMP-2 and transforming growth factor beta 1 (TGF-β1) promote bone and blood vessel formation [37], induce EO by accelerating bone healing and remodeling [38], and stimulate BMSCs to chondrogenic differentiation [39]. In addition, BMP-2 combined with chondroitin sulfate in a gelatin matrix improves the regenerative potential of EO in bone healing in mice [40].

Alginate is another versatile biomaterial that facilitates cell encapsulation and growth factor delivery, making it a promising candidate for guiding endochondral bone formation [41]. This material allows for the incorporation of a variety of substances such as peptides, kartogenin, magnesium, or cells to enhance EO. For example, peptides such as RGD (arginine, glycine, and aspartic acid) and QK (VEGF mimicking peptide) in combination with kartogenin were found to play a key role in regulating cell behavior for osteochondral defect repair [42]. Magnesium-enriched alginate microspheres promoted vascularized bone growth by mimicking key developmental processes by upregulating the expression of magnesium transporter-1 (MagT1), a selective magnesium (Mg) transporter, in a mouse embryo model and enhance formation of vascularized bone in cranial defects in rats (Fig. 2c) [21]. Alternatively, ASC-derived alginate constructs demonstrated superior bone-forming capacity, chondrogenesis, and vascularization in mice after four weeks of chondrogenic induction and eight weeks of subcutaneous implantation [43].

Biomaterials have been tested for their ability to promote EO after ectopic implantation in nude mice. For example, hyaluronic acid (HA) (HyStem hydrogel) loaded with Bone Marrow mesenchymal stromal cells (BMSCs) has been shown to exhibit complete integration in all biomodels evaluated, producing bone with vascularization and marrow development between fused grafts in ectopic model in nude mice (Fig. 2a) [19].

Another novel material for bone repair by EO is Adiscaf, a fractionated human adipose tissue designed to differentiate adipose stromal cells (ASCs) and facilitate cartilage formation. It contains glycosaminoglycans (GAGs) and type II collagen, enabling the potential for bone tissue formation by EO in an ectopic approach in nude mice [44] in the treatment of long bone defects in nude rats [45,46]. Adiscaf has shown higher GAG production, superior bone formation and vascularization than decellularized bone matrices (DBM).

Using natural materials in bone tissue engineering for repair by EO without using calcium compounds is an excellent way to develop new technologies for repairing long bone defects. However, it is important to note that these materials need to be functionalized and modified to achieve better mechanical behavior and properties that contribute to bone vascularization, formation, and remodeling. A summary of different fabrication methods and *in vivo* evaluations is presented in Table 1.

1.2. Synthetic materials

Synthetic materials have emerged as innovative solutions in orthopedics and bone repair, offering promising alternatives to natural materials. Synthetic materials used in bone repair can be divided into metal materials, polymer materials, and composite materials. Synthetic polymers and metallic biomaterials combined with bioactive molecules are novel strategies for bone scaffold fabrication and/or advanced therapy design. In addition, synthetic materials overcome several limitations, including the availability of natural materials and immunological reactions. Likewise, synthetic scaffolds prepared by various techniques such as electrospinning, 3D printing, and hydrogels have osteoinductive and osteoconductive properties and superior physical and mechanical properties that resemble native bone. In addition, incorporating bioactive molecules induces strategic modifications that enhance physical, chemical, and biological properties to direct site-specific tissue formation while maintaining biomimetic architectures. These modified structures have the potential to support tissue healing and regeneration processes and promote faster and more effective recovery. Fig. 3 offers insight into the process of design, fabrication, and *in vitro* and *in vivo* testing of diverse synthetic materials, using techniques such as 3D printing, hydrogel design, and 3D melting electrospinning as alternatives to bone tissue engineering strategies for critical defects without use of calcium compounds. Different designs that have been tested provide a similar native architecture, contributing to an optimal environment for bone healing and regeneration. These materials, coupled with cell therapy strategies and/or growth factors that have been incorporated, have shown outstanding results in critical-sized bone defect healing.

1.2.1. Polymers

Polymeric materials offer novel solutions for bone tissue engineering, particularly for the repair of critical bone defects by endochondral ossification (EO). These materials exhibit high biocompatibility and gradual degradation, which are essential for successful bone repair. A variety of compounds such as polycaprolactone (PCL), polylactic acid (PLA), poly(L-lactide-co-epsilon-caprolactone) (poly(LA-co-CL)), polyglycolic acid (PGA), and polyethylene glycol (PEG) have been used to obtain fibrous scaffolds and hydrogels that have been fine-tuned and tested in relevant environments for bone tissue engineering applications. Table 2 summarizes the strategies using these polymers and their results in bone tissue engineering. This section explores the role of polymers in advancing bone regeneration and highlights their potential to address critical challenges in bone defect repair.

Polycaprolactone (PCL) is a widely studied polyester in many tissue engineering applications. This polymer has been extensively used to fabricate electrospun PCL nanofiber scaffolds that could mimic the fibrous microarchitecture of bone extracellular matrix; however, they are limited by their mechanical properties. In this sense, porosity optimization and enhanced mechanical properties have been tested and shown to be successful approaches as flexible 3D scaffolds that support chondrogenic differentiation of stem cells and promote endochondral bone formation in long bone defects (Fig. 3a) [47,50].

Accordingly, PCL and its copolymers have been used to develop new scaffolds through polymer casting, 3D printing, and hydrogel-like structures as alternatives for bone-critical defects. For example, polymer casting of poly(L-lactide-co-epsilon-caprolactone) (poly(LA-co-CL)) into a cylindrical architecture has been reported to be a more effective method of inducing endochondral ossification in polymeric bone scaffolds, thereby improving the healing of bone-critical femoral defects in 12-week-old rat models. Similarly, organized 3D architecture has been achieved through additive manufacturing. 3D-printed cylindrical fibrin PCL scaffolds were designed to support mesenchymal cell adhesion and promote chondrogenic or hypertrophic differentiation, thereby achieving

Table 1
Strategies using natural materials evaluated *in vivo*.

Material	Loading or complement	Fabrication	*In vivo* model	Key findings	Ref
Fibrinogen gel	Cortical bone powder and Bone marrow stromal cells (BMSC's)	Cryoprecipitation for fibrinogen gel and BMSC's differentiated osteogenic lineage.	Femur defects in rabbits	Osteogenic BMSCs, combined with the natural scaffold, promoted bone maturity and decreased fibrosis.	[22]
	Mesenchymal Stromal Cells (MSC's)	Crosslinking of thrombin and fibrinogen loaded with MSC's	Ectopic model in nude mice	Micropellet-fibrin-MSC's constructs, with a shorter *in vitro* priming time, showed comparable bone formation to standard MSC's pellets *in vivo*.	[23]
Decellularized and demineralized cancellous bone (DCBM)	N/A	Decellularization of cancellous bone and demineralization by ultrasound	4 mm defect in medial femoral epicondyles in New Zealand white rabbits.	More newly formed trabeculae, vessels, and endochondral bone were observed during early-stage bone repair *in vivo* in groups treated with specific mineralized DCBM.	[24]
Collagen	N/A	Directional freezing	5 mm femur defect in rats	Collagen with a channel-like pore architecture can control cell recruitment and tissue patterning for bone healing.	[27]
	Adipose Stromal cells (ASC's)	Type I collagen and Bone Morphogenetic Protein 6 (BMP-6).	Ectopic model in nude mice	ASC's can generate ectopic bone through ECO in the presence of collagen type I foam, similar to BMSC.	[28]
	Skeletal stromal cells (SSC's) and B6.Cg-Tg(ACTb-eGFP) mice embryos.	Encapsulation of SSC in collagen capsules	Ectopic model in NMRI nu/nu mice	Collagen with encapsulated SSCs delivers biochemical cues that guide their differentiation towards the osteogenic lineage	[29]
	Angiostatin	Loading Mesenchymal Stromal Cells (MSC's) onto collagen I scaffolds with or without angiostatin	Ectopic model in Lewis rats.	Angiostatin reduced inflammation and vascularization but did not induce fibrocartilage formation in subcutaneously implanted collagen scaffolds with or without MSC in rats.	[31]
	Vascular Endothelial Growth Factor (VEGF) and Bone Morphogenetic Protein 2 (BMP-2)	Isolation of bovine collagen, and fabricating uni- and multidirectional scaffolds by freezing the collagen dispersion, followed by lyophilization. VEGF and BMP-2 were loaded with cell culture medium.	Muscular pockets in Wistar rats	Unidirectional collagen scaffolds had superior mechanical properties and liquid uptake capacity compared to multidirectional ones. Additionally, both types of scaffolds supported cell growth and osteoblastic differentiation *in vitro* and supported bone formation when loaded with BMP-2 or BMP-2 + VEGF, with pore orientation affecting the osteogenic process.	[32]
	Oxysterol (Oxy133)	Loading Oxy133 on collagen sponges	Spinal fusion in Lewis rats	Oxy133 induces significant expression of osteogenic markers and shows potential as an osteogenic molecule with improved synthesis and fusion time.	[33]
	Salvianic acid (SAA)	Loading a compound of SAA and a bone targeting liposome (SAA-BTL) on collagen sponges.	Radius defect in New Zealand rabbit	SAA-BTL-incorporated collagen sponges significantly stimulated bone formation in the nonunion defect rabbit model. Also, increased the expression of P-HDAC3, collagen II, RUNX2, VEGFA, and osteocalcin.	[34]
Type I collagen and hyaluronic acid (HA)	Bone marrow stromal cells (BMSC's)	Resuspend the BMSCs in collagen or hyaluronic acid to create hydrogels containing the cells.	Ectopic model in nude mice	*In vivo*, both collagen and HA constructs promoted vascularization, endochondral bone formation, and bone marrow development. However, HA constructs demonstrated superior fusion ability, forming integrated bone tissues with evidence of vascularization and marrow development between fused grafts.	[19]
Gelatin	N/A	Crosslinking of gelatin scaffolds by carbodiimide chemistry	Ectopic model in C57BJL/6 mice	EDC treatment enhances trabecular bone formation; and the high mechanical strength of 3D scaffolds promotes stem cell-mediated bone regeneration through endochondral ossification.	[20]

(*continued on next page*)

Table 1 (*continued*)

Material	Loading or complement	Fabrication	*In vivo* model	Key findings	Ref
	Basic fibroblast growth factor (bFGF)	Crosslinking of gelatin scaffolds with glutaraldehyde	Critical size femur defect on C57BL/6 mice	Hydrogels incorporating bFGF showed significantly stronger bone regeneration compared to bFGF solutions.	[36]
	Transforming growth factor beta 1 (TGF-β1), bone morphogenetic protein 2 (BMP-2), Bone marrow stromal cells (BMSC's)	Soaking gelatin hydrogels in BMP-2 solution.	Femoral defects in rabbits and Rowett nude (RNU) rats.	Promotion of bones and blood vessel formation in a femur defect model in a New Zealand rabbit.	[37]
		Encapsulating TGF-β1, BMP-2 and BMSC's in gelatin microspheres.	Calvarial defect in Rowett nude (RNU) rats	Mesenchymal condensations induce bone formation based on morphogen presentation, with BMP-2 + TGF-β1 fully restoring mechanical function.	[38]
Alginate	RGD and QK peptides and kartogenin	Microscaffolds of alginate and RGD, loaded with Kartogenin, and a final layer of RGD and QK peptides. Crosslinking was made by carbodiimide chemistry.	Ectopic model in BALB/c nude mice	Alginate, RGD and QK microscaffold-hydrogel composites effectively accelerate bone growth and enhance stem cell behavior, and controlled release of kartogenin induces chondrocyte differentiation and hypertrophy for accelerated osteochondral repair.	[42]
	Magnesium	Mixed sodium alginate with BMSC's in a Mg enrichment culture medium.	Critical size cranial defect in Sprague Dawley rats	The Mg-enriched cell delivery vehicles promote osteogenic differentiation of stromal cells and lead to significant vascularized bone regeneration in rats with critical-sized cranial defects.	[21]
	Adipose Stromal cells (ASC's)	Loaded ASC's within alginate beads	Ectopic model in nude mice	Comparisons against ASC constructs in high-density pellets versus alginate bead hydrogels indicated that hydrogel culture may be a more promising method for bone tissue engineering via the endochondral pathway due to the exhibit better vascularization and higher cell retention.	[43]
Hypertrophic cartilage matrix	Adipose Stromal Cells (ASC's)	Culture of fractionated human liposuction for 3 weeks and posterior culture of ASC's to hypertrophic differentiation for 2 weeks.	Ectopic model in nude mice	Employing adipose tissue as a scaffold exhibited enhanced *in vitro* differentiation and superior *in vivo* performance in comparison to the conventional approach of isolating and expanding ASCs in monolayers.	[44]
		Decellularization of bovine juvenile trabecular bone and ASC's differentiated to chondrogenic lineage.	5 mm femur defect in RNU nude rats	Tissue-engineered bone grafts using hypertrophic chondrocytes led to enhanced bone deposition and bridged a higher number of defects compared to osteoblast grafts and acellular scaffolds.	[45]

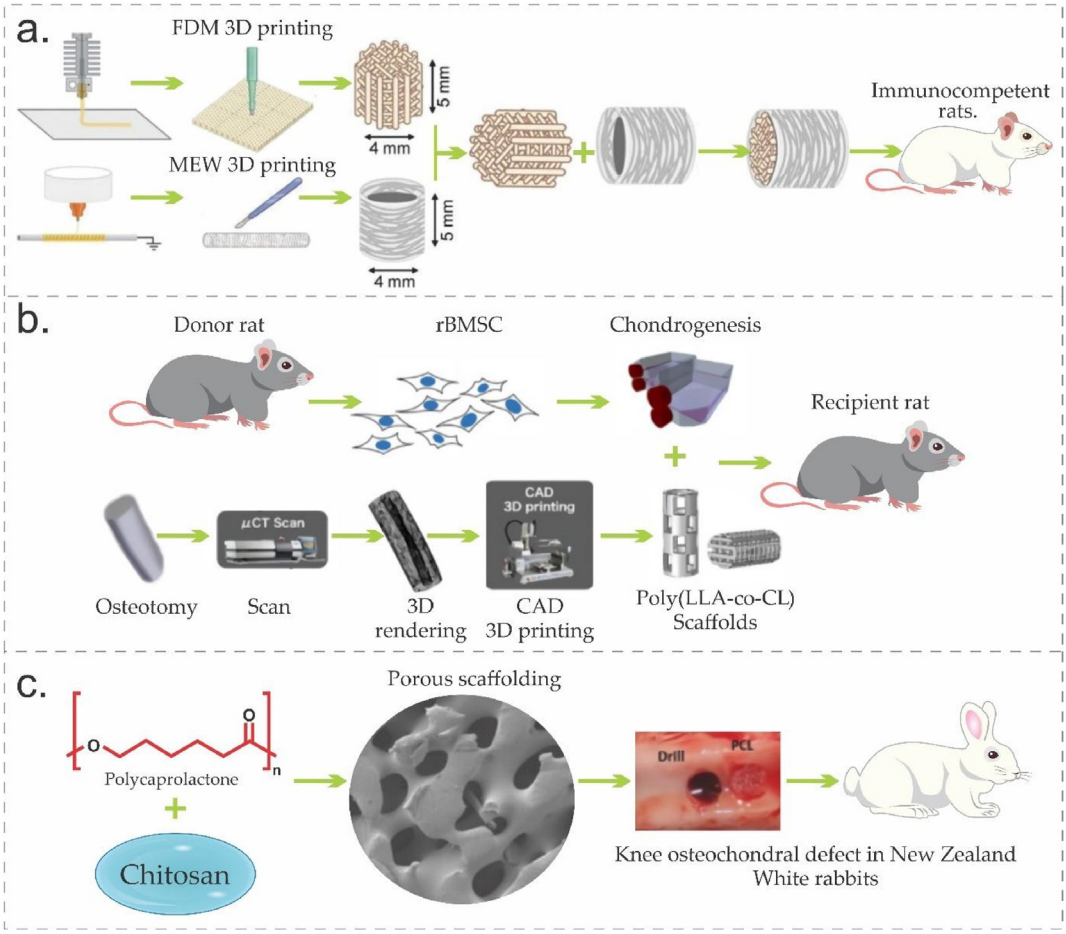


Fig. 3. Application of non-calcium compounds in bone tissue engineering approaches using synthetic biomaterials. a. Schematic representation of the 3D printed scaffold created using fused deposition modeling (FDM) and scaffold fabrication using Melt Electrowriting (MEW). The 3D scaffold was assembled by combining the inner implant core and the MEW membrane. The *in vivo* evaluation of the scaffold shows the functionalization and vascularization of the mimetic periosteum (Adapted from Ref. [47]). b. The tube scaffold is designed with a simulated medullary canal and has pores on its walls to stimulate vascularization. In contrast, the cylindrical scaffold is fabricated using a 0/90 lay-down pattern. Rat bone marrow-derived mesenchymal stem cells (rBMSC) were seeded onto printed scaffolds and underwent sequential chondrogenesis for 21 days. Afterward, they were implanted into the defects for a follow-up period of up to 15 weeks (Adapted from Ref. [48]). c. PCL scaffolds coated with chitosan to create a composite material, which was then evaluated for its effects on various tissue regeneration processes. (Adapted from Ref. [49]).

the initial stages of EO processes for large bone healing (Fig. 3b) [48]. Similarly, PCL hydrogel-like structures have been explored as alternatives to traditional scaffolds for mimicking hypertrophic cartilage microtissues. Polycaprolactone-based structures coated with chitosan and various cell lines, such as hBMSCs and human umbilical vein endothelial cells (HUVECs), have been used to achieve complete and efficient bone regeneration [52].

These studies have shown promising results of polycaprolactone scaffold approaches, such as ectopic bone formation, mineralized hypertrophic cartilage, and vascularization along the scaffold in various animal models, principally in the murine and lagomorph models, which are considered some of the most relevant models for BTE studies. In addition, low immune responses have been reported, suggesting scaffold integration and healing of critical-size bone defects throughout the EO in many cases (Fig. 3c) [49,52].

Besides PCL, PGA has been extensively studied and used in BTE applications. This thermoplastic polymer has been combined with different cell lines using porous scaffolds as a support structure and a cell therapy delivery vehicle. For example, 3D scaffolds enriched with BMSCs or chondrocytes have been developed to mimic endogenous bone-healing processes by promoting hypertrophic cartilage formation. Notably, preclinical rat models have shown vascularization in the scaffold, high-density mineralization, cell recruitment, and osteoclast activity throughout the implanted area, suggesting that endochondral processes were occurring [59,60].

Similarly, PEG is one of the most commonly used synthetic polymers for the development of degradable hydrogels. This specific structure was designed to mimic the characteristics of the extracellular matrix of cancellous bone. In this sense, proteins such as metalloproteinase (MMP) and thiolene alginate have been mixed with PEG, and stem cells or periosteum-derived cells are some of the most relevant approaches. These strategies support blood vessels and nerves in the graft, resulting in increased ectopic bone formation, density, and better structural incorporation of the implanted scaffold into the endogenous bone. Interestingly, these alternatives could overcome the lack of treatment availability and the osseointegration problems of traditional treatments [54,56].

Furthermore, elastomeric polymers have been used in BTE, which are desirable because they offer customizable properties amenable to bone regeneration. For example, poly(glycerol sebacate) (PGS) is considered one of the most promising materials for BTE because its stiffness can be tuned to match osteoid or immature tissue rather than mature bone. It has been shown that tailoring these specific mechanical properties is sufficient to induce mechanobiological responses that promote bone regeneration. This means that PGS is a promising material that needs to be thoroughly

Table 2
Studies in bone tissue engineering using synthetic polymeric biomaterials.

Material	Loading or complement	Fabrication	*In vivo* model	Results	Ref
PCL	BMP-2 expressing cells	Electrospinning and freeze- drying techniques	Subdermal implantation on nude mice	*In vitro* osteogenic differentiation was achieved on the microporous scaffold. Additionally, subdermal implantation of the cell-loaded scaffold showed cell infiltration, cartilage-like tissue formation, and hypertrophic cartilage matrixes.	[50]
	rhBMP-2	3D printing and melt electrospinning	5 mm femur defect on rats	Bone volume and density were achieved after 10 weeks of implantation on the femur defect, suggesting complete healing.	[47]
Poly(ethylene glycol) diacrylate	Human articular chondrocytes (hACs) & Human mesenchymal stem cells (hMSCs)	Photo Encapsulation in polymeric hydrogels	2-mm segmental defect by osteotomy in the mid-tibial diaphysis of immunocompromised mice	Cartilage grafts enhance bone regeneration, promoting highly vascularized new bone tissue.	[51]
Chitosan, PCL, fibrin, gelatin hyaluronic acid	HUVECs & hBMSCs	3D printing and bioprinting	Subcutaneous implantation on nude mice	Pre-vascularized scaffold showed a higher potential, promoting higher mineralization and angiogenesis after 4 weeks prior subcutaneous implantation	[49,52]
PGA, hyaluronic acid, and fibrin	hBMSCs	Hydrogel	3,5 mm one defect on parietal lobes on transgenic mouse	*In vivo* study showed a high capacity for cell recruitment all over the hybrid matrix, leading to new bone formation and highly vascularized structures through endochondral ossification processes.	[53]
PEG, MMP	mMSCs, adipose tissue pellets	Hydrogel	4 mm femoral defect on murine models	Metalloproteinase hydrogels showed increased new vessel formation and density, coupled with high nerve density, after 9 weeks. The scaffold was shown to induce early endochondral ossification and new bone formation.	[54]
Poly(L-lactide-co-epsilon-caprolactone) (poly(LA-co-CL))	Rat bone marrow mesenchymal stem cells (rBMSC), pre-differentiated *in vitro* into cartilage-forming chondrocytes	3D printing	Critical-sized (5 mm) femur defects on rats	Significant new bone was formed inside and in the periphery of the implanted scaffold. Also, bone marrow space was reported with connective tissue, adipocytes, and mononuclear cells.	[48]
Silicone	Periosteal strips	Silicone elastomer sheeting	2,54 cm Mid-diaphysis bone defect on sheeps	Substitutes loaded with periosteal strips, proved to be significantly more efficient, inducing ectopic bone formation and bone regeneration within the muscle.	[55]
Thiol-ene alginate	3D Bioprinting	Hydrogel	Subcutaneous implantation on mice	Ectopic bone formation was evidenced on the implanted scaffold. This approach induced nodules of mineralized tissue.	[56]
PGS	rBMSCs	Casting and particulate leaching	16 mm Ulna defect on rabbits	Runx2 and Osteocalcin gene expression were increased in the PGS scaffold. Moreover, complete defect bridging was achieved after 4 weeks.	[57]
PLLA	VEGF	Core-shell electrospinning	Rat 5 mm diameter calvarial defect	Membranous porous scaffolds completely repaired the defect zone and formed a periosteum-like structure. Bone density and hyaline-like cartilage were found, indicating endochondral ossification repairing processes.	[58]

tested [57]. Similarly, a silicone elastomer film was used as a barrier membrane to mimic the key structural and functional properties of native periosteal tissue, including elastin, collagen, and progenitor cells. These results suggest that the elastomeric film generates bone tissue primarily through endochondral mechanisms [55].

Overall, the reported findings on elastomeric polymer scaffolds have made them promising alternatives for BTE. Nevertheless, the lack of follow-up studies and more robust results indicate that this novel approach requires extensive research that could lead to specific bone repair and regeneration mechanisms when using these materials in scaffold design.

On the other hand, scaffold design has focused on more than just creating a support structure or delivering cell therapy. The incorporation of bioactive molecules such as VEGF, BMP-2, TGF-β3 and IL-8 has gained prominence as these factors have been shown to promote faster and more efficient healing of critical bone defects. For example, PEG hydrogels encapsulating BMSCs and chondrocytes have been loaded with BMP-2 and TGF-β3 to enhance cellular response. Similarly, bioactive glass and poly(L-lactic acid) (PLLA) electrospun scaffolds have been used as bioactive molecule delivery systems for interleukin-8 (IL-8), BMP-2, and VEGF. These studies have concluded that the incorporation of these molecules into scaffolds is a novel approach to designing bone healing strategies. The sustained release of these factors leads to the development of endochondral bone, forming osteochondral components that could potentially lead to endochondral ossification processes. Although promising results have been achieved, process optimization and encapsulation efficiency must be considered [51,58,61].

In summary, several approaches to bone tissue engineering have been undertaken in recent years using synthetic materials and moving beyond calcium compounds. Studies have shown how different strategies have led to a new understanding of bone repair processes and how this mechanism can be used to induce early stages of endochondral ossification, healing and repair of critical bone defects.

Table 3
Metallic scaffolds that have been evaluated for *in vivo* endochondral bone repair.

Material	Loading or complement	Fabrication	*In vivo* model	Results	Ref
Titanium	N/A	3D printing	4 cm tibial defect on sheeps	Bone formation was observed, and complete bone bridging was achieved.	[62]
			Ovine lumbar fusion	Cell migration to the scaffold leads to cancellous bone formation. Osseointegration was achieved, and endochondral ossification was evident on the titanium scaffold.	[63]
CoCrMo	N/A	3D printing	Tibial defects on rabbits	Fibrocartilaginous tissue and a large/dense area of interconnected trabeculae. Additionally, angiogenesis was confirmed by the presence of multiple blood vessels in the trabecular area of the scaffold.	[64]

1.2.2. Metallic scaffolds

Metallic materials such as titanium and titanium alloys have become useful in orthopedic and bone replacement therapies due to their superior mechanical properties. Known for their remarkable strength and biocompatibility, they have been tested in relevant environments that have positioned them not only as replacement materials but also as repair and bone tissue engineering materials. In this sense, lagomorph and ovine models have been extensively used to study them due to their anatomical similarity to humans in this specific tissue. In addition, the locomotion, bone healing similarity, and vascularization comparability of these models have established them as gold standard models. Table 3 shows the metallic materials and their corresponding *in vivo* results.

Recently, versatile additive manufacturing technology has been used with superior metal/polymer-based filaments, causing 3D printed metallic scaffolds to take particular relevance due to their matching mechanical properties and optimizing pore size, emphasizing the importance of mechanobiological stimulation in critical-size bone defect healing. Therefore, titanium-printed scaffolds have shown superior mechanical properties and osteoinductive and osteoconductive potential even more than novel materials, including PEEK. These characteristics have been successfully applied in preclinical ovine models with excellent results, mechanically supporting bone structures and enhancing tissue regeneration, indicating EO processes [62,63]. In addition, 3D-printed metallic alloys have been studied. For example, lagomorph models were used for carrying out trials of the effects of UV photofunctionalization of a CoCrMo alloy to improve its bioactivity for bone formation, revealing that photofunctionalized CoCrMo scaffolds exhibited superior bone formation and integration compared to untreated implants [64]. This highlights the potential of UV photofunctionalization to enhance the bioactivity of orthopedic materials.

1.3. Cells and cellular scaffolds

In recent years, cells and cell-derived biological matrices have been widely used in tissue engineering solutions to heal critical defects in long bones. Preclinical studies have shown that these tissue engineering strategies are a promising source of therapies for regeneration of large bone defects by guiding endogenous bone formation, mineralization, and critical defect bridging.

1.3.1. Cell approaches

A major focus of tissue engineering research has been using cells for bone repair via endochondral ossification. Mesenchymal stromal cells (MSCs) have been investigated for their potential to promote bone regeneration via endochondral ossification. This section reviews various applications and recent advances in cellular approaches to BTE. The discussion focuses on the changing landscape of cell-based strategies, highlighting their potential impact and advances in addressing critical bone defects through *in vivo* evaluations. Table 4 summarizes cell-based strategies tested for their efficacy in bone repair through endochondral ossification, demonstrating the transformative potential of cellular interventions in bone regeneration. In recent years, cells and cell-derived biological matrices have been widely used in tissue engineering solutions to heal critical defects in long bones. Preclinical studies have shown that these tissue-engineering strategies are a promising source of therapies for large bone defect regeneration by guiding endogenous bone formation, mineralization, and critical defect bridging.

MSCs play a critical role in BTE due to their multipotent nature and ability to differentiate into multiple cell types. They offer the potential for tissue repair and regeneration in regenerative medicine applications. BMSCs are particularly attractive due to their immunomodulatory properties, self-renewal and high proliferative capacity. These cells can differentiate into multiple lineages, including osteogenic, adipogenic, and chondrogenic pathways, making them valuable for various tissue engineering approaches [65]. Various studies have consistently demonstrated the ability of BMSCs to differentiate into chondrocytes and promote bone formation *in vivo* through endochondral ossification (ECO), making them an attractive candidate for bone regeneration and repair of critical defects [73,74]. Fig. 4 shows different methods that use BMSC for bone repair through endochondral ossification that have been demonstrated *in vivo*.

The epigenetic profile of BMSCs has been identified as a critical factor influencing their ability to mature into functional hypertrophic cartilage and facilitate bone defect healing via endochondral ossification [75,76]. In particular, the induction of chondrogenic and osteogenic pathways in these cells accelerates bone regeneration via endochondral ossification. For example, cartilage-like tissue with a calcified bone layer promotes healing, as demonstrated in a severe combined immunodeficiency mouse calvarial defect model (Fig. 4a) [77]. Furthermore, studies have shown that supplementation of BMSCs with bioactive substances such as dioscin and mangiferin (MAG) or their integration into the extracellular matrix can significantly improve bone formation via endochondral ossification in mouse models mimicking endochondral ossification (Fig. 4b, c, and 4d) [66–68].

Therapeutic applications of BMSCs go beyond direct cellular treatments. BMSC-derived exosomes have been shown to be important in promoting fracture repair in mouse models. These nanovesicles carry bioactive molecules that can modulate cellular processes and promote tissue healing [78]. This is achieved by stimulating osteogenesis and angiogenesis, highlighting the osteogenic potential of BMSCs through paracrine signaling mechanisms (Fig. 4e) [69]. However, further research is needed to optimize transplantation protocols and to exploit the paracrine signaling pathways of BMSCs mediated by exosomes or extracellular matrix (ECM) components. This will enable the translation of these

Table 4
Strategies using cells evaluated *in vivo* for repairing critical bone defects.

Cell type	Strategy	Model	Key findings	Ref
BMSC	Chondrogenic and Osteogenic induction	Immunodeficiency mouse calvarial defect model	Cells differentiated into osteogenic cells provided bone matrix proteins to reconstruct the bone defect.	[65]
	Combined with Dioscin	Drill-hole injury in mice subchondral bone on the distal end of femur	Treatment of dioscin increased collagen type X expression and promoted the hypertrophic differentiation of BMSCs	[66]
	BMSC-derived chondrocytes planted on demineralized bone matrix with or without Mangiferin (MAG)	Middle femoral defect model in mice	MAG-treated, BMSC-based grafts have better osteogenesis in a mouse bone-defect model	[67]
	Integrated into their ECM	Ectopic bone formation on immunodeficient male mice	Constructs undergo N-cadherin-mediated condensation and subsequent chondrogenesis, mimicking endochondral ossification	[68]
	BMSC-derived exosomes	Transverse femoral shaft fracture on CD9−/− mice	MSC exosomes stimulate osteogenesis and angiogenesis for bone tissue repair process	[69]
Ad-MSCs	Combined with LLP2A alendronate (LLP2A-Ale)	Mid-femur fracture in osterix-mCherry (Osx-mCherry) male and female reporter mice	This combination increased endochondral bone formation and enhanced callus maturation compared to LLP2A-Ale alone	[70]
hOA	Hypertrophic cartilage grafts	Segmental defects unilaterally at the tibial middiaphysis of immunocompromised mice	hOA can be transformed into endochondral tissues that are able to integrate with host bone, undergo vascularization, and heal critical-size long-bone defects in mice.	[59]
PDCs	Microaggregates with BMP-2	Tibia defect in immunodeficient mice	Vascularization, hypertrophic chondrocyte production, and endochondral ossification	[71]
iPSCs	Cartilaginous Organoids	Critical size long bone (tibia) defects of NMRI nu/nu mice	Cartilaginous organoids successfully bridged critical size long bone defects	[72]

findings into effective clinical interventions for bone abnormalities and fractures.

In addition to BMSCs, other cell sources such as Ad-MSCs, hOAs, PDCs, and iPSCs have demonstrated promising therapeutic potential for healing bone defects when combined with osteoinductive factors. The ability of these cells to generate hypertrophic cartilage is critical to their ability to heal damage through endochondral processes. For example, Ad-MSCs have effectively enhanced femur fracture repair in murine models when co-administered with LLP2A alendronate (LLP2A-Ale). This improved callus maturation and enhanced endochondral bone formation compared to LLP2A-Ale treatment alone [70]. Similarly, hOAs have demonstrated the ability to produce hypertrophic cartilage grafts that can integrate with host bone, undergo ossification, and promote the healing of critical-sized bone lesions in immunocompromised mice through endochondral repair processes [59].

Additionally, PDCs in microaggregate form with BMP-2 have been shown to induce chondro-osteogenic lineages *in vitro*. Upon *in vivo* implantation, PDCs have been shown to promote vascularization, hypertrophic chondrocyte formation, and endochondral ossification in a critical-sized murine tibial lesion model [71]. On the other hand, iPSCs have successfully generated both cartilage and bone tissue *in vitro* and *in vivo*. The cartilage tissue derived from these cells has been shown to effectively promote bone healing in an orthotopic model [72]. This study highlights the potential of induced pluripotent stem cells for creating functional skeletal tissue intermediates. These findings show the therapeutic potential of various sources of MSCs and the importance of exploring new strategies to improve bone healing and regeneration.

1.3.2. Cartilaginous templates

Researchers have explored various cartilage template-based strategies to address graft integration and vascularization challenges in bone tissue engineering. These templates promote bone regeneration through endochondral ossification by serving as temporary biomimetic structures that imitate the natural process of bone formation and facilitate bone healing, particularly in critical-size bone defects. Cartilage templates use the principles of endochondral ossification to help chondrocytes differentiate into hypertrophic cartilage. This cartilage then undergoes mineralization and remodeling, leading to the formation of new bone tissue. This process resembles the developmental and repair sequences observed during embryonic development and fracture healing. Ultimately, this enhances bone regeneration outcomes aligned with the body's native bone healing mechanisms [79].

One innovative approach is utilizing cartilage tissue derived from stem cells to stimulate bone repair through endochondral ossification. This method replicates the natural processes observed during embryonic development and fracture repair, demonstrating the potential for promoting bone repair through tissue transformation in a mouse model of segmental tibial lesions [80]. The study demonstrates that chondrocytes can be transformed into osteoblasts by activating the pluripotent transcription factor Oct4A. Additionally, endothelial cells can mineralize cartilage explants by secreting one BMP or providing a conditioned medium. These findings advance the understanding of how stem cell-derived cartilage can contribute to bone regeneration.

Recent advances in generating hypertrophic cartilage (HyC) templates from mesenchymal stromal cells (MSCs) have shown promise for improving orthotopic bone healing outcomes. Devitalized human hypertrophic cartilage extracellular matrix (hHyC-ECM) has demonstrated superior efficacy in rabbit defect models compared to currently available clinical products [81]. This innovative approach highlights the potential of utilizing HyC templates derived from MSCs to enhance bone regeneration and repair in orthotopic settings.

Additionally, investigations into enhancing the osteogenic potential of engineered hypertrophic cartilage through the involvement of monocytes have yielded varied results [82]. Although initial studies aimed at improving bone healing through monocyte participation showed promise, subsequent research has reported mixed outcomes with limited effects on remodeling or invasion processes. These findings emphasize the challenge of regulating the osteogenic properties of engineered hypertrophic cartilage and the necessity for additional research to determine the best methods to maximize the regenerative potential of HyC templates in bone healing applications.

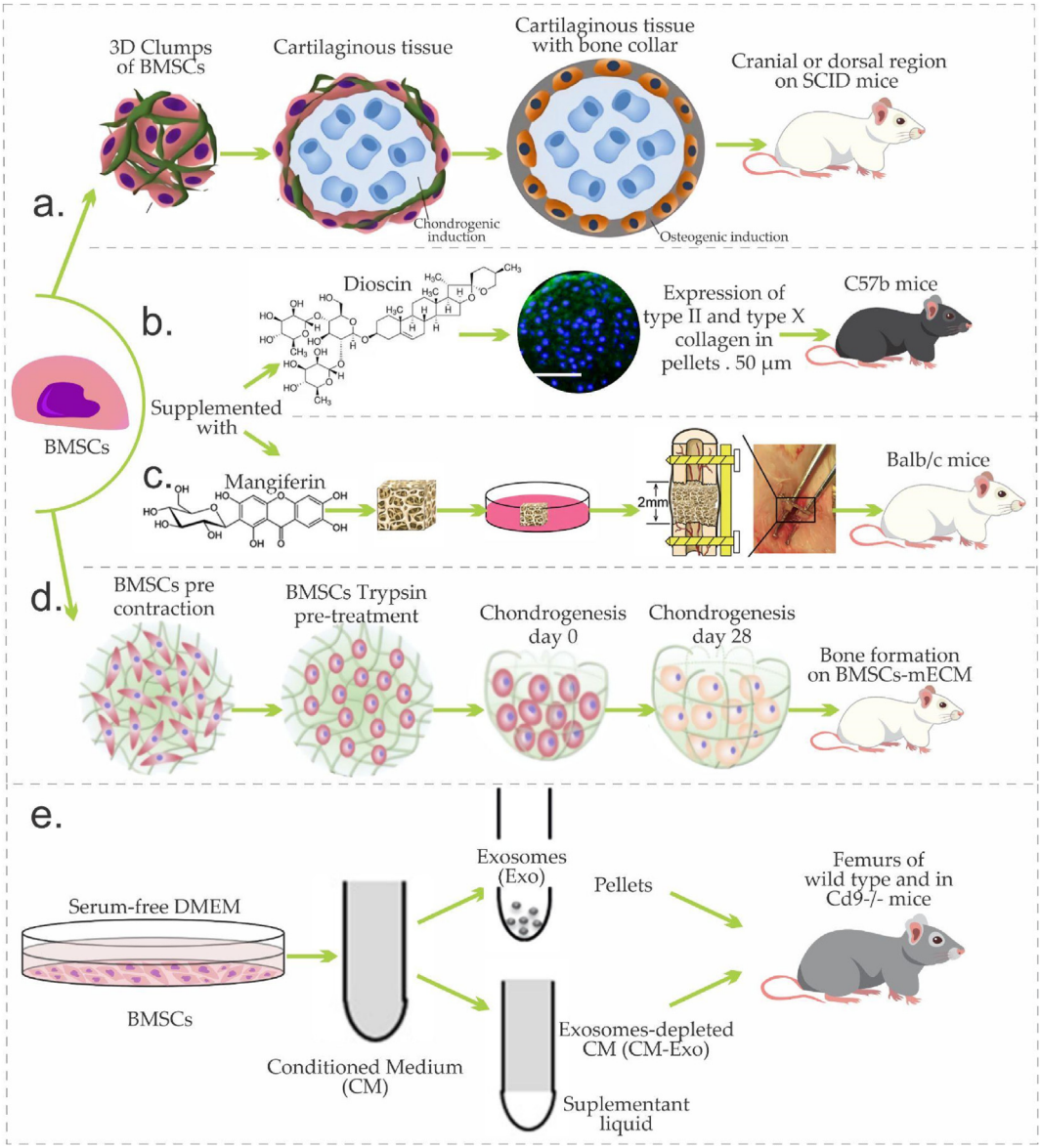


Fig. 4. Methods for bone repair by endochondral ossification studied *in vitro* and *in vivo* using BMSCs. a. C-MSCs were cultured in chondro-inductive and osteo-inductive mediums, resulting in cartilaginous tissue covered with a mineralized matrix layer. Treatment with only chondro-inductive medium resulted in cartilage with no mineralization. Transplantation of mineralized cartilaginous tissue induced rapid bone reconstruction via endochondral ossification in the mouse calvarial defect model. (adapted from Ref. [77]). b. BMSC pellets treated with Dioscin increase the expression of type II and type X collagen, promoting the osteochondrogenic differentiation of these cells. In animal models of subchondral bone fractures, Dioscin treatment enhance endochondral ossification (Adapted from Ref. [66]) c. The schematic diagram illustrates the process of endochondral ossification-based bone repair using BMSCs in combination with mangiferin. The cells were planted in the demineralized bone matrix for two weeks with MAG. The hypertrophic chondrocyte-based graft was implanted in a 2 mm bone defect in the middle of the femur in the mouse. This enhanced endochondral ossification-based bone repair. (Adapted from Ref. [67]). d. BMSCs embedded in their secreted ECM can form bone through endochondral ossification when given chondrogenic and osteogenic cues. A trypsin pre-treatment can alter cell morphology, enabling MSC-mECM constructs to undergo the condensation process and chondrogenesis. (Image adapted from Ref. [68]). e. Exosomes isolated from BMSC-conditioned medium (CM), supernatant without exosomes (CM-Exo), and an exosome pellet were injected into the fracture site. Delayed fracture healing in CD9−/− mice was rescued by injection of CM and exosomes. (adapted from Ref. [69]).

Similarly, decellularized scaffolds bioengineered and seeded with allogeneic BMSCs demonstrated osteoinductive properties. When implanted subcutaneously in mice, this type of scaffold induced vascularization and mineral accumulation, and half of the bone defects treated with hypertrophic cartilage scaffolds showed complete bridging [83].

Alternatively, injectable "cartilaginous" grafts incorporating particulate decellularized cartilage matrix, chondrogenically primed BMSCs bricks, and platelet-rich plasma gel have shown accelerated degradation of cartilage matrices and facilitated transformation processes, suggesting a promising avenue for generating vascularized bone tissue [84]. This approach showed that using BMSCs bricks in the constructs resulted in faster degradation of decellularized cartilage matrices, facilitating the transformation process. These findings suggest a promising method for generating vascularized bone tissue using injectable cartilaginous templates and BMSCs.

On the other hand, investigations into decellularized xenogenic hyaline cartilage xenograft matrices prepared using vacuum-assisted osmotic shock have demonstrated the preservation of structural integrity and differentiation potential for human chondrocytes and periosteum-derived cells [85]. This method preserves

Table 5
Mixed techniques and other methodologies applied in bone repair with their *in vivo* evaluation.

Material	Loading or complement	Fabrication	*In vivo* model	Key findings	Ref
Exogenous haploinsufficiency of endogenous parathyroid hormone-related peptide (PTHrP)	NA	Peptide extraction	Femur lessons on Wild-type and leptin receptor null Lepr(−/−) mice	Subcutaneous injection of PTHrP into Lepr(−/−) mice improves fracture repair by enhancing callus formation and accelerating cell transformation.	[87]
PCL	Cartilaginous spheroids from chondrogenic diff	Melt Electrowriting (MEW)	Ectopic and Orthotopic lesions on Immune compromised mice (Rj:NMRInu/nu)	Biohybrid lamellae, implanted subcutaneously for 4 weeks, mineralized (23 ± 3% MV/TV) and formed bone and bone marrow. Bone formation was observed when implanted in a critical-sized long bone defect in mice, although high variation between samples was detected.	[88]
	FPSCs & Chondrocytes BMSCs RGD- Alginate	Photoencapsulation on polymeric hydrogels	Osteochondral defect regeneration	The scaffolds facilitated the capture and fusion of cartilaginous spheroids with the potential to develop into bone.	[89]
Acceleration through whole body vibration	NA	Vibration-induced repair	Lessons from the eighth ribs on both sides in female Wistar Hanoverian rats	Low amplitude vibration (30-L) promotes chondrogenic differentiation and the expression of cartilage-related genes and may enhance fracture healing by promoting cartilage formation.	[90]
Osteoinductive autologous bone graft substitute (ABGS)	Recombinant human BMP6 (rhBMP6)	Bovine Achilles tendon-derived absorbable collagen sponge and bovine bone collagen as scaffold	Subcutaneous Rats implant and rabbit ulna segmental defect model.	The ABC scaffold within ABGS creates an environment conducive to bone formation, allowing the use of lower doses of rhBMP6 compared to other formulations. In addition, the newly formed bone remodels uniformly, integrating with the surrounding bone.	[91]

the structural and biological integrity of the cartilage xenograft matrix and allows differentiation of human chondrocytes and periosteum-derived cells. Similarly, devitalized cartilage constructs of allogeneic origin have demonstrated significant new bone production and defect-bridging capabilities after four weeks, indicating their potential for endochondral bone regeneration applications [86].

These diverse approaches utilizing cartilaginous templates or cartilaginous tissues underscore the multifaceted strategies available for enhancing bone regeneration outcomes and hold significant promise for future clinical applications in regenerative medicine.

1.4. Mixed scaffolds and other treatments

Innovative strategies have emerged to complement traditional approaches in the search for advanced techniques to repair endochondral bone. Among the interventions used are peptides, biohybrid films, microspheres, and autologous encapsulated and coagulated materials. They are all designed to enhance the effectiveness of bone healing mechanisms within endochondral repair. Table 5 and Fig. 5 provide an overview of the strategies and methodologies tested for bone defect repair, shedding light on the various approaches being investigated in bone regeneration.

Another approach to bone repair and fracture healing is the administration of parathyroid hormone-related peptide (PTHrP) (Fig. 5a). Studies have shown that PTHrP-derived peptides can enhance bone mass and strength, promote bone formation, and improve critical bone defect repair in various experimental models [92]. Moreover, exogenous PTHrP has been discovered to expedite fracture healing by promoting callus formation, upregulating osteoblastic gene and protein expression, and enhancing endochondral bone formation [87]. These findings regarding PTHrP's effects on bone tissue make it a promising candidate for promoting bone regeneration and addressing critical bone defects. Moreover, advancing enhanced PTH-related peptides provides a potential solution to overcome limitations associated with current treatments such as teriparatide, opening up new possibilities for improving bone metabolism and repair [93].

In a related development, researchers have investigated the combination of cartilage spheroids with electrically melted polycaprolactone membranes (MEW) as a means of creating cellular implants that induce bone formation *in vivo* (Fig. 5b) [88]. Seeding microspheroids onto MEW meshes results in improved expression of chondrogenic and prehypertrophic gene markers. Implantation of these biohybrid sheets has led to mineralization and bone formation, demonstrating their potential for treating critical-sized bone defects in murine models. The versatility of these scaffolds in bone repair applications is highlighted by their adaptability to varying defect sizes, as well as individual patient needs. This synergistic approach leverages the unique properties of each component to foster regenerative processes and facilitate bone regeneration through innovative scaffold design.

Furthermore, researchers have explored other mixed scaffold techniques, such as integrating 3D-printed polycaprolactone with alginate hydrogels and stem cells, to engineer constructs that mimic natural developmental processes for bone regeneration (Fig. 5c) [89]. These constructs have demonstrated the ability to induce endogenous endochondral ossification healing processes and promote the formation of cartilage resembling hyaline cartilage in caprine models. Moreover, the use of recombinant human bone morphogenetic protein 6 (rhBMP6) and autologous blood coagulum (ABC) as carriers for autologous bone graft substitutes has shown potential in enhancing the repair of critical bone defects and promoting bone formation in animal models (Fig. 5e) [91].

On the other hand, studies have demonstrated that vibration therapy can positively impact angiogenesis at the fracture site and surrounding muscles during the healing process (Fig. 5d) [94]. This therapy has been found to enhance bone callus formation, mineralization, and remodeling, ultimately accelerating osteoporotic fracture healing [95]. The mechanism through which vibration treatment influences fracture healing involves improving callus formation, mineralization, and remodeling processes [90].

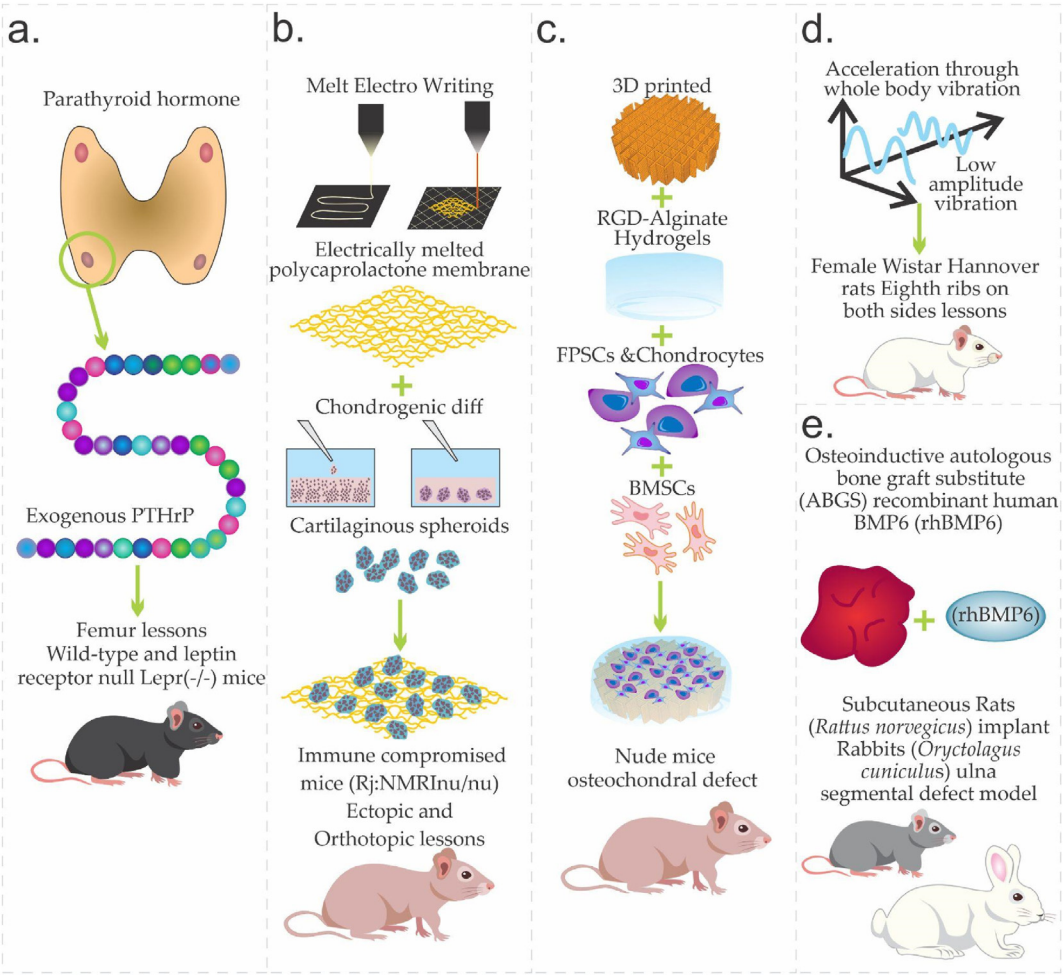


Fig. 5. Mixed and other techniques: a. graphic description of exogenous PTHRP tested in femur lesions of Lepr(−/−) mice (Adapted from Ref. [92]); b. Melt Electro Writing fabrication method, with spheroids from *in vitro* chondrogenic differentiation tested in immuno-compromised mice (Adapted from Ref. [88]); c. mix between 3D printed RGD-Alginate hydrogel functionalized with FPSC coculture and chondrocytes with BMSCs tested in osteochondral defects of nude mice (Adapted from Ref. [89]); d. Acceleration through whole-body vibration was tested in the number 8 ribs of Wistar Hannover rats (Adapted from Ref. [94]) e. Osteoinductive autologous bone graft substitute with recombinant human BMP6 was tested subcutaneously in *Rattus norvegicus* and *Oryctolagus cuniculus* ulna segmental defect (Adapted from Ref. [91]).

2. Conclusions and perspectives

Significant progress has been made in bone tissue engineering to develop effective regenerative strategies that use different biomaterials combined with cells and growth factors but without calcium components. Due to the complexity of biological systems, a multidisciplinary research approach is required to address key challenges. One of these challenges is the stimulation of the vasculature within scaffolds or constructs to ensure their survival and functional integrity after implantation. Tuning the mechanical properties of scaffolds to mimic natural tissues facilitates seamless integration with host tissues.

Recently, novel techniques inspired by embryonic processes have emerged and shown great promise. Advanced co-culture models incorporating different cell types are being developed to mimic the native stem cell microenvironment better. As our understanding of these mechanisms deepens, further advances are expected. At the same time, advances in material selection and manufacturing techniques are making commercially available products suitable for routine clinical use more feasible. This trend highlights the increasing viability of off-the-shelf solutions that can help researchers translate their discoveries into practical and effective treatments.

Achieving these goals requires a collaborative, multidisciplinary effort involving biologists, chemists, engineers, physicians, and orthopedic surgeons. Combining expertise across disciplines allows *in vitro* findings to be effectively translated into viable treatments. The future of bone regeneration therapy is bright because of the dedicated collaboration within the scientific community. This collaborative approach fosters innovation and accelerates the development of breakthrough solutions for complex bone defects.

Maintaining an ongoing dialogue and knowledge sharing among stakeholders is critical to advancing regenerative platforms and improving patient outcomes. The transformative potential of collaborative efforts is driving advances in bone tissue engineering, resulting in improved clinical applications and patient care.

Author contributions

William Cárdenas-Aguazaco, Adriana Lorena Lara-Bertrand, Leonadro Prieto-Abello, Nicolás Barreto-López and Ingrid Silva-Cote contributed significantly to the research, evaluation, writing, analysis, and interpretation of the consulted articles. Bernardo Camacho secured funding, and he critically reviewed the final manuscript. All authors have read and approved the published version of the manuscript.

Declaration of competing interest

Authors have no conflict of interest to declare.

Acknowledgements

This work was funded by the Instituto Distrital de Ciencia, Biotecnología e Innovación en Salud-IDCBIS.

References

[1] Kiernan C, Knuth C, Farrell E. Chapter 6 - endochondral ossification: recapitulating bone development for bone defect repair. In: Stoddart MJ, Craft AM, Pattappa G, Gardner OFW, editors. Dev. Biol. Musculoskelet. Tissue eng. Boston: Academic Press; 2018. p. 125–48. https://doi.org/10.1016/B978-0-12-811467-4.00006-1.

[2] Bi M, Yang K, Yu T, Wu G, Li Q. Cell-based mechanisms and strategies of co-culture system both in vivo and vitro for bone tissue engineering. Biomed Pharmacother 2023;169:115907. https://doi.org/10.1016/j.biopha.2023.115907.

[3] Karalashvili L, Kakabadze A, Uhryn M, Vyshnevska H, Ediberidze K, Kakabadze Z. Bone grafts for reconstruction of bone defects (review). Georgian Med News 2018:44–9.

[4] Fesseha H, Fesseha Y. Bone grafting, its principle and application. A Review 2020:43–50. https://doi.org/10.17140/ORHOJ-1-113.

[5] Amini AR, Laurencin CT, Nukavarapu SP. Bone tissue engineering: recent advances and challenges. Crit Rev Biomed Eng 2012;40:363–408. https://doi.org/10.1615/critrevbiomedeng.v40.i5.10.

[6] Migliorini F, La Padula G, Torsiello E, Spiezia F, Oliva F, Maffulli N. Strategies for large bone defect reconstruction after trauma, infections or tumour excision: a comprehensive review of the literature. Eur J Med Res 2021;26:118. https://doi.org/10.1186/s40001-021-00593-9.

[7] Kneser U, Schaefer DJ, Polykandriotis E, Horch RE. Tissue engineering of bone: the reconstructive surgeon's point of view. J Cell Mol Med 2006;10:7–19. https://doi.org/10.1111/j.1582-4934.2006.tb00287.x.

[8] Xue N, Ding X, Huang R, Jiang R, Huang H, Pan X, et al. Bone tissue engineering in the treatment of bone defects. Pharmaceuticals 2022;15:879. https://doi.org/10.3390/ph15070879.

[9] Stahl A, Yang YP. Regenerative approaches for the treatment of large bone defects. Tissue Eng Part B Rev 2021;27:539–47. https://doi.org/10.1089/ten.TEB.2020.0281.

[10] Koons GL, Diba M, Mikos AG. Materials design for bone-tissue engineering. Nat Rev Mater 2020;5:584–603. https://doi.org/10.1038/s41578-020-0204-2.

[11] Lodoso-Torrecilla I, Klein Gunnewiek R, Grosfeld E-C, De Vries RBM, Habibović P, Jansen JA, et al. Bioinorganic supplementation of calcium phosphate-based bone substitutes to improve in vivo performance: a systematic review and meta-analysis of animal studies. Biomater Sci 2020;8:4792–809. https://doi.org/10.1039/D0BM00599A.

[12] Cárdenas-Aguazaco W, Camacho B, Gómez-Pachón EY, Lara-Bertrand AL, Silva-Cote I. Electrospun scaffolds of polylactic acid, collagen, and amorphous calcium phosphate for bone repair. Pharmaceutics 2023;15:2529. https://doi.org/10.3390/pharmaceutics15112529.

[13] Sun H, Yang H-L. Calcium phosphate scaffolds combined with bone morphogenetic proteins or mesenchymal stem cells in bone tissue engineering. Chin Med J (Engl) 2015;128:1121–7. https://doi.org/10.4103/0366-6999.155121.

[14] Germaini M-M, Belhabib S, Guessasma S, Deterre R, Corre P, Weiss P. Additive manufacturing of biomaterials for bone tissue engineering – a critical review of the state of the art and new concepts. Prog Mater Sci 2022;130:100963. https://doi.org/10.1016/j.pmatsci.2022.100963.

[15] Henkel J, Woodruff MA, Epari DR, Steck R, Glatt V, Dickinson IC, et al. Bone regeneration based on tissue engineering conceptions - a 21st century perspective. Bone Res 2013;1:216–48. https://doi.org/10.4248/BR201303002.

[16] Abuarqoub D, Theeb LS, Omari MB, Hamadneh YI, Alrawabdeh JA, Aslam N, et al. The osteogenic role of biomaterials combined with human-derived dental stem cells in bone tissue regeneration. Tissue Eng Regen Med 2023;20:251–70. https://doi.org/10.1007/s13770-022-00514-9.

[17] Banyard DA, Bourgeois JM, Widgerow AD, Evans GRD. Regenerative biomaterials: a review. Plast Reconstr Surg 2015;135:1740–8. https://doi.org/10.1097/PRS.0000000000001272.

[18] Kasir R, Vernekar V, Laurencin C. Inductive biomaterials for bone regeneration. J Mater Res 2017;32:1–14. https://doi.org/10.1557/jmr.2017.39.

[19] Yamazaki S, Hirayama R, Ikeda Y, Iseki S, Yoda T, Ikeda M-A. Hyaluronic acid hydrogels support to generate integrated bone formation through endochondral ossification in vivo using mesenchymal stem cells. PLOS ONE 2023;18:e0281345. https://doi.org/10.1371/journal.pone.0281345.

[20] Sun H, Zhu F, Hu Q, Krebsbach PH. Controlling stem cell-mediated bone regeneration through tailored mechanical properties of collagen scaffolds. Biomaterials 2014;35:1176–84. https://doi.org/10.1016/j.biomaterials.2013.10.054.

[21] Lin S, Yang G, Jiang F, Zhou M, Yin S, Tang Y, et al. A magnesium-enriched 3D culture system that mimics the bone development microenvironment for vascularized bone regeneration. Adv Sci 2019;6:1900209. https://doi.org/10.1002/advs.201900209.

[22] Montes-Medina L, Hernández-Fernández A, Gutiérrez-Rivera A, Ripalda-Cemboráin P, Bitarte N, Pérez-López V, et al. Effect of bone marrow stromal cells in combination with biomaterials in early phases of distraction osteogenesis: an experimental study in a rabbit femur model. Injury 2018;49:1979–86. https://doi.org/10.1016/j.injury.2018.09.007.

[23] Knuth CA, Witte-Bouma J, Ridwan Y, Wolvius EB, Farrell E. Mesenchymal stem cell-mediated endochondral ossification utilising micropellets and brief chondrogenic priming. Eur Cell Mater 2017;34:142–61. https://doi.org/10.22203/eCM.v034a10.

[24] Liu S, Wang Y, Wang J, Qiu P, Wang S, Shi Y, et al. A cancellous bone matrix system with specific mineralisation degrees for mesenchymal stem cell differentiation and bone regeneration. Biomater Sci 2019;7:2452–67. https://doi.org/10.1039/c8bm01657g.

[25] Nadine S, Fernandes IJ, Correia CR, Mano JF. Close-to-native bone repair via tissue-engineered endochondral ossification approaches. iScience 2022;25:105370. https://doi.org/10.1016/j.isci.2022.105370.

[26] Feng Y, Shi Y, Tian Y, Yang Y, Wang J, Guo H, et al. The collagen-based scaffolds for bone regeneration: a journey through electrospun composites integrated with organic and inorganic additives. Processes 2023;11:2105. https://doi.org/10.3390/pr11072105.

[27] Petersen A, Princ A, Korus G, Ellinghaus A, Leemhuis H, Herrera A, et al. A biomaterial with a channel-like pore architecture induces endochondral healing of bone defects. Nat Commun 2018;9:4430. https://doi.org/10.1038/s41467-018-06504-7.

[28] Osinga R, Di Maggio N, Todorov A, Allafi N, Barbero A, Laurent F, et al. Generation of a bone organ by human adipose-derived stromal cells through endochondral ossification. Stem Cells Transl Med 2016;5:1090–7. https://doi.org/10.5966/sctm.2015-0256.

[29] Verbeeck L, Geris L, Tylzanowski P, Luyten FP. Uncoupling of in-vitro identity of embryonic limb derived skeletal progenitors and their in-vivo bone forming potential. Sci Rep 2019;9:5782. https://doi.org/10.1038/s41598-019-42259-x.

[30] Purushothaman AE, Abhinandan R, Adithya SP, Sidharthan DS, Balagangadharan K, Selvamurugan N. Bioactive molecule-incorporated polymeric electrospun fibers for bone tissue engineering. Curr Stem Cell Res Ther 2022;18:470–86. https://doi.org/10.2174/1574888X17666220414100358.

[31] Helgeland E, Pedersen TO, Rashad A, Johannessen AC, Mustafa K, Rosén A. Angiostatin-functionalized collagen scaffolds suppress angiogenesis but do not induce chondrogenesis by mesenchymal stromal cells in vivo. J Oral Sci 2020;62:371–6. https://doi.org/10.2334/josnusd.19-0327.

[32] Moncayo-Donoso M, Rico-Llanos GA, Garzón-Alvarado DA, Becerra J, Visser R, Fontanilla MR. The effect of pore directionality of collagen scaffolds on cell differentiation and in vivo osteogenesis. Polymers 2021;13:3187. https://doi.org/10.3390/polym13183187.

[33] Montgomery SR, Nargizyan T, Meliton V, Nachtergaele S, Rohatgi R, Stappenbeck F, et al. A novel osteogenic oxysterol compound for therapeutic development to promote bone growth: activation of hedgehog signaling and osteogenesis through smoothened binding: OXY133: compound for therapeutic development to promote bone growth. J Bone Miner Res 2014;29:1872–85. https://doi.org/10.1002/jbmr.2213.

[34] Zhou L, Wu H, Gao X, Zheng X, Chen H, Li H, et al. Bone-targeting liposome-encapsulated salvianic acid A improves nonunion healing through the regulation of HDAC3-mediated endochondral ossification. Drug Des Devel Ther 2020;14:3519–33. https://doi.org/10.2147/DDDT.S263787.

[35] Salehi Abar E, Vandghanooni S, Torab A, Jaymand M, Eskandani M. A comprehensive review on nanocomposite biomaterials based on gelatin for bone tissue engineering. Int J Biol Macromol 2024;254:127556. https://doi.org/10.1016/j.ijbiomac.2023.127556.

[36] Hiroyuki F, Yasuhiko T, Kazuo K. Bone regeneration for murine femur fracture by gelatin hydrogels incorporating basic fibroblast growth factor with different release profiles. TISSUE Eng Part A 2014;20:1531–41. https://doi.org/10.1089/ten.tea.2012.07631531.

[37] Kalay E, Ermutlu C, Yenigül AE, Yalçınkaya U, Sarısözen B. Effect of bone morphogenic protein-2 and desferoxamine on distraction osteogenesis. Injury 2022;53:1854–7. https://doi.org/10.1016/j.injury.2022.03.064.

[38] McDermott AM, Herberg S, Mason DE, Collins JM, Pearson HB, Dawahare JH, et al. Recapitulating bone development through engineered mesenchymal condensations and mechanical cues for tissue regeneration. Sci Transl Med 2019;11:eaav7756. https://doi.org/10.1126/scitranslmed.aav7756.

[39] Dang PN, Herberg S, Varghai D, Riazi H, Varghai D, McMillan A, et al. Endochondral ossification in critical-sized bone defects via readily implantable scaffold-free stem cell constructs. Stem Cells Transl Med 2017;6:1644–59. https://doi.org/10.1002/sctm.16-0222.

[40] Dai K, Deng S, Yu Y, Zhu F, Wang J, Liu C. Construction of developmentally inspired periosteum-like tissue for bone regeneration. Bone Res 2022;10:1. https://doi.org/10.1038/s41413-021-00166-w.

[41] Venkatesan J, Nithya R, Sudha PN, Kim S-K. Role of alginate in bone tissue engineering. Adv Food Nutr Res 2014;73:45–57. https://doi.org/10.1016/B978-0-12-800268-1.00004-4.

[42] Zhang H, Li Q, Xu X, Zhang S, Chen Y, Yuan T, et al. Functionalized microscaffold–hydrogel composites accelerating osteochondral repair

through endochondral ossification. ACS Appl Mater Interfaces 2022;14:52599–617. https://doi.org/10.1021/acsami.2c12694.
[43] Weiss-Bilka HE, McGann ME, Meagher MJ, Roeder RK, Wagner DR. Ectopic models for endochondral ossification: comparing pellet and alginate bead culture methods: the effect of culture method on ectopic endochondral bone formation. J Tissue Eng Regen Med 2018;12:e541–9. https://doi.org/10.1002/term.2324.
[44] Guerrero J, Pigeot S, Müller J, Schaefer DJ, Martin I, Scherberich A. Fractionated human adipose tissue as a native biomaterial for the generation of a bone organ by endochondral ossification. Acta Biomater 2018;77:142–54. https://doi.org/10.1016/j.actbio.2018.07.004.
[45] Bernhard J, Ferguson J, Rieder B, Heimel P, Nau T, Tangl S, et al. Tissue-engineered hypertrophic chondrocyte grafts enhanced long bone repair. Biomaterials 2017;139:202–12. https://doi.org/10.1016/j.biomaterials.2017.05.045.
[46] Huang R-L, Fu R, Yan Y, Liu C, Yang J, Xie Y, et al. Engineering hypertrophic cartilage grafts from lipoaspirate for critical-sized calvarial bone defect reconstruction: an adipose tissue-based developmental engineering approach. Bioeng Transl Med 2022;7:e10312. https://doi.org/10.1002/btm2.10312.
[47] Romero-Torrecilla JA, Lamo-Espinosa JM, Ripalda-Cemboráin P, López-Martínez T, Abizanda G, Riera-Álvarez L, et al. An engineered periosteum for efficient delivery of rhBMP-2 and mesenchymal progenitor cells during bone regeneration. NPJ Regen Med 2023;8:54. https://doi.org/10.1038/s41536-023-00330-2.
[48] Hara K, Hellem E, Yamada S, Sariibrahimoglu K, Mølster A, Gjerdet NR, et al. Efficacy of treating segmental bone defects through endochondral ossification: 3D printed designs and bone metabolic activities. Mater Today Bio 2022;14:100237. https://doi.org/10.1016/j.mtbio.2022.100237.
[49] Hoemann CD, Rodríguez González J, Guzmán-Morales J, Chen G, Jalali Dil E, Favis BD. Chitosan coatings with distinct innate immune bioactivities differentially stimulate angiogenesis, osteogenesis and chondrogenesis in polycaprolactone scaffolds with controlled interconnecting pore size. Bioact Mater 2022;10:430–42. https://doi.org/10.1016/j.bioactmat.2021.09.012.
[50] Xu T, Miszuk JM, Zhao Y, Sun H, Fong H. Electrospun polycaprolactone 3D nanofibrous scaffold with interconnected and hierarchically structured pores for bone tissue engineering. Adv Healthc Mater 2015;4:2238–46. https://doi.org/10.1002/adhm.201500345.
[51] Stüdle C, Vallmajó-Martín Q, Haumer A, Guerrero J, Centola M, Mehrkens A, et al. Spatially confined induction of endochondral ossification by functionalized hydrogels for ectopic engineering of osteochondral tissues. Biomaterials 2018;171:219–29. https://doi.org/10.1016/j.biomaterials.2018.04.025.
[52] Nulty J, Burdis R, Kelly DJ. Biofabrication of prevascularised hypertrophic cartilage microtissues for bone tissue engineering. Front Bioeng Biotechnol 2021;9:661989. https://doi.org/10.3389/fbioe.2021.661989.
[53] Mikael PE, Golebiowska AA, Xin X, Rowe DW, Nukavarapu SP. Evaluation of an engineered hybrid matrix for bone regeneration via endochondral ossification. Ann Biomed Eng 2020;48:992–1005. https://doi.org/10.1007/s10439-019-02279-0.
[54] Li Y, Hoffman MD, Benoit DSW. Matrix metalloproteinase (MMP)-degradable tissue engineered periosteum coordinates allograft healing via early stage recruitment and support of host neurovasculature. Biomaterials 2021;268:120535. https://doi.org/10.1016/j.biomaterials.2020.120535.
[55] Moore SR, Heu C, Yu NYC, Whan RM, Knothe UR, Milz S, et al. Translating periosteum's regenerative power: insights from quantitative analysis of tissue genesis with a periosteum substitute implant. Stem Cells Transl Med 2016;5:1739–49. https://doi.org/10.5966/sctm.2016-0004.
[56] Bolander J, Mota C, Ooi HW, Agten H, Baker MB, Moroni L, et al. Bioinspired development of an in vitro engineered fracture callus for the treatment of critical long bone defects. Adv Funct Mater 2021;31:2104159. https://doi.org/10.1002/adfm.202104159.
[57] Zaky SH, Lee KW, Gao J, Jensen A, Verdelis K, Wang Y, et al. Poly (glycerol sebacate) elastomer supports bone regeneration by its mechanical properties being closer to osteoid tissue rather than to mature bone. Acta Biomater 2017;54:95–106. https://doi.org/10.1016/j.actbio.2017.01.053.
[58] Wu L, Gu Y, Liu L, Tang J, Mao J, Xi K, et al. Hierarchical micro/nanofibrous membranes of sustained releasing VEGF for periosteal regeneration. Biomaterials 2020;227:119555. https://doi.org/10.1016/j.biomaterials.2019.119555.
[59] Bahney CS, Jacobs L, Tamai R, Hu D, Luan TF, Wang M, et al. Promoting endochondral bone repair using human osteoarthritic articular chondrocytes. Tissue Eng Part A 2016;22:427–35. https://doi.org/10.1089/ten.TEA.2014.0705.
[60] Bardsley K, Kwarciak A, Freeman C, Brook I, Hatton P, Crawford A. Repair of bone defects in vivo using tissue engineered hypertrophic cartilage grafts produced from nasal chondrocytes. Biomaterials 2017;112:313–23. https://doi.org/10.1016/j.biomaterials.2016.10.014.
[61] Lin D, Chai Y, Ma Y, Duan B, Yuan Y, Liu C. Rapid initiation of guided bone regeneration driven by spatiotemporal delivery of IL-8 and BMP-2 from hierarchical MBG-based scaffold. Biomaterials 2019;196:122–37. https://doi.org/10.1016/j.biomaterials.2017.11.011.
[62] Pobloth A-M, Checa S, Razi H, Petersen A, Weaver JC, Schmidt-Bleek K, et al. Mechanobiologically optimized 3D titanium-mesh scaffolds enhance bone regeneration in critical segmental defects in sheep. Sci Transl Med 2018;10:eaam8828. https://doi.org/10.1126/scitranslmed.aam8828.
[63] Laratta JL, Vivace BJ, López-Peña M, Guzón FM, Gonzalez-Cantalpeidra A, Jorge-Mora A, et al. 3D-printed titanium cages without bone graft outperform PEEK cages with autograft in an animal model. Spine J 2022;22:1016–27. https://doi.org/10.1016/j.spinee.2021.12.004.
[64] Zuchuat J, Maldonado Y, Botteri J, Decco O. In vivo effect of UV-photofunctionalization of CoCrMo in processes of guided bone regeneration and tissue engineering. J Biomed Mater Res A 2021;109:31–41. https://doi.org/10.1002/jbm.a.37004.
[65] Re F, Sartore L, Borsani E, Ferroni M, Pasini C, Pandini S, et al. Potentiality of bone marrow-derived mesenchymal stromal cells (BM-MSCs) to differentiate into the osteogenic lineage in in vitro model of tissue regeneration. Blood 2023;142:5626. https://doi.org/10.1182/blood-2023-177940.
[66] You M, Jing J, Tian D, Qian J, Yu G. Dioscin stimulates differentiation of mesenchymal stem cells towards hypertrophic chondrocytes in vitro and endochondral ossification in vivo. Am J Transl Res 2016;8:3930–8.
[67] Bai Y, Liu C, Fu L, Gong X, Dou C, Cao Z, et al. Mangiferin enhances endochondral ossification-based bone repair in massive bone defect by inducing autophagy through activating AMP-activated protein kinase signaling pathway. FASEB J Off Publ Fed Am Soc Exp Biol 2018;32:4573–84. https://doi.org/10.1096/fj.201701411R.
[68] Liu Y, Kuang B, Rothrauff BB, Tuan RS, Lin H. Robust bone regeneration through endochondral ossification of human mesenchymal stem cells within their own extracellular matrix. Biomaterials 2019;218:119336. https://doi.org/10.1016/j.biomaterials.2019.119336.
[69] Furuta T, Miyaki S, Ishitobi H, Ogura T, Kato Y, Kamei N, et al. Mesenchymal stem cell-derived exosomes promote fracture healing in a mouse model. Stem Cells Transl Med 2016;5:1620–30. https://doi.org/10.5966/sctm.2015-0285.
[70] Yao W, Lay Y-AE, Kot A, Liu R, Zhang H, Chen H, et al. Improved mobilization of exogenous mesenchymal stem cells to bone for fracture healing and sex difference. Stem Cells 2016;34:2587–600. https://doi.org/10.1002/stem.2433.
[71] Nilsson Hall G, Mendes LF, Gklava C, Geris L, Luyten FP, Papantoniou I. Developmentally engineered callus organoid bioassemblies exhibit predictive in vivo long bone healing. Adv Sci 2020;7:1902295. https://doi.org/10.1002/advs.201902295.
[72] Tam WL, Freitas Mendes L, Chen X, Lesage R, Van Hoven I, Leysen E, et al. Human pluripotent stem cell-derived cartilaginous organoids promote scaffold-free healing of critical size long bone defects. Stem Cell Res Ther 2021;12:513. https://doi.org/10.1186/s13287-021-02580-7.
[73] Farrell E, Both SK, Odörfer KI, Koevoet W, Kops N, O'Brien FJ, et al. In-vivo generation of bone via endochondral ossification by in-vitro chondrogenic priming of adult human and rat mesenchymal stem cells. BMC Musculoskelet Disord 2011;12:31. https://doi.org/10.1186/1471-2474-12-31.
[74] Scotti C, Piccinini E, Takizawa H, Todorov A, Bourgine P, Papadimitropoulos A, et al. Engineering of a functional bone organ through endochondral ossification. Proc Natl Acad Sci U S A 2013;110:3997–4002. https://doi.org/10.1073/pnas.1220108110.
[75] Reinisch A, Etchart N, Thomas D, Hofmann NA, Fruehwirth M, Sinha S, et al. Epigenetic and in vivo comparison of diverse MSC sources reveals an endochondral signature for human hematopoietic niche formation. Blood 2015;125:249–60. https://doi.org/10.1182/blood-2014-04-572255.
[76] Hochmann S, Ou K, Poupardin R, Mittermeir M, Textor M, Ali S, et al. The enhancer landscape predetermines the skeletal regeneration capacity of stromal cells. Sci Transl Med 2023;15:eabm7477. https://doi.org/10.1126/scitranslmed.abm7477.
[77] Morimoto S, Kajiya M, Yoshii H, Yoshino M, Horikoshi S, Motoike S, et al. A cartilaginous construct with bone collar exerts bone-regenerative property via rapid endochondral ossification. Stem Cell Rev Rep 2023;19:1812–27. https://doi.org/10.1007/s12015-023-10554-w.
[78] Liu A, Lin D, Zhao H, Chen L, Cai B, Lin K, et al. Optimized BMSC-derived osteoinductive exosomes immobilized in hierarchical scaffold via lyophilization for bone repair through Bmpr2/Acvr2b competitive receptor-activated Smad pathway. Biomaterials 2021;272:120718. https://doi.org/10.1016/j.biomaterials.2021.120718.
[79] Dennis SC, Berkland CJ, Bonewald LF, Detamore MS. Endochondral ossification for enhancing bone regeneration: converging native extracellular matrix biomaterials and developmental engineering in vivo. Tissue Eng Part B Rev 2015;21:247–66. https://doi.org/10.1089/ten.TEB.2014.0419.
[80] Bahney CS, Hu DP, Taylor AJ, Ferro F, Britz HM, Hallgrimsson B, et al. Stem cell-derived endochondral cartilage stimulates bone healing by tissue transformation. J Bone Miner Res Off J Am Soc Bone Miner Res 2014;29:1269–82. https://doi.org/10.1002/jbmr.2148.
[81] Pigeot S, Bourgine PE, Claude J, Scotti C, Papadimitropoulos A, Todorov A, et al. Orthotopic bone formation by streamlined engineering and devitalization of human hypertrophic cartilage. Int J Mol Sci 2020;21:7233. https://doi.org/10.3390/ijms21197233.
[82] Todorov A, Scotti C, Barbero A, Scherberich A, Papadimitropoulos A, Martin I. Monocytes seeded on engineered hypertrophic cartilage do not enhance endochondral ossification capacity. Tissue Eng Part A 2017;23:708–15. https://doi.org/10.1089/ten.tea.2016.0553.
[83] Cunniffe GM, Vinardell T, Murphy JM, Thompson EM, Matsiko A, O'Brien FJ, et al. Porous decellularized tissue engineered hypertrophic cartilage as a scaffold for large bone defect healing. Acta Biomater 2015;23:82–90. https://doi.org/10.1016/j.actbio.2015.05.031.

[84] Feng X, Li Z, Wei J, Feng Z, Wu W, Zhao Y. Injectable cartilaginous template transformed BMSCs into vascularized bone. Sci Rep 2018;8:8244. https://doi.org/10.1038/s41598-018-26472-8.
[85] Vas WJ, Shah M, Blacker TS, Duchen MR, Sibbons P, Roberts SJ. Decellularized cartilage directs chondrogenic differentiation: creation of a fracture callus mimetic. Tissue Eng Part A 2018;24:1364–76. https://doi.org/10.1089/ten.TEA.2017.0450.
[86] Longoni A, Utomo L, Robinson A, Levato R, Rosenberg AJWP, Gawlitta D. Acceleration of bone regeneration induced by a soft-callus mimetic material. Adv Sci Weinh Baden-Wurtt Ger 2022;9:e2103284. https://doi.org/10.1002/advs.202103284.
[87] Liu A, Li Y, Wang Y, Liu L, Shi H, Qiu Y. Exogenous parathyroid hormone-related peptide promotes fracture healing in Lepr(-/-) mice. Calcif Tissue Int 2015;97:581–91. https://doi.org/10.1007/s00223-015-0041-2.
[88] Hall GN, Chandrakar A, Pastore A, Ioannidis K, Moisley K, Cirstea M, et al. Engineering bone-forming biohybrid sheets through the integration of melt electrowritten membranes and cartilaginous microspheroids. Acta Biomater 2023;165:111–24. https://doi.org/10.1016/j.actbio.2022.10.037.
[89] Critchley S, Sheehy EJ, Cunniffe G, Diaz-Payno P, Carroll SF, Jeon O, et al. 3D printing of fibre-reinforced cartilaginous templates for the regeneration of osteochondral defects. Acta Biomater 2020;113:130–43. https://doi.org/10.1016/j.actbio.2020.05.040.
[90] Yokoi H, Take Y, Uchida R, Magome T, Shimomura K, Mae T, et al. Vibration acceleration promotes endochondral formation during fracture healing through cellular chondrogenic differentiation. PLoS ONE 2020;15. https://doi.org/10.1371/journal.pone.0229127.
[91] Grgurevic L, Oppermann H, Pecin M, Erjavec I, Capak H, Pauk M, et al. Recombinant human bone morphogenetic protein 6 delivered within autologous blood coagulum restores critical size segmental defects of ulna in rabbits. JBMR Plus 2019;3:e10085. https://doi.org/10.1002/jbm4.10085.
[92] Camirand A, Goltzman D, Gupta A, Kaouass M, Panda D, Karaplis A. The role of parathyroid hormone-related protein (PTHrP) in osteoblast response to microgravity: mechanistic implications for osteoporosis development. PloS One 2016;11:e0160034. https://doi.org/10.1371/journal.pone.0160034.
[93] Chen T, Wang Y, Hao Z, Hu Y, Li J. Parathyroid hormone and its related peptides in bone metabolism. Biochem Pharmacol 2021;192:114669. https://doi.org/10.1016/j.bcp.2021.114669.
[94] Wang J, Leung KS, Chow SK, Cheung WH. The effect of whole body vibration on fracture healing - a systematic review. Eur Cell Mater 2017;34:108–27. https://doi.org/10.22203/eCM.v034a08.
[95] Cheung WH, Wong RMY, Choy VMH, Li MCM, Cheng KYK, Chow SKH. Enhancement of osteoporotic fracture healing by vibration treatment: the role of osteocytes. Injury 2021;52(Suppl 2):S97–100. https://doi.org/10.1016/j.injury.2020.05.020.

Superintendencia de Industria y Comercio

Superintendencia de Industria y Comercio

Certificado Número: **44419**

Otorga Patente de Invención a:

INSTITUTO DISTRITAL DE CIENCIA BIOTECNOLOGIA E INNOVACIÓN EN SALUD - IDCBIS

A la creación denominada:

MÉTODO DE FABRICACIÓN DE UN DISPOSITIVO MÉDICO MEDIANTE IMPRESIÓN 3D Y ELECTROHILADO

Clasificación: A61L 2/00, A61L 27/00, A61L 15/22

Vigente:

Desde: 7 de marzo de 2022
Hasta: 7 de marzo de 2042

Que la Solicitud de Patente de Invención No.NC2022/0002677 cumple con los requisitos previstos en las disposiciones legales vigentes, Resolución No.51367 de 30 de julio de 2025 en testimonio de ello se estampa la firma del funcionario competente.



Firmado digitalmente por: CIELO ELAINNE RUSINQUE URREGO
Fecha: 2025.09.16 09:01:12 COT
Razón: Validez juridica.
Ubicación: Bogotá, Colombia.